# University of Alberta

Transport and Deposition of Particles onto Homogeneous and Chemically Heterogeneous Porous Media Geometries

by

Reeshav Chatterjee

A thesis submitted to the Faculty of Graduate Studies and Research
in partial fulfillment of the requirements for the degree of Master of Science

Master of Science

Mechanical Engineering


Fall 2011
Edmonton, Alberta

To my parents, Late Tanima Chatterjee and Jyotirmoy Chatterjee

# Abstract

Particle transport and deposition in porous media are central to a wide gamut of natural and engineering processes. In order to establish optimal macroscopic performance, it is essential to understand the microscopic colloid transport fundamentals that ultimately manifest at the macroscopic scale. The present body of work intends to provide an insight into the fundamentals of particle transport and deposition onto ideal porous media geometries. An Eulerian model, was developed to evaluate particle deposition rates onto homogeneous and heterogeneous surfaces of two model geometries-a spherical collector and a cylindrical microchannel. For a homogeneous spherical collector, in the absence of Electrostatic Double Layer interactions, the correctness of the Levich solution was established for Brownian particle deposition. Further, it was shown that surface chemical heterogeneity can be effectively tuned to design novel fluidized bed filters. Surface heterogeneity in cylindrical channels was identified as an effective tool in drug targeting and controlling analyte/biomolecule transport in microfluidic devices.

**Keywords:** Particle deposition, Convection-Diffusion-Migration equation, Eulerian analysis, Patterned Heterogeneity

# Acknowledgements

First and foremost, I thank Prof. Mitra for giving me the opportunity to pursue graduate studies here at the University of Alberta. If not for his diligence, I would not have been here today as I had missed the application deadline. His confidence in me has always helped me do better with my research. I have had the opportunity to share frank discussions with him on several occasions which have helped me focus better and aim higher. I am simply awestruck by his ambitious outlook towards life which I have tried to inculcate in me. His brisk responses to my problems have helped me maintain good pace during my research and achieve a few personal milestones on the professional front.

On my first meeting with Prof. Bhattacharjee, he said

"All my previous students have managed to provide me with the 'wow-factor' in their work."

That was the first of several motivational quotes I had received from Dr. Bhattacharjee during my stay as a graduate student. It is only befitting to say that what I am today as an individual plying my trade in scientific research is because of him. Over the past two years, the support and help I have received from Prof. Bhattacharjee is indescribable. From teaching me FORTRAN hands on, to helping me with my research till midnight, he has been a beacon in my life. The technical and motivational discussions we shared on several weekends shall remain etched in my memory forever. His dedication, zeal and vision towards focused research has served as a constant source of inspiration and shall continue to elevate my thoughts for many years to come. In all, a few words of gratitude is insufficient to describe the respect I have for him and the debt I owe him for his teachings in science as well as philosophies in life. He has indeed been a godfather.

Life at work would not have been good had life at home not been so as well. It will be gravely unfair if I don't acknowledge the support and company of my dear colleague and friend Satyasai Gajapathi during these two years. I can't describe how much I enjoyed the scientific arguments I have had with him at home. I have known him for almost 6 years now, and our friendship has

only grown in these two years of graduate life. With that, I must also thank my colleagues at the Micro and Nano Transport Laboratory (MNTL), especially Prashant Waghmare and Nagasiva Gunda and all my colleagues at the Colloids and Complex Fluids Laboratory (CCF) including Dr. Tania Rizwan, Dr. Jeff Kemps and Dr. Neda Nazemifard.

Finally, the support of my family members has helped me hold my own during the tough times in the past couple of years. Without my father's encouragement and words of calm, it would have been difficult for me to sustain myself away from home for so long. My aunt's persistence must be given due credit as well. Without her effort, I would not have been able to see through the toughest ten years of my life since my mother's demise. And talking about my mother, I am now bearing the fruits for the seeds she sowed in me for the 16 years of life I had with her. She taught me to have a goal in life without which I would not have been able to achieve even the trifle that I have managed till date.

# Contents

[1] Parts of this chapter have been published in *Langmuir*, June 2011, doi:10.1021/la201421n., *In press*

[2] Parts of this chapter have been published in *Microfluidics and Nanofluidics*, July 2011, doi:10.1007/s10404-011-0847-9 *In press.*

# List of Figures

# List of Tables

# Chapter 1

# Introduction

## 1.1 Background and Overview

Particle deposition is a frequently encountered phenomenon in wide a range of industrial and natural processes spanning fouling of surfaces [Ngene et al., 2010], filtration techniques [Rajagopalan and Tien, 1976], coating paint on surfaces [Ali et al., 2000], particle capture by microbubble floatation [Liu et al., 2010], chromatographic separation [Buffham, 1996], biomolecular devices [Soliman et al., 2010], etc. Particle deposition can be defined as particle transport from flowing suspensions to a substrate followed by its attachment to the substrate. Depending upon the application, particle deposition can be desirable or undesirable. Hence it is important to understand and devise methods to control the deposition process. With the advent of nanotechnology and state-of-the art micro- and nano- fabrication methods, considerable emphasis has been given to the development a deeper understanding of the sub-micron scale particle deposition process.

Particle deposition has been a subject of immense interest since the 1960's. Different flow regimes and geometries have been considered for studying particle deposition including rotating disk systems [Adamczyk et al., 1978], impinging jet geometry [Adamczyk et al., 1986], rectangular and cylindrical channels [Adamczyk and van de Ven, 1981], and spherical collectors [Elimelech et al., 1995, Rajagopalan and Tien, 1976]. A through review of deposition processes on these geometries have been summarized in various texts [Elimelech et al., 1995, Masliyah and Bhattacharjee, 2006]. Of these, evaluating particle deposition on a spherical collector in a packed bed system has been widely used

to simulate particle transport and deposition in porous media. For a packed bed of spheres, the Happel sphere-in-cell model [Happel, 1958] is a commonly adopted tool to investigate the fundamental mechanisms of particle deposition. As stated earlier, deposition involves particle transport to large surfaces (called collectors) where adsorption occurs. Three major factors contribute to particle transport, namely, Brownian motion (diffusion) , fluid motion (convection) and external forces (migration) acting on the particle. As a particle approaches the collector surface, the colloidal interactions, which account for the external forces acting on the particle, becomes the predominant mode of transport. The colloidal interactions are modeled using the classical DLVO (Derjaguin-Landau-Verway-Overbeek) theory [Derjaguin and Landau, 1941, Verwey and Overbeek, 1948]. According to the DLVO theory, the net force between the particle and the collector depends on the surface-to-surface separation distance $h$ as shown in Figure 1.1. The DLVO theory also suggests that the nature of the interactions (whether attractive or repulsive) depends upon the physical and chemical properties of the surfaces of both the collector and the particle. Since, the DLVO interactions deal with surface forces, colloid deposition studies are valid (i.e, surface to volume ration must be significant) for particles between $10^{-9}\ m\ <\ a_p\ < 10^{-5}\ m$, where $a_p$ is the paricle radius.

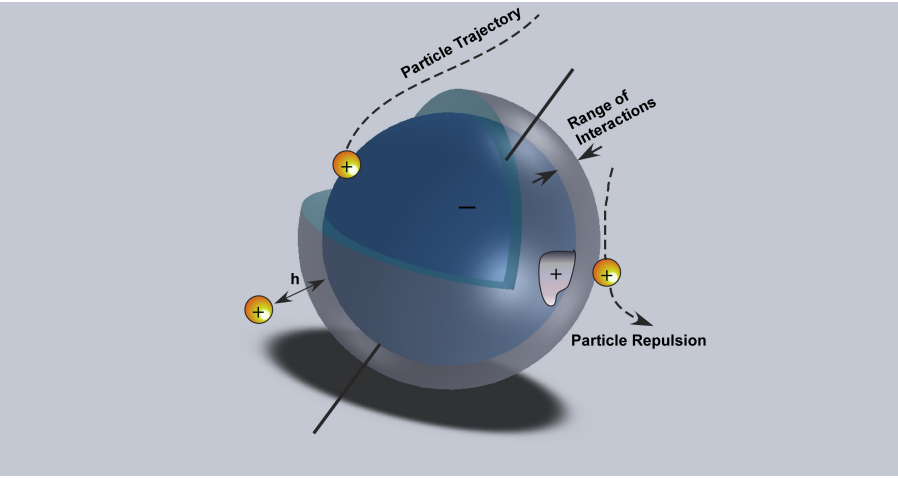


**Figure 1.1** – Schematic depiction of particle depostion onto a spherical substrate. The semi-transparent shell denotes the zone of particle capture where colloidal interactions are dominant. The interactions are a function of the surface to surface separation distance $h$ between particle and substrate as indicated in the figure. The figure also depicts the effect of surface charge distribution on the colloidal particle's trajectory.

In addition to colloidal interactions, particles also respond to the viscous fluid motion they are suspended in. Hence, the moving fluid drags the particle along with it as it flows (convection). Conversely, the motion of the particle also affects the fluid flow field. However, for laminar, creeping flow systems ($Re << 1$), viscous damping effects significantly mask the inertial effects [Kemps, 2010]. Thus there is a direct relationship between the force acting on the particle due to the fluid and the disturbance it creates in the flow field. Hydrodynamic interaction (or hydrodynamic drag) is defined as the resistance to a particle approaching a surface due to the fluid molecules being squeezed out of the shrinking space between the surfaces. Hydrodynamic interactions affect all three transport mechanisms (convection, diffusion and migration) to different extents and must be accurately accounted for to predict particle deposition rates.

Theoretical investigation of particle transport and deposition can be performed by employing two approaches - Eulerian and Lagrangian. In the Eulerian method, the generalized convection-diffusion-migration equation is solved in space using a continuum assumption to evaluate the spatial distribution of particles. The convection-diffusion-migration equation is representative of the three mechanisms of particle transport due to Brownian motion (diffusion), fluid flow (convection) and external field forces (migration). The second approach which is the Lagrangian framework focusses on tracking the trajectory of a single colloidal particle using simple force balace (Newton's laws). Although the two methods are different in their implementations, they capture the same physics of particle transport and should point to identical conclusions regarding particle deposition. The present body of work employs the Eulerian method to evaluate particle transport in two geometries most relevant to porous media transport, namely the sphere-in-cell geometry for a packed bed and cylindrical microchannel which serves as an approximation to the pores in porous media.

In context of particle deposition, heterogeneities on the collector surface has a profound influence on the overall deposition behavior. Heterogeneities can be in the form of surface roughness (physical heterogeneity) or due to presence of charged species on the collector surface (chemical heterogeneity). When heterogeneities are present, the collector surface cannot be approximated as

smooth and homogeneous. It is worth noting that most natural and engineering process involve surface heterogeneity (both physical and chemical) and hence it is imperative to evaluate the role of surface heterogeneity on particle deposition. Effect of surface heterogeneity on particle deposition has attracted a lot of interest of late and significant amount of relevant research has been performed [Rizwan and Bhattacharjee, 2009, Vaidyanathan and Tien, 1991]. Majority of these works have focussed on deposition of planar heterogeneous substrates [Duffadar and Davis, 2008, Kemps and Bhattacharjee, 2005]. In a recent study by Saiers and Ryan [2005], physical heterogeneity was modeled as hemispherical asperities on the surface of a spherical collector and its effect on particle deposition was reported. However, there is a paucity of theoretical work dealing with surface chemical heterogeneity on spherical collectors and cylindrical microchannels. The present study evaluates the role of surface chemical heterogeneity on particle deposition on a spherical collector and in a cylindrical microchannel and captures the effect of the collector geometry on particle deposition.

Chemical heterogeneity results from uneven surface charge distribution on the collector surface. Figure 1.1 qualitatively depicts the effect of surface charge on the trajectory of a particle in the vicinity of the collector. The surface has two types of randomly distributed charges which determines whether it is favorable or unfavorable to deposition of a charged colloidal particle. Surface impurities, difference in mineral constituents etc contribute to chemical heterogeneity. Modeling the random surface charge distribution is difficult from the theoretical point of view. One of the common methods to approximate the surface charge distribution is the use of patterning technique [Nazemifard et al., 2006] which facilitates tractable analysis of particle deposition. In this two types of surface charge is defined on the surface of the collector as alternate stripes. It is noteworthy that surface charge distributions varies over large length scales and it has been proven that spatial averaging (patchwise heterogeneity model) [Song et al., 1994] works remarkably well only for macroscopic length scales [Elimelech et al., 2003]. For microscopic chemical heterogeneity, this approximation leads to erroneous results and appropriate modifications to the modeling must be incorporated to capture the effect of the heterogeneity on particle deposition correctly. The present body of work deals entirely with microscopic surface charge distribution and captures the combined effect of

the other transport mechanisms and the surface charge distribution on particle deposition.

## 1.2 Problem Statement

In light of particle transport in porous media, it must be understood that it is almost impossible to characterize the random geometry of real porous structures. Hence approximations must be made with regards to the porous media geometry, in order to enable tractable modeling analysis. In the present study, two geometries are considered as approximations to the real porous media. Firstly, the porous media is approximated as a packed bed of spheres following which the single collector efficiency is calculated using the Happel sphere-in-cell model [Happel, 1958]. Particle deposition behavior is first investigated on a smooth homogeneous spherical collector in order to validate the fundamental mass transport principles. The initial validation part of the model development (involving deposition onto homogeneous collectors) was important in light of the existing debate on the deposition behavior of particles on spherical collectors especially for sub-micron sized particles (Brownian regime). Although a lot of research has been directed towards it over the past three decades, the question as to why these models predict different deposition rates for the same geometry is still unanswered. It was initially proposed that the analytical Levich solution [Levich, 1962] defines the deposition efficiency for Brownian particles. This however was later refuted. How accurate is the analytical Levich solution in predicting deposition efficiency of Brownian particles? Does it represent the true limiting mass transport behavior? Upon logically answering these questions, the model is improved by incorporating micropatterned surface charge heterogeneity and its effect on the particle deposition rate is investigated. The particle deposition model with surface charge heterogeneity formed the second subpart for analyzing deposition onto spherical collectors.

Porous structures are also characterized by pores of varying lengths and diameters which donot allow systematic evaluation of particle transport. Hence, approximating the pores as cylindrical microchannels provides a viable solution to overcome the modeling difficulties and facilitate systematic analysis of

particle transport. Thus, in the second problem, a cylindrical microchannel with patterned surface heterogeneity is considered and the transport and deposition of particles suspended in a fluid flowing through the microchannel is investigated. Considering transport of particles suspended in a carrier fluid in micro/nano scale channels is central to numerous microfluidic and nanofluidic systems, the model would provide enhanced understanding of how these particles tend to stick to the walls of the microchannel or get transported through it. In both problems, the fluid is assumed to be operating in the Stoke's flow regime which is consistent with porous media systems.

The effect of the surface chemical heterogeneity coupled with the geometry and flow parameters on the deposition behavior is investigated (for both the spherical collector and the cylindrical microchannel). For the cases where micropatterned surface charge heterogeneity is considered, it is important to understand the rationale behind patterning. Is it merely to replicate the surface chemical heterogeneities? Can artificial patterning be useful in controlling the deposition rates? If they can, what are the prospects of developing novel particle separation systems by tuning these patterned surfaces?

## 1.3 Objectives and Scope

### 1.3.1 Objectives of the Present Study

With the preceding questions in mind, the major objectives of the present thesis can be summarized as

1. Evaluate the contribution of each of the particle transport mechanisms individually in the sphere-in-cell geometry. Investigate the accuracy of the analytical Levich equation in predicting deposition efficiency of Brownian particles. Explain the reasons for the disagreements between existing models. Establish a correct correlation which accurately predicts particle deposition efficiency for a range of particle sizes.

2. Develop a model to investigate the effect of surface charge heterogeneity on the local and overall particle deposition behavior in a sphere-in-cell geometry. Analyze the effect of change in orientation of the fluid flow approaching the collector and the available area fraction on the deposition rates.

3. Develop a computational model to investigate the effect of surface charge heterogeneity on the particle transport behavior in a micropatterned cylindrical microchannel.

4. Propose techniques to tune these artificially prepared collectors for designing novel particle separation systems with enhanced retention efficiency and improved operational life.

### 1.3.2 Scope of the Present Study

In order to reconcile the disagreements of the previous models in predicting the single collector efficiency, it was important to maintain the same physical and chemical properties of the system as in the other models. Thus the the only colloidal interactions considered for the validation part of the problem was the attractive van der Waals interactions between the collector and particle. Electrostatic Double Layer (EDL) interactions were neglected. Real surfaces however are almost always charged due to the presence of ions in solution and on the surfaces. The evaluation of the single collector efficiency in itself comes with inherent assumptions which include very dilute particle concentrations and totally clean collector. In other words it gives an indication of the initial deposition rates only and does not consider the transient blocking of the collector surface due to surface fouling by the particles. Very dilute particle concentration is assumed to ensure inter particle interactions are negligible. Further, large particle to collector aspect ratio systems have been considered which makes the sphere-in-cell system very similar to the deposition onto a flat plate system especially near the collector wall.

The assumption of smooth and chemically homogeneous surface greatly simplifies evaluation of particle transport around such surfaces but at the cost of pragmatic depiction of the real systems. Since in most real systems, the heterogeneity is random, modeling deposition onto such surfaces is practically impossible using the conventional continuum type approach. Hence, the heterogeneity was modeled as alternate stripes of positive and negative surface charges (or alternate attractive and repulsive regions). Further, the analysis in this model is restricted to chemical heterogeneity due to surface charges only. Physical heterogeneities have not been considered in the present body of work to maintain modeling simplicity. Most real systems however have both

physical and chemical heterogeneities on the surface of the substrates.

For evaluating particle transport in a patterned microchannel, the flow was assumed to be fully developed and parabolic in nature. This again is an idealization as flow in microchannels is never truly parabolic. Further, the pores in a real porous matrix are hardly ever cylindrical throughout their lengths. Similarly, for the sphere-in-cell geometry the assumptions that the packed bed is made up of uniform spheres is an idealization for modeling tractability.

## 1.4 Overview of the Thesis

The content of this thesis has been subdivided into 6 chapters with each chapter looking at different aspects of particle deposition onto porous media.

In the present chapter (Chapter 1), a general overview of the deposition process has been described followed by a concise problem statement and the objectives of the present study. The present chapter also highlights the scope of problem statement which basically describes the underlying simplifying assumptions which were employed to enable tractable analysis of the deposition problem.

In Chapter 2, a thorough review of existing work on particle deposition has been presented. This includes deposition onto both homogeneous and heterogeneous substrates. Further, a critical review of the existing analytical correlations for predicting single collector efficiency has been performed. This chapter sets the foundation for the remaining chapters of the thesis in which we discuss particle deposition onto various porous media geometries with different surface chemistries.

Chapter 3 discusses particle deposition onto homogenous sphercical collectors in the absence of Electrostatic Double Layer (EDL) interactions. The results are compared with other models in literature with the objective of establishing the correct deposition behavior for Brownian particles. In the later half of the chapter, a new correlation is presented for predicting single collector efficiency as a function of particle size.

Most real substrates are chemically heterogeneous in aqueous solution. Chapter 4 investigates the effect of surface chemical heterogeneity on particle deposition. In this chapter, the packed bed is assumed to be an assemblage of micropatterned charged spheres. The numerical model from chapter 3 is modified and surface heterogeneity is incorporated.

In Chapter 5, effect of surface charge heterogeneity on particle transport in a cylindrical channel is presented. Chapter 5 lends significant insight into particle/analyte transport in microfluidic devices involving cylindrical channels.

In the final chapter, the most important conclusions from each chapter are summarized and possible areas of improvement of the developed model are discussed.

# Chapter 2

# Literature Review

## 2.1 Introduction

Particle transport and deposition in porous media geometries has been a subject of intense research for over half a century. The fundamental principles of particle transport and interactions have been used in various engineering and biomedical systems ranging from ground water transport, chromatographic separation, filtration methods, surface fouling, in developing materials with novel surface properties, transport of biomolecules and analytes, drug delivery and many more. The subject of particle deposition in porous structures has evolved over the years involving extensive theoretical and experimental studies with an attempt to replicate real porous media and the particle wall interactions associated therewith. This literature review aims to summarize the relevant previous works on particle transport in porous structures using the sphere-in-cell geometry and cylindrical microchannel. The review is divided into three main parts dealing with evaluation of particle transport in a homogeneous sphere-in-cell model, relevant works and applications of heterogeneous substrates and its extension to the sphere-in-cell models and finally particle transport in heterogeneous microchannels. The discussion maintains a flow starting from particle transport in homogeneous systems and then develops into investigating transport in the presence of surface heterogeneity.

## 2.2 Happel sphere-in-cell Model

In studies dealing with Colloid Filtration Threory (CFT) [Shen et al., 2010, Yao et al., 1971], the Happel sphere-in-cell model [Elimelech et al., 1995, Hap-

pel, 1958] is a commonly used tool to evaluate particle deposition rates in granular porous media. A packed bed of spherical collectors is often used to simulate particle transport in such systems [Payatakes et al., 1974, Rajagopalan and Tien, 1976, Tufenkji and Elimelech, 2004, Yao et al., 1971]. Figure 2.1(a) schematically depicts a porous medium approximated as an assemblage of spheres. According to the Happel cell model, the porous medium is a packed bed of identical spheres (of radius $a_c$) in which each sphere is enveloped by a thin film of fluid. The thickness of the fluid shell, $b$ in Figure 2.1(b) is defined by the porosity of the medium or conversely, the volume fraction of the spheres in the packed bed. The transport behavior around the single isolated spherical collector gives an indication of the deposition characteristics of the entire porous bed. It is important to note that, although the analysis considers only one spherical collector, the fluid flow field in the fluid shell will be affected by the presence of the other neighboring collectors. This is accounted for by modifying the flow field in the shell using the porosity factor [Tien, 1989]. The Happel cell model neglects the interactions between the collectors and only considers particle-collector interactions.

The transport efficiency parameter which gives an indication of the initial deposition rate in the Happel cell model is known as the single collector efficiency [Elimelech et al., 1995, Payatakes et al., 1974, Ruckenstein, 1964, Tien, 1989]. Single collector efficiency is defined as the ratio of the rate at which colloidal particles strike the collector surface to the rate at which the particles are flowing towards the collector [Shen et al., 2010, Yao et al., 1971]. In essence the single collector efficiency quantifies the initial deposition rate on a "clean" collector. The single collector efficiency ($\eta$) is directly related to the overall filter coefficient of the medium ($\lambda$) defined as [Elimelech et al., 1995, Tien, 1989]

$$\lambda = \frac{3}{2}\frac{1-f}{(2a_c)}\alpha\eta \tag{2.1}$$

where $f$ is the medium porosity, $a_c$ is the radius of the spherical collector and $\alpha$ is the sticking efficiency which is defined as the ratio of the number of particles striking the collector surface to the number of particles sticking to it. Under ideal cases $\alpha$ is approximated as 1. Evaluation of this single collector ef-

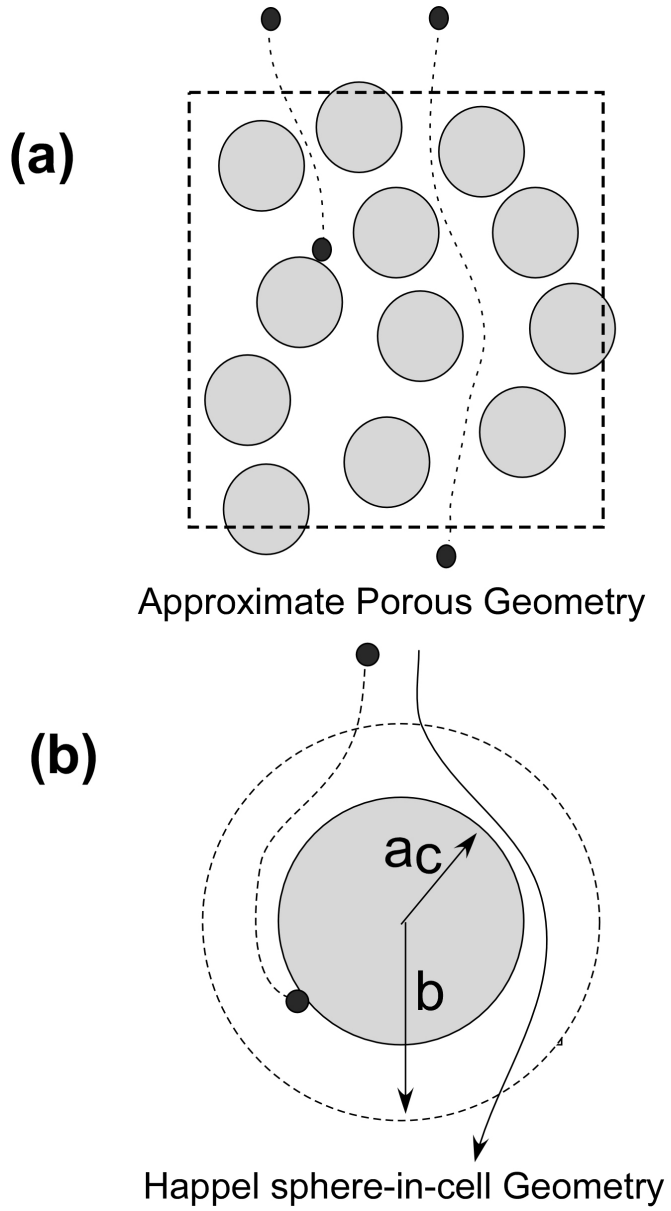


**Figure 2.1** – Particle transport in saturated porous media (a) Schematic representation of porous media as an assemblage of spheres. (b) Happel sphere-in-cell geometry showing a single collector with radius $a_c$ and shell radius $b$.

ficiency parameter involves rigorous numerical calculation by employing either the particle tracking method (Lagrangian framework) or the field evaluation method (Eulerian framework).

### 2.2.1 Happel's Flow Field

Before reviewing the methods and models to evaluate single collector efficiency, it is important to discuss the fluid and mass transport mechanisms in the Happel cell model. This subsection focuses on the hydrodynamic aspects of the cell model. As mentioned earlier, the thickness of the fluid shell $b$ in the Happel cell model is a function of the porosity of the granular medium as is given by the expression [Elimelech, 1994, Masliyah and Bhattacharjee, 2006]

$$\frac{a_c}{b} = (1 - f)^{1/3} \tag{2.2}$$

$f$ is the medium's porosity, $a_c$ and $b$ are as defined by Figure 2.1(b). Equation 2.2 simply assigns the shell thickness $b$ such that the collector to cell volume ratio is equal to the volume fraction of the entire medium. Thus, the cell thickness is characteristic of the porous medium and is independent of the flow and other transport parameters involved. To solve a mass transport problem however, the governing fluid transport and mass flux equations need to be solved in the fluid shell of the cell model.

Since most porous media flows operate in the creeping flow regime (i.e, $Re << 1$), the fluid transport in the shell is governed by the Stokes equation [Masliyah and Bhattacharjee, 2006] which describes the motion of the fluid relative to the collector.

$$\mu \nabla^2 \mathbf{u} = \nabla P - \mathbf{f_b} \tag{2.3}$$

where $\mu$ is the fluid viscosity, $\mathbf{u}$ is the fluid velocity vector, and $\mathbf{f_b}$ is the sum of the body force vectors. Solution of the Stokes equation in conjunction with the continuity equation gives the fluid flow field distribution in the shell.

Ofcourse, appropriate boundary conditions must be provided along with the Stokes and continuity equation to establish the fluid flow field. The boundary conditions for solving the flow field are

$$\mathbf{u} = 0 \qquad at \qquad r = a_c \tag{2.4}$$

which signifies no slip condition at the wall of the spherical collector and

$$\tau_{r\theta} = \mu \nabla \mathbf{u} = 0 \qquad at \qquad r = b \tag{2.5}$$

where $\tau_{r\theta}$ is the shear stress and $\nabla \mathbf{u}$ is the gradient of the velocity vector (in spherical co-ordinates). Thus, Equation 2.5 states that at the outer boundary of the shell there is no shear stress. The boundary condition given by Equation 2.5 is known as the Happel's boundary condition proposed by Happel [1958] and Happel and Brenner [1965]. Careful observation reveals that the Happel boundary condition states that the shell thickness is larger than the hydrodynamic boundary layer (where shear stress vanishes due to absence of viscous effects). Due to the shape of the spherical collector the hydrodynamic boundary layer thickness is varies along the tangential position on the collector. Figure 2.2 schematically depicts the hydrodynamic boundary layer thickness and the Happel's boundary. It is very interesting to note that the shell thickness does not impose any restriction on the hydrodynamic boundary layer thickness. Thus, for low flow velocities it is actually possible that the hydrodynamic boundary layer thickness is greater than the shell thickness where shear flow is maximum. In such a scenario, the Happel's boundary condition will not be valid and hence, the Happel cell model must be employed judiciously.

For an incompressible fluid, the stream function ($\Psi$) for an axisymmetric creeping flow in spherical co-ordinates is given as [Elimelech et al., 1995, Tien, 1989]

$$\left[\frac{\partial^2}{\partial r^2} + \frac{sin\theta}{r^2}\frac{\partial}{\partial \theta}\left(\frac{1}{sin\theta} - \frac{\partial}{\partial \theta}\right)\right]^2 \Psi = 0 \tag{2.6}$$

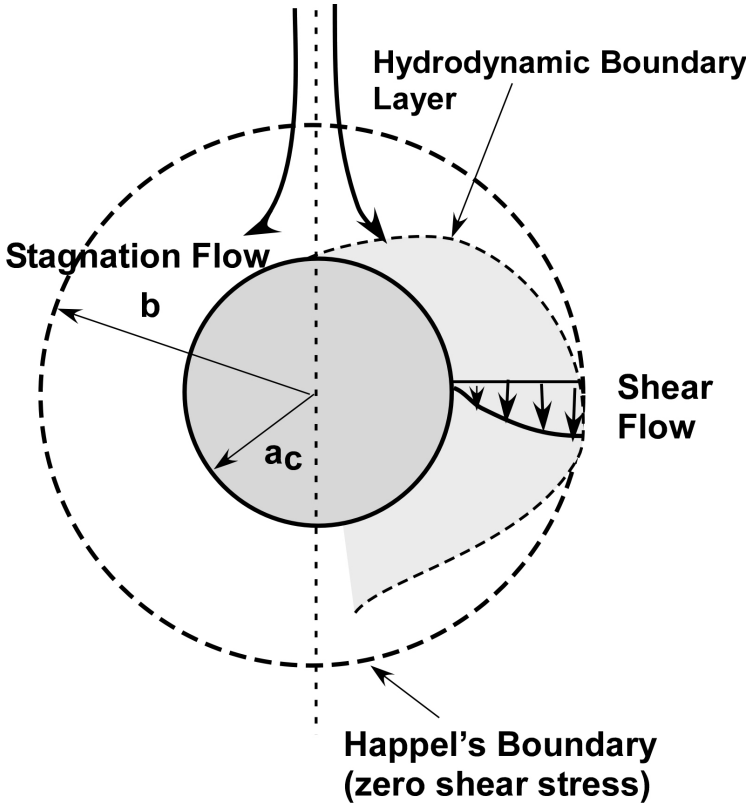


**Figure 2.2** – Happel boundary condition and hydrodynamic boundary layer thickness in the sphere-in-cell geometry. Stagnation and shear flow regimes exist in the cell model due to the sphericity of the collector.

where $r$ and $\theta$ denote the radial and tangential co-ordinate in the cell. The appropriate steam function expression which accounts for the disturbances in the flow field around the cell due to the presence of the neighboring collectors was given by Tien [1989] as

$$\Psi = \widehat{A}\left[K_1\left(\frac{a_c}{r}\right) + K_2\left(\frac{r}{a_c}\right) + K_3\left(\frac{r}{a_c}\right)^2 + K_4\left(\frac{r}{a_c}\right)^4\right] sin^2\theta \qquad (2.7)$$

Here $U$ is the free stream velocity, and $K_i,\ i \in [1,4]$ are porosity dependent parameters which can be determined by employing the appropriate boundary conditions for the flow model. The exact expressions for the $K_i$'s are given in Table 2.1. Using the analytical stream function expression, the radial and tangential components of the fluid velocity can be be evaluated readily by calculating the derivatives in the radial and tangential directions.

| Parameter | Expression |
|---|---|
| $\widehat{A}$ | $Ua_c^2/2$ |
| $K_1$ | $1/w$ |
| $K_2$ | $-(3+2p^5)/w$ |
| $K_3$ | $(2+3p^5)/w$ |
| $K_4$ | $-p^5/w$ |
| $w$ | $2-3p+3p^5-2p^6$ |
| $p$ | $a_c/b\ =\ (1-f)^{\frac{1}{3}}$ |

**Table 2.1** – Constants used for defining flow field around a unit collector in granular porous media

### 2.2.2 Particle Transport Mechanisms in the Cell Model

The three major mechanisms which contribute to particle transport and deposition are convection, diffusion and migration [Molla and Bhattacharjee, 2007, Nazemifard et al., 2006]. Particle transport by convection occurs due to Stokes drag which pulls the particle along with the flowing fluid. Diffusive transport is driven by the random motion of the suspended particle due to molecular

collisions from the surrounding fluid and migration is governed by the colloidal interactions between the particle and the collector surface. Depending upon the conditions of the flow system in question, these three mechanisms affect the particle transport to different extents and at different length scales. It is important to evaluate each of these three mechanisms carefully to develop a deep understanding of the deposition processes.

**Convective Transport and Hydrodynamic Interactions**

For a particle suspended in an unbounded flowing fluid, its velocity can be assumed to be the same as the fluid velocity and the particle is follows the fluid streamlines [Kemps, 2010]. In most colloidal deposition systems, it is usually assumed that the particle does not disturb the fluid flow field [Elimelech et al., 1995]. The factors that effect convective particle transport are the fluid viscosity (which defines the viscous damping effect) and the particle radius (defining the projected drag area). Thus the Stokes drag is directly proportional to both these quantities ($Drag \propto a_p\mu$ where $a_p$ is the particle radius) [Dickinson, 1985]. The situation however changes dramatically near a bounding surface. Near the surface, the particle experiences enhanced resistance as the fluid molecules squeeze out of the thin bounding space [Dickinson, 1985, Kim and Karrila, 2005]. Thus, the fluid and particle velocities are very different. To account for this, analytical hydrodynamic correction factors were developed to accurately calculate the particle velocities near the wall [Brenner, 1961, Goldman et al., 1967, Goren and Oneill, 1971, Spielman, 1977, Spielman and Fitzpatr., 1973]. For the Happel cell model, the particle and fluid velocities are coupled as

$$v_r = f_1(H) f_2(H) u_r \tag{2.8}$$

and

$$v_\theta = f_3(H) u_\theta \tag{2.9}$$

where $u_r$ and $u_\theta$ denote the fluid velocity components in the radial and tangential directions while $v_r$ and $v_\theta$ denote the corresponding particle velocity

components. $H(= h/a_p)$ is the scaled surface-to-surface separation distance between particle and collector. $f_1(H),\ f_2(H),\ f_3(H)$ are the correction factors that account for the hydrodynamic interactions between the particle and the collector at close separation distances. At large separation distances (or conversely in an unbounded flowing fluid) the hydrodynamic correction functions decay to a value of 1, in which case the fluid and particle velocities are equal. Several correlations these correction factors exist in literature [Brenner, 1961, Goldman et al., 1967, Payatakes et al., 1974, Spielman and Fitzpatr., 1973]. The present body for work employs the curve fit expressions extracted from the book by Masliyah and Bhattacharjee [2006]. Table 2.2 provides these correlation expressions.

| i | $a_i$ | $b_i$ | $c_i$ | $d_i$ | $e_i$ |
|---|---|---|---|---|---|
| 1 | 0.9267 | -0.3990 | 0.1487 | -0.6010 | 1.2020 |
| 2 | 0.5695 | 1.3550 | 1.3600 | 0.8750 | 0.5250 |
| 3 | 0.1500 | -0.3750 | 3.9060 | -0.6250 | 3.1050 |
| 4 | 1.2600 | -2.6760 | 0.3581 | 1.9990 | 0.2320 |

$$f_i(H) \ = \ 1.0 \ + \ b_i \ exp(-c_i H) \ + \ d_i \ exp(-e_i H^{a_i})$$

**Table 2.2** – Hydrodynamic correction factors to relate the particle velocity to the fluid velocity in the proximity of the collector.

Another important aspect of hydrodynamic interactions which is not often discussed is the effect of the particle size. Following the reasoning for the enhanced particle drag near the surface, an important question arises as to what happens when the particles are "point-like". Physically, for a vanishingly small particle, it has to squeeze a very small amount of fluid between itself and the collector surface. Hence, the near wall drag is negligible and it is safe to assume that the fluid and particle velocities are the same at all times. Further, for "point-like" particles the Stokes drag is also insignificant for realistic values of fluid viscosity [Dickinson, 1985]. Hence, it can be summarized that for vanishingly small particles, particle transport by convection has negligible impact on the deposition process.

### Diffusive Transport and Hydrodynamic Interactions

As discussed earlier, diffusive transport occurs due to Brownian motion of the particle as a result of molecular collisions from the surrounding fluid. It is intuitive that Brownian motion is more pronounced for "point like" particles as inertial resistance is small. Also, as viscosity increases, diffusion decreases due to viscous damping. Hence, the two main factors affecting diffusion are particle size and viscosity [Dickinson, 1985]. The diffusion coefficient is given by the Stokes Einstein expression as [Edward, 1970]

$$D_\infty = \frac{k_B T}{6\pi\mu a_p} \tag{2.10}$$

where $k_B$ is the Boltzmann constant and $T$ is the absolute temperature in Kelvin scale. The other terms retain their usual meanings. The thermal energy term in the numerator of Equation 2.10 quantifies the extent of molecular collisions. As Equation 2.10 suggests, diffusion decreases as particle size becomes larger for a given value of viscosity but is the dominant mode of transport for "point like" particles. It is important to note that hydrodynamic interactions effect diffusive particle transport near the collector surface just like it does for convection [Elimelech et al., 1995, Kemps, 2010, Nazemifard et al., 2006]. Hence, it experiences increased resistance near the wall as it tries to squeeze the fluid molecules out of the thin space during its course of vibration. To account for the hydrodynamic interactions near the surface [Honig et al., 1971, van de Ven, 1989] the particle diffusion coefficient tensor is formulated as

$$\underline{\underline{D}} = D_\infty \begin{bmatrix} f_4(H) & 0 \\ 0 & f_1(H) \end{bmatrix} \tag{2.11}$$

where $f_4(H)$ and $f_1(H)$ are the correction factors enumerated in Table 2.2.

### Colloidal Interactions and DLVO Theory

Particle transport by migration occurs due to short range (about a few hundred nanometers) colloidal interactions between the particle and the collector surfaces. Colloidal interactions are evaluated using the classical DLVO theory developed by Derjaguin and Landau [1941], and Verwey and Overbeek [1948].

The DLVO model is basically a theoretical tool which qualitatively interprets the colloidal phenomenon induced by the Lifshitz-van der Waals and electrostatic interactions. The DLVO theory is, however, approximate and is based upon a few underlying assumptions which are

- The solvent is treated as a continuum
- The ions in the solvent are point like (i.e, there is no volume associated with the ions) and they do not interact with each other and,
- The interacting bodies have smooth surfaces and are well defined geometries such as planes, spheres or cylinders.

Although, the DLVO model has been subject to controversy and criticism [Israelachvili, 1992, Kemps, 2010, Ninham, 1999], its assumptions have proven to be fairly robust in evaluating colloidal interactions for many systems [Torrie and Valleau, 1979].

As mentioned earlier, the two main components of the DLVO model are the attractive van der Waals interactions and the attractive/repulsive (depending upon the surface charge of the collector and the particle) electrostatic double layer interactions. Both these interactions play an important role in particle transport and attachment to the substrate. The van der Waals interaction energy is calculated from the classical Lenard-Jones potential which summarizes the interaction between a pair or atoms (in the particle and the collector) when they are brought very close to each other [Israelachvili, 1992].

$$U_{LJ} = \epsilon_D \left[ \left(\frac{\sigma}{r}\right)^{12} - \left(\frac{\sigma}{r}\right)^{6} \right] \tag{2.12}$$

where $\epsilon_D$ is the characteristic energy for dipolar interaction, $\sigma$ is the distance of neutral approach, and $r$ is the separation distance between the atoms. There are two well known methods for calculating the attractive van der Waals interactions, namely, the Hamaker approach [Hamaker, 1937] which is based on microscopic molecular model and the macroscopic continuum model by Lifshitz [1956]. The present study evaluates the van der Waals interactions using the Hamaker approach. It must be mentioned that the Hamaker approach uses volume integrals for calculating the van der Waals energy which might

be cumbersome when the interacting bodies are of arbitrary geometric shapes. A simplified approximation to calculate van der Waals energy, known as the Derjaguin approximation, is often used. In the Derjaguin technique, the interaction energy per unit area is calculated between two infinite planar surfaces (half spaces) over the surfaces of the interacting particles [Masliyah and Bhattacharjee, 2006]. Further, van der Waals interaction energy can be retarded (Born repulsion [Hunter, 2001]) or unretarded depending upon whether the repulsive part ($r^{12}$) of the Lenard-Jones potential in Equation 2.12 is considered. In reality, when two atoms are brought very close to each other (0.1 nm), their electron clouds overlap resulting in strong repulsive forces known as Born repulsion [Hunter, 2001]. The non-retarded sphere-plate interaction energy based on Derjaguin approximation is given as

$$\phi_{DA} = -\frac{A_H \ a_p}{6h} \tag{2.13}$$

and the non-retarded interaction energy based on Hamaker approach is

$$\phi_{Ham} = -\frac{A_H}{6}\left[\frac{a_p}{h} + \frac{a_p}{h+2a_p} + \ln\left(\frac{h}{h+2a_p}\right)\right] \tag{2.14}$$

with $A_H$ being the Hamaker constant. The retarded van der Waals interaction based on Derjaguin approximation is given by [Schenkel and Kitchener, 1960]

$$\phi_{r,DA} = -\frac{A_H a_p}{6h}\left[\frac{1}{1+11.12h/\lambda}\right] \tag{2.15}$$

whereas the corresponding expression based on Hamaker approach is [Czarnecki, 1979]

$$\begin{aligned}\phi_{r,Ham} &= -\frac{A_H\lambda}{12\pi}\left[\frac{2.45}{5}\left(\frac{h-a_p}{h^2} - \frac{h+3a_p}{(h+2a_p)^2}\right)\right. \\ &- \frac{2.17\lambda}{60\pi}\left(\frac{h-2a_p}{h^3} - \frac{h+4a_p}{(h+2a_p)^3}\right) \\ &+ \left.\frac{0.59\lambda^2}{420\pi^2}\left(\frac{h-3a_p}{h^4} - \frac{h+5a_p}{(h+2a_p)^4}\right)\right]\end{aligned} \tag{2.16}$$

where $\lambda = 100$ nm. $h$ and $a_p$ retain their usual meanings as before. It is important to note that all four expressions indicate that the interaction energy diminishes as particle size decreases. Thus

$$\phi_{vdW} \rightarrow 0 \quad as \quad a_p \rightarrow 0 \tag{2.17}$$

Equation 2.17 will have important implications in determining the correct limiting mass transport behavior when the single collector efficiency is evaluated.

In addition to the van der Waals interaction energy, electrostatic interactions also play a key role in particle transport and deposition. Solid surfaces in aqueous solution often acquire different surface charges as a result of which they interact [Hogg et al., 1966]. Acquisition of surface charge may be due to ionization of surface groups, physical restriction of a particular type of ion to one phase or specific affinity of surfaces towards ions. In order to maintain electro-neutrality, an excess amount of oppositely charged ions (counter-ions) arrange themselves next to the surface and a deficit of an equal amount of similarly charged ions (co-ions) is created simultaneously. This redistribution of ions in solutions gives rise to the Electrostatic Double Layer (EDL) [Hunter, 1981]. The Stern model is often used to describe the double layer [Hiemstra and VanRiemsdijk, 1996, Westall and Hohl, 1980] interactions between surfaces in solution. According to this model, outside the Stern layer (which is the immobile layer of counter ions adjacent to the surface), the mobile counter ions are distributed and their motion is balanced by the electrostatic attraction and the diffusion due to thermal energy. This layer of mobile counter ions is called the diffuse layer. Electrostatic double layer interactions take place when the diffuse layers of two approaching surfaces overlap [Nazemifard, 2006]. The EDL interaction energy, assuming constant surface potential on the particle and the collector and symmetric (z:z) electrolyte, is given by the Hogg Healy Fuerstenau (HHF) [Hogg et al., 1966] expression

$$\phi_{EDL} = \pi\epsilon a_p \left\{ 2\psi_s\psi_p \ln\left[\frac{1+\exp(-\kappa h)}{1-\exp(-\kappa h)}\right] + (\psi_s^2+\psi_p^2)\ln[1-\exp(-2\kappa h)\right\} \tag{2.18}$$

where $\psi_s, \psi_p$ are the surface potentials on the collector and the particle respectively, and $\kappa$ is the inverse Debye length [Hunter, 1981, Masliyah and Bhattacharjee, 2006] given by the expression

$$\kappa = \sqrt{\frac{2n_\infty z^2 e^2}{\epsilon_0 \epsilon k_B T}} \tag{2.19}$$

Here $n_\infty$ is the bulk ionic number concentration of the electrolyte, $\epsilon$ is the solvent dielectric constant and $\epsilon_0$ is the permitivity of vacuum. Depending upon the signs of the surface potentials, the EDL interactions can be attractive or repulsive in nature.Both the van der Waals interaction energy and EDL energy expressions used in the present study apply to a spherical particle interacting with a flat plate. Although the sphere-in-cell model defines a spherical collector, the ratio of the collector to particle size is very large (>100) which allows the sphere-flat plate approximation. Thus, near the surface, the particle does not feel the curvature effect of the collector due to the large size of the collector compared to that of the particle.

Summarizing all the three particle transport mechanisms, it can be proven mathematically as well as logically that for small particles convection and colloidal interactions are negligible as is hydrodynamic interaction. These transport mechanisms start taking effect only as particle size becomes large. For small particles the dominant mode of transport and deposition is diffusion. Figure 2.3 schematically depicts the three modes of particle transport near the collector surface. With this background, the obvious question is what is the definition of a small particle? At what particle size does hydrodynamic and colloidal interactions cease to have any significant effect on particle transport and deposition?

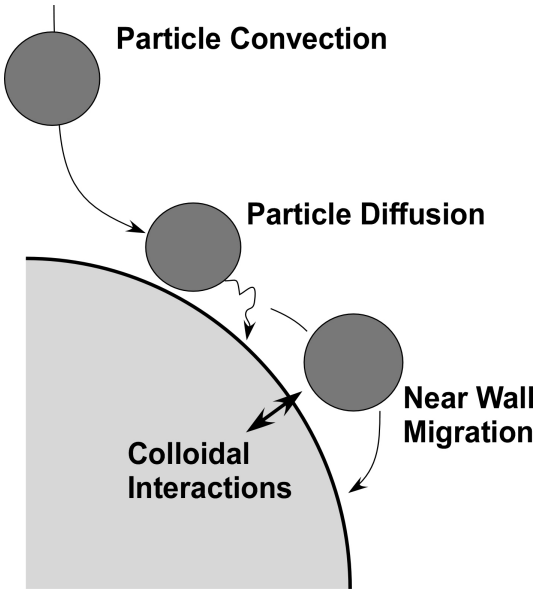


**Figure 2.3** – Schematic depicting all three modes of particle transport near the collector surface

## 2.3 Limiting Deposition Behavior and Levich Equation

As previously discussed, the three mechanisms of particle transport predominate at different length scales and particle sizes. The non-dimensional mass transport coefficient (Sherwood number, $Sh$) in the absence of hydrodynamic retardation and colloidal interactions was given by [Levich, 1962]. According to the analytical Levich solution, the Sherwood number and Peclet number (which is the ratio of particle convection to particle diffusion), for a packed bed, are related as

$$Sh \propto Pe^{1/3} \qquad (Pe >> 1) \tag{2.20}$$

It has already been discussed that both hydrodynamic retardation and the colloidal interactions become insignificant for "point-like particles" and diffusion is the predominant mode of particle transport in such cases. Hence for such strongly diffusive systems, Levich equation should be the valid limiting condition for predicting the Sherwood number. Some earlier studies [Rajagopalan and Tien, 1976, Ruckenstein, 1964, van de Ven, 1989, Yao et al., 1971] es-

tablished that for all particle sizes upto 1 micron, Levich equation is valid. van de Ven [1989] argued that in the absence of electrostatic interactions and below 1 micron particle size, the hydrodynamic retardation forces balance the attractive van der Waals interactions thereby adhering to the Levich solution. This claim, however, is hypothetical and there is no mathematical proof that the two factors counter each other below 1 micron particle size. In a recent article by Tufenkji and Elimelech [2004], it was highlighted that the Levich solution is not the true limiting behavior even for Brownian particles. This has instigated a debate regarding the limiting mass transport behavior for the sphere-in-cell model. There is a rift between the two schools of thought, one which agrees with the Levich solution [Long and Hilpert, 2009, Nazemifard et al., 2006, Rajagopalan and Tien, 1976, Yao et al., 1971] and the other which does not [Civan, 2010, Lin et al., 2008, Tufenkji and Elimelech, 2004]. It is thus important to establish the correct fundamental limiting behavior before investigating complicated deposition systems.

## 2.4 A Review of Existing Models Predicting Particle Deposition onto Homogenous Attractive Collectors: Limiting Case Conjectures

As discussed earlier, in colloid filtration theory, the most important link between the micro-scale physics of particle deposition around a single collector and the macroscopic filtration efficiency (or filter coefficient) of a granular packed bed is the initial deposition rate of colloidal particles onto a clean collector grain, generally referred to as the single collector efficiency. Over the years, various models have evolved for evaluation of single collector efficiency. In this section, a comprehensive review of these models are discussed. In all these models, the effect of the EDL interactions has not been considered.

The first comprehensive study on an isolated spherical collector was conducted by Ruckenstein [Ruckenstein, 1964]. Following this, cell models for an assemblage of spherical collectors were used extensively as a means of elucidating the mechanisms of colloid filtration by granular porous media [Kemps and Bhattacharjee, 2009, Nelson and Ginn, 2005, Prieve and E, 1974, Rajagopalan

and Tien, 1976, Tufenkji and Elimelech, 2004]. Recently, Ma and Johnson [2010] developed a theoretical model for evaluating single collector efficiency on a hemisphere-in-cell model incorporating grain to grain contact. Among various methods, Eulerian and Lagrangian particle transport models employing the Happel sphere-in-cell model [Happel, 1958] to describe the flow field remains the most widely used approach for this purpose. In a study by Long and Hilpert [2009], Lattice Boltzmann method has also been used to evaluate single collector efficiency. Although these models qualitatively indicate similar deposition trends, over the recent years, some confusion seems to have crept in literature related to the description of the diffusion dominated deposition rendering significant differences in the slope of the overall single collector efficiency curve for Brownian particles.

Yao et al. [1971] provided the first model to calculate single collector efficiencies for Brownian and non-Brownian particles by considering the finite size of the particles. This work proposed the additivity rule by which the overall single collector efficiency could be evaluated by adding the contributions from the three mechanisms of diffusion, interception, and gravity. A Lagrangian analysis using the additivity principle was performed by Rajagopalan and Tien [Rajagopalan and Tien, 1976] in developing their correlation for particle deposition efficiency, referred hereafter as the RT correlation. The RT correlation improved upon the Yao et al. [1971] correlation by accounting for the attractive van der Waals interaction between the particle and the collector, as well as, by incorporating the hydrodynamic retardation of the particle owing to its proximity to the collector on the convective and migration transport (both deterministic) terms. However, Rajagopalan and Tien, who only calculated the deterministic particle trajectories, simply added the Levich solution to their trajectory analysis results assuming the linear additivity principle to obtain their correlation. In this respect, both the Yao et al. [1971] and RT [Rajagopalan and Tien, 1976] results revert to the classical Levich solution for purely diffusive systems. Neither of these solutions explicitly account for hydrodynamic interactions on the diffusive particle transport. A comprehensive summary of these early correlations is given in Elimelech et al. [1995]

Tufenkji and Elimelech [2004] developed a new correlation, referred hereafter as the TE correlation, for predicting single collector efficiency for the

sphere-in-cell geometry by numerically solving the convection-diffusion-migration equation. The TE correlation is obtained by performing a regression analysis on the results obtained from a numerical solution of the governing transport equations. The Eulerian approach adopted by Tufenkji and Elimelech in developing the correlation can be considered the most rigorous because of the following reasons: (i) All three transport mechanisms are considered fully coupled through the governing equation, and are not linearly combined; and, (ii) the hydrodynamic retardation effects are considered in the particle diffusion term in addition to convection and migration. The single collector efficiency predicted by the TE correlation, however, has a distinct deviation from the Levich slope, and hence, from the slope of the RT correlation in the diffusion dominated regime. The authors attribute this deviation to the van der Waals attraction and the hydrodynamic retardation, which were not considered in Levich's solution [Rajagopalan and Tien, 2005, Tufenkji and Elimelech, 2005].

Brownian trajectory analysis of the same problem was later performed by Nelson and Ginn [2005] and Kemps and Bhattacharjee [2009]. Both these works take into account the van der Waals interaction between the particle and the collector. Although both these studies included the diffusional transport mechanism directly in the particle tracking model, the Brownian motion term in the original Nelson and Ginn model did not consider hydrodynamic retardation. In contrast, the model of Kemps and Bhattacharjee considered hydrodynamic retardation in the Brownian motion term. The single collector efficiencies predicted by Kemps and Bhattacharjee tend to agree closely with the RT correlation in the diffusion dominated region. In contrast, the original work of Nelson and Ginn predicted a consistently lower single collector efficiency in the diffusion dominant regime, which was later corrected and their revised results [Nelson and Ginn, 2009] agree well with the RT correlation values using the Lagrangian approach. However, Nelson and Ginn depicted in their comment [Nelson and Ginn, 2009] that the diffusive regime of the single collector efficiency vs. particle diameter plot can attain different values depending on how the hydrodynamic interactions have been included in the particle tracking model. Notwithstanding these, the slopes of the single collector efficiency plots against particle diameter obtained from the Lagrangian models used by Kemps and Bhattacharjee [2009] as well as Nelson and Ginn [2005, 2009] tend to follow the slope of the RT plot in the diffusion dominated

(small particle size) regime. It has been shown more recently that the slope of single collector efficiency vs. particle size curve for strongly diffusive systems agrees with the Levich slope even when collector grain-to-grain contact is considered in a hemisphere-in-cell geometry, which retains most of the attributes of Happel's cell model [Ma and Johnson, 2010, Ma et al., 2009]. However, these authors have also used Brownian trajectory analysis. The correlation developed by Long and Hilpert [2009] using Lattice Boltzmann simulations also indicates that the Levich slope is correct for Brownian particles.

This brings us to one of the central question to be addressed in this thesis. One would expect that as the particle size becomes smaller, or the deposition process becomes diffusion dominated, all colloid deposition model predictions should approach the classical Levich behavior in two ways. First, the single collector efficiency will become proportional to $Pe^{-2/3}$. Second, in the limit of point like particles, the single collector efficiency should approach unity. This limiting behavior is automatically ensured in all trajectory model based correlations which do not explicitly calculate Brownian motion, but utilize the Levich solution in the diffusion dominated regime [Rajagopalan and Tien, 1976, Yao et al., 1971]. It also appears that Lagrangian methods that explicitly incorporate Brownian motion also respect this limiting behavior [Kemps and Bhattacharjee, 2009, Nelson and Ginn, 2005, 2009]. Finally, for most geometrically well-defined (ideal) deposition systems, such as stagnation point flow, parallel-plate channel, slot impinging jet, isolated spherical collector, and rotating discs, these limiting Levich trends are always recovered as the particle size is diminished [Adamczyk and van de Ven, 1981, Adamczyk et al., 1978, 1983, Dabros and Adamczyk, 1979, Dabros and van de Ven, 1983, Nazemifard et al., 2006, Ruckenstein, 1964]. In sharp contrast, for the Happel cell geometry involving a spherical collector, the rigorous Eulerian calculations done by Tufenkji and Elimelech seem to show a different slope in the diffusion dominated regime, rendering the single collector efficiency to be proportional to $Pe^{-0.715}$ in the Tufenkji-Elimelech (TE) correlation [Tufenkji and Elimelech, 2004].

Use of the TE correlation gives rise to two discrepancies from the Levich solution. As the particle size becomes smaller, a mass transfer correlation must revert to the Levich slope magnitude of $-2/3$, which the TE correlation

| Correlation | Expression for single collector efficiency ($\eta_0$) |
|---|---|
| Yao et al. [1971] | $4.04N_{Pe}^{-2/3} + \frac{3N_R^2}{2} + N_G$ |
| Rajagopalan and Tien [1976] | $4A_s^{1/3}N_{Pe}^{-2/3} + A_sN_{Lo}^{0.125}N_R^{1.875} + 0.0038A_sN_G^{1.2}N_R^{-0.4}$ |
| Tufenkji and Elimelech [2004] | $2.4A_s^{1/3}N_R^{-0.081}N_{Pe}^{-0.715}N_{vdw}^{0.052} + 0.55A_sN_R^{1.675}N_A^{0.125} + 0.22N_R^{-0.24}N_G^{1.11}N_{vdw}^{0.053}$ |
| Long and Hilpert [2009] | $(15.56 \pm 0.21)\frac{(1-\epsilon)^3}{\epsilon}N_{Pe}^{-0.65\pm0.023}N_R^{0.19\pm0.03} + 0.55A_sN_R^{1.675}N_A^{0.125} + 0.22N_R^{-0.24}N_G^{1.11}N_{vdw}^{0.053}$ |
| Ma and Johnson [2010] | $\gamma^2[2.3A_s^{1/3}N_R^{-0.080}N_{Pe}^{-0.65}N_A^{0.052} + 0.55A_sN_R^{1.8}N_A^{0.15} + 0.2N_R^{-0.10}N_G^{1.1}N_A^{0.053}N_{Pe}^{0.053}]$ |

**Table 2.3** – Single collector efficiency correlations by various researchers.

fails to attain, and second, when the particle size approaches zero, the TE correlation predicts values of the single collector efficiency that are above 1. Thus, although there is excellent agreement between the TE correlation and a host of independent experimental data on colloid filtration [Godinez and Darnault, 2011, Phenrat et al., 2010, Sunkara et al., 2010, Torkzaban et al., 2010], the fundamental mass transfer characteristics of the deposition process in the Brownian regime seem to be missing in the TE correlation. These fundamental limiting behaviors must be ensured in a correlation to render them theoretical as opposed to empirical. To the best of our knowledge, this discrepancy has still not been resolved [Petosa et al., 2010]. A list of available correlation to evaluate single collector efficiency is provided in Table 2.3 while the list of non dimensional numbers used in the correlations is given in Table 2.4.

| Parameter | Definition | Meaning |
|---|---|---|
| $N_R$ | $a_p/a_c$ | Interception Number |
| $N_{Pe}$ | $2Ua_p/D_\infty$ | Peclet Number |
| $N_{Lo}$ | $4A_H/(9\pi\rho_f\nu(2a_p)^2U)$ | London Number, $A_H$ is the Hamaker constant |
| $N_G$ | $(2a_p)^2(\rho_p-\rho_f)g/18\rho_f\nu U$ | Gravity Number |
| $N_A$ | $A_H/3\pi\rho_f\nu(2a_p)^2U$ | Attraction Number |
| $N_{vdW}$ | $A_H/k_BT$ | van der Waals Number |

**Table 2.4** – List of non-dimensional numbers used in the correlations of Table 2.3.

An important observation from Table 2.3 is that barring the Tufenkji and

Elimelech [2004] correlation, the exponent of the Peclet number in allthe other correlations is $-2/3$ which is the Levich solution. In the following chapters, the cause of this discrepancy will be discussed and a closure correlation for evaluating single collector efficiency will be presented.

## 2.5 Surface Heterogeneity and its Role in Particle Deposition

The discussions in the previous sections of this chapter delved into particle transport and deposition onto smooth homogeneous surfaces. Rarely are real surfaces smooth and uncharged in aqueous solution. In a quest to develop more sophisticated and realistic models for particle deposition, a lot of focus has been laid on experimental and theoretical studies dealing with surface heterogeneity [Hoek et al., 2003, Sun and Walz, 2001]. Surface heterogeneity can be either in the form of physical heterogeneity due to roughness [Saiers and Ryan, 2005] or chemical heterogeneity due to non-uniform distribution of charged species [Duffadar and Davis, 2008, Rizwan and Bhattacharjee, 2009]. In most real systems physical and chemical heterogeneity are concurrent. However, incorporating both effects together poses challenges towards systematic analysis and it is rare to find such models [Kemps, 2010].

Several models to study the effect of physical heterogeneity on the interactions energies and particle deposition [Das and Bhattacharjee, 2005, Henry et al., 2011, Herman and Papadopoulos, 1990, Kemps and Bhattacharjee, 2005, 2009, Saiers and Ryan, 2005] have been developed since the initial works by Czarnecki [1986], Czarnecki and Dabros [1980]. Reduced energy barrier to particle deposition in presence of surface heterogeneity compared to a smooth surface was a reported by Suresh and Walz [1996]. Similarly, Zhao and Mason [2008] determined the depletion interaction potential for both ordered and disordered surface roughness and explained the self-assembly of rough platelets using the model. Chen et al. [2010] demonstrated that greater surface roughness of like samples resulted in higher colloid deposition even for roughness dimensions which were two orders of magnitude smaller than the colloidal particles. Most of these studies have focussed on modeling physical heterogeneity on planar substrates. To the best of our knowledge, a recent article

by Saiers and Ryan [2005] is the only work that deals with surface roughness on a sphere-in-cell geometry but does not consider chemical heterogeneity. The present body of work focuses on the effects of chemical heterogeneity on particle deposition in a sphere-in-cell model with an otherwise smooth surface.

Chemically patchy surfaces are ubiquitous in natural and engineered systems as collectors or adsorbents in a wide gamut of applications spanning water treatment [Loveland et al., 2003], environmental remediation [Miller et al., 2010], biomedical devices [Bendersky and Davis, 2011, Kalasin and Santore, 2010, Pegueroles et al., 2010] and molecular diagnostics [Soliman et al., 2010]. Like in the case of physical heterogeneity, there has been a lot of research dealing with particle deposition onto planar chemically heterogeneous substrates [Bendersky and Davis, 2011, Duffadar and Davis, 2008, Kalasin and Santore, 2010, Kemps and Bhattacharjee, 2005, Nazemifard et al., 2006, Rizwan and Bhattacharjee, 2009]. However, there is a paucity of rigorous models of particle deposition onto chemically patterned substrates in other geometries, such as spherical collectors [Kemps and Bhattacharjee, 2009]. It is of interest to note that such chemically heterogeneous surfaces are also widely encountered in porous media flows [Chen et al., 2001, Shellenberger and Logan, 2002, Song et al., 1994, Vaidyanathan and Tien, 1991]. In naturally occurring substrates, the charge heterogeneity is random and of arbitrary geometric shapes rendering it almost impossible for systematic evaluation of deposition characteristics on such substrates [Ryan and Elimelech, 1996]. It is therefore important to devise a technique to systematically define the charge heterogeneity on the surface of the collector such that particle transport modeling and analysis is tractable. Surface patterning remains one of the most widely used techniques to model chemical heterogeneity with regards to particle deposition [Nazemifard et al., 2006, Rizwan and Bhattacharjee, 2009].

Several experimental studies dealing with particle deposition onto planar patterned surfaces have been reported. Chen et al. [2000] demonstrated self-organization of $SiO_2$ and polystyrene particles onto patterned polyelectrolyte substrate. Similarly, Zheng et al. [2002] discussed methods to develop small scale patterned features onto multi-layer polyelectrolyte substrates and use them as templates for controlled particle deposition. Interestingly, various experimental works on spherical particles with surface patchiness have also been

reported. Binks and Fletcher [2001] showed how the amphiphilicity of Janus particles can be tuned to influence the strength of particle adsorption. Petit et al. [2001] discussed techniques to adsorb gold nanoclusters on the surface of only one hemisphere of silica nanobeads thereby giving it Janus characteristics. Molecular simulations were performed by Zhang and Glotzer[Zhang and Glotzer, 2004] to investigate the self assembly of particles with discrete patches of attractive sites on their surface. Recent development in state-of-the-art fabrication technology has enabled facile production of such particles with chemical anisotropy in bulk [Perro and Manoharan, 2010]. Numerous applications of such patchy or Janus particles have been also been reported reported [Walther and Mueller, 2008], including their use as nanomotors [Wheat et al., 2010], emulsion stabilizers [Bormashenko et al., 2011], ion exchange clusters [Pardhy and Budhlall, 2010], optical probes for rheological measurements [Behrend et al., 2004], nanoscale chemical locomotion [Howse et al., 2007] to name a few. Surprisingly however, not much has been reported with respect to particle deposition onto such patchy and Janus spherical collectors. This thesis reports particle deposition onto such patchy and Janus spherical collectors employing patterning techniques to mimic the patchiness. The analysis opens up a frontier in artificially prepared porous media for studying particle transport and deposition.

Of the available methods to evaluate particle transport over charged heterogeneous surfaces, the patchwise heterogeneity model remains the most widely used[Elimelech et al., 2003, Erickson and Li, 2002, Mamleev et al., 2002]. In this model, two types of surface charge is defined on the collector surface and the surface area fraction occupied by one type of surface charge is evaluated using a two site averaging process [Nazemifard et al., 2006, Rizwan and Bhattacharjee, 2009]. It has, however, been pointed out that the spatial averaging in patch models gives accurate results only for macroscopic surface heterogeneity (i.e. when the patch dimensions are much larger than the particle dimensions) but disintegrates when the patch size is comparable to that of the particle [Elimelech et al., 2003, Nazemifard et al., 2006]. Since the analysis in this work involves surface patterns of dimensions comparable to the particle size, deviations from the patchwise heterogeneity model for the sphere-in-cell geometry are explored.

In addition to modeling porous media as planar and assmblage of spherical collectors, investigating particle transport in micropores is also important. For simplicity, the micropores can be approximated as microchannels and heterogeneity can be incorporated to render realism to the model. Transport of particles suspended in a carrier fluid in micro/nano scale channels is central to numerous microfluidic and nanofluidic systems. Lab-on-Chip (LOC) systems [Felten et al., 2008], flow of biomolecules in microchannels and micro capillaries [Waghmare and Mitra, 2010a], porous media flows [Sbai and Azaroual, 2011], chromatographic analysis [Bernate and Drazer, 2011], membrane separations [Bacchin et al., 2011, Das et al., 2003] are some of the examples of such systems in which particle transport in micro and nano channels is ubiquitous. Adamczyk and van de Ven [1981] investigated particle transport and deposition in narrow homogeneous cylindrical channels almost three decades back. Since then, fundamental concepts of particle transport has been used in various microfluidic applications. Waghmare and Mitra [2010a] discussed the transport of microbead suspension in rectangular capillaries. In a recent article by Fridjonsson et al. [2011], NMR microscopy and CFD simulations were used to investigate transport of fluids with colloidal suspensions in a bifurcated capillary system. The study was linked to applications in microvascular physiology and other microfluidic devices. Waghmare and Mitra [2010b] have also investigated transport of biomolecules and cells through buffer solution in microchannels for immunoassay based sensing devices. Saadatmand et al. [2011] focussed on blood transport in a capillary tube to investigate mixing in biomedical microdevices and microcirculation. Several other similar applications for particle transport in micro and nano channels can be found in literature [Chein and Dutta, 2009, Gudipaty et al., 2011, Zhao et al., 2010].

As in other real geometries, surface heterogeneity (in the form of surface roughness or chemical heterogeneity) is inevitable in these microchannel walls as well. Erickson and Li [2003] investigated electroosmotic flow in a microchannel with patchwise surface heterogeneity. A similar study to investigate electroosmotic flow in a circular microchannel with periodic surface potentials was performed by Yang et al. [2004]. Although a lot of theoretical investigations have been performed to analyze electrolyte transport in these microfluidic and nanofluidic systems [Liu et al., 2011, Santillo et al., 2011, Waghmare and Mitra, 2009, 2010], there is no significant theoretical model which predicts

particle transport and deposition in microchannels considering the effects of the surface heterogeneities. The last section of this thesis delves into particle transport modeling in such chemically patterned microchannels. Using simple approximations as in other porous media geometries, the deposition characteristics onto the walls of the microchannel is discussed and possible applications in microfluidic/nanofluidic systems are presented.

## 2.6 Summary

It is evident from the literature review of this chapter that although colloid transport is a mature subject, there is confusion regarding the fundamental mass transport behavior in the sphere-in-cell model. Further, effects of chemical heterogeneity on particle transport and deposition in non-planar geometries have still not been rigorously investigated, especially from the theoretical standpoint. With this basic premise, the present work aims to develop an enhanced understanding of the fundamental mass transport behavior in the Happel sphere-in-cell geometry, explore the effects of surface chemical heterogeneity in modifying particle transport in non-planar geometries (sphere-in-cell model and microchannels) and discuss applications of tuning these chemically heterogeneous substrates in designing efficient deposition systems pertinent to porous media and microfluidic/nanofluidic transport. The next chapter introduces a model for investigating particle deposition onto a homogeneous favorable spherical collector in the absence of double layer interactions.

# Chapter 3

# Colloid Deposition onto Homogenous Collectors in Absence of Double Layer Interactions

## 3.1 Introduction

In this chapter, an Eulerian model for colloid deposition onto a spherical collector representing a porous medium employing the Happel sphere-in-cell geometry is presented. The convection-diffusion-migration (C-D-M) equation is numerically solved to evaluate the particle deposition efficiency (single collector efficiency) as a function of particle radius and the contribution of each of the transport mechanisms to the single collector efficiency is described. The study includes a comprehensive assessment of several hitherto unexplored aspects of colloid transport involving cell models. These include: influence of different expressions for the unretarded and retarded van der Waals interactions used in the analysis, which turns out to be highly insightful, the suitability of Dirichlet and Neumann boundary conditions in conjunction with the cell model, and complications that can arise due to overlap of the concentration and Happel (momentum) boundaries. The implications of pairwise additivity of the transport mechanisms, and regimes of validity of such simplifications are systematically revisited. The objective of this chapter is to present a theoretically consistent interpretation of the results obtained from the various deposition models in porous media. Finally, a new correlation predicting single collector efficiency for deposition of colloidal particles onto a packed bed of

spherical collectors is presented. The correlation represents an improvement to the existing correlations for predicting single collector efficiency, especially for Brownian particles.

## 3.2 Numerical Formulation of the Problem

### 3.2.1 Sphere-in-cell Geometry

Figure 3.1(a) depicts the sphere-in-cell geometry for the spherical collector with the Happel fluid envelope, as well as, the relative directions of the convection and gravity. The system considered here is identical to the model considered in most of the earlier studies, either Eulerian or Lagrangian [Kemps and Bhattacharjee, 2009, Nelson and Ginn, 2005, Rajagopalan and Tien, 1976, Song and Elimelech, 1992, Tufenkji and Elimelech, 2004]. We use a spherical coordinate system assuming azimuthal symmetry. Figure 3.1(b) depicts the geometric parameters, as well as the forces and velocities acting on a spherical particle in the fluid envelope. The particle radius is $a_p$, $h$ denotes the normal surface to surface separation distance between collector and particle, whereas $v_r$ and $v_\theta$ denote the radial and tangential particle velocity components, respectively, in the spherical coordinate system. The forces considered are the attractive van der Waals force between the particle and the collector ($F_{vdW}$), and gravity ($F_g$). The direction of gravity depends on the density of the particle relative to the fluid. For a particle heavier than the fluid, the direction of gravity is as shown. The model can be employed to calculate deposition under both gravity assisted and gravity hindered conditions.

### 3.2.2 Governing Equations

The governing transport equation is the well-known steady-state convection diffusion-migration equation Elimelech et al. [1995], Masliyah and Bhattacharjee [2006], Tufenkji and Elimelech [2004], van de Ven [1989]

$$\nabla \cdot \left[ \mathbf{v}c - \underline{\underline{D}} \cdot \nabla c + \frac{\underline{\underline{D}} \cdot \mathbf{F}}{k_B T} c \right] = 0 \tag{3.1}$$

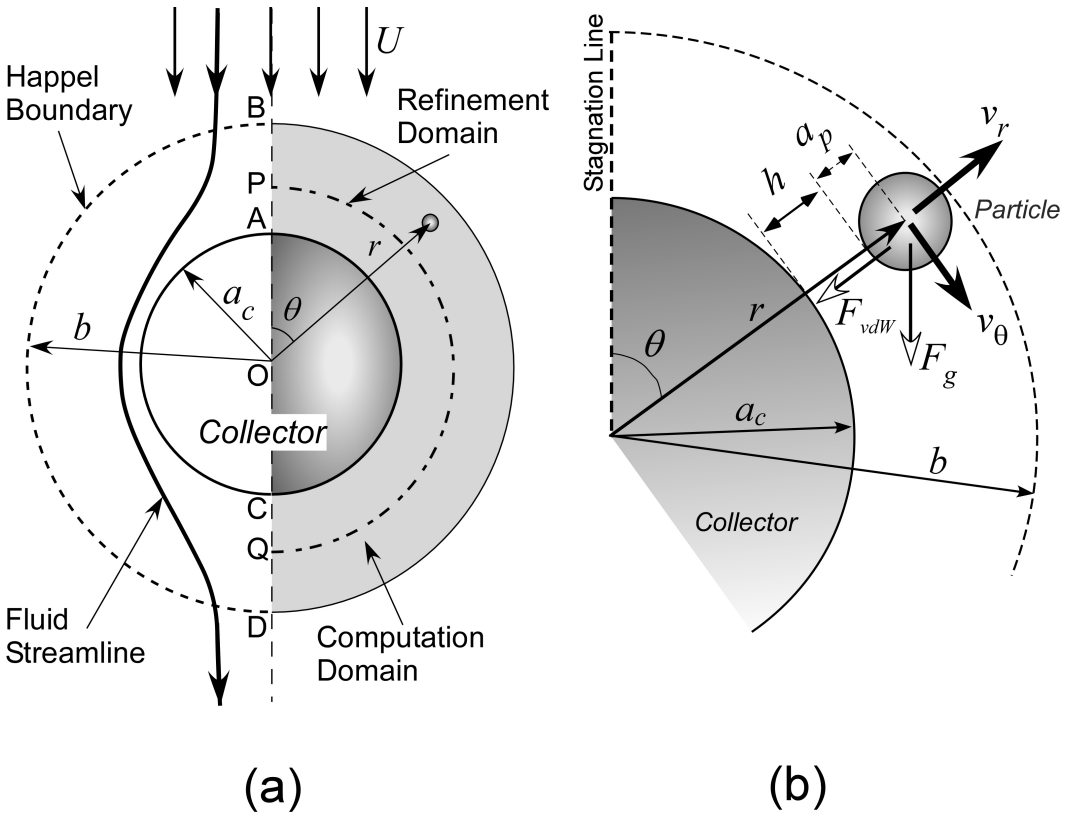


**Figure 3.1** – (a) Spherical collector with a Happel fluid cell. The vertical dashed line represents the line of symmetry. The right half of the diagram represents the computational domain within the fluid envelope (ABDC). The curve PQ denotes the region within which the mesh refinement is applied. (b) Velocity components and the forces acting on a particle in the fluid cell. The particle radius is $a_p$, $h$ denotes the normal surface to surface separation distance between collector and particle. $v_r$ and $v_\theta$ denote the radial and tangential particle velocity components in the spherical coordinate system. The forces considered are the particle-collector van der Waals attraction ($F_{vdW}$) and gravity ($F_g$).

where $\mathbf{v} \equiv (v_r, v_\theta)$ is the particle velocity vector, $c$ is the particle concentration, $\underline{\underline{D}}$ is the diffusion tensor, $k_B$ is the Boltzmann constant, $T$ is the absolute temperature and $\mathbf{F}$ is the sum of all the non-hydrodynamic (*i.e.*, van der Waals and gravity) forces acting on the particle. Equation 3.1 can be solved if the particle velocity, the diffusion tensor and the sum of the external forces acting on the particle are defined.

The undisturbed fluid velocity, $\mathbf{u} \equiv (u_r, u_\theta)$, is obtained from the Happel solution of the Stokes equation [Elimelech et al., 1995, Tien, 1989] by calcu-

lating the derivatives of Equation 2.7. The expressions for the scaled fluid velocities in the radial and tangential directions are given as

$$U_r = u_r/U = -cos\theta \left[ K_1 \left(\frac{a_c}{r}\right)^3 + K_2 \left(\frac{a_c}{r}\right) + K_3 + K_4 \left(\frac{r}{a_c}\right)^4 \right] \tag{3.2}$$

$$U_\theta = u_\theta/U = \frac{sin\theta}{2} \left[ -K_1 \left(\frac{a_c}{r}\right)^3 + K_2 \left(\frac{a_c}{r}\right) + 2K_3 + 4K_4 \left(\frac{r}{a_c}\right)^2 \right] \tag{3.3}$$

The expressions for the porosity dependent factors $K_1$, $K_2$, $K_3$, $K_4$ have been listed in Table 2.1. The particle velocities are calculated from the undisturbed fluid velocities by incorporating the hydrodynamic correction functions as [Elimelech, 1994, Nazemifard et al., 2006] $v_r = f_1(H)f_2(H)u_r$ and $v_\theta = f_3(H)u_\theta$, where $H$ is the dimensionless surface to surface separation distance between the particle and the collector (defined as $H = h/a_p$). To account for the hydrodynamic interactions on the Brownian diffusion, [van de Ven, 1989] the diffusion tensor terms incorporating the hydrodynamic interactions is formulated as, $D_{rr} = f_1(H)D_\infty$ and $D_{\theta\theta} = f_4(H)D_\infty$, where $D_\infty$ is the Stokes-Einstein diffusion coefficient. The functions $f_1(H)$, $f_2(H)$, $f_3(H)$ and $f_4(H)$ are the universal hydrodynamic correction functions [Elimelech, 1994, Goldman et al., 1967, Kemps and Bhattacharjee, 2009, Masliyah and Bhattacharjee, 2006, Nazemifard et al., 2006] as explained in Chapter 2. The expressions for these functions used in the present study are listed in Table 2.2.

The net radial force includes the radial component of the gravitational force ($F_g$) and the attractive van der Waals force ($F_{vdW}$) between the particle and the collector:

$$F_r = -\frac{d\phi_T}{dr} - \frac{4}{3}\pi a_p^3(\rho_p - \rho_f)g \ \cos\theta \tag{3.4}$$

where $\phi_T$ is the van der Waals interaction energy in this study. Although it is trivial to add electrostatic interactions in the model, we have not included

these interactions in our analysis presented in this paper simply because inclusion of electrostatics is not warranted for the discussion at hand.

The van der Waals interaction energy between the particle and collector can be expressed in four different ways. Two expressions of the interaction energy can be obtained based on Hamaker's microscopic approach (one including electrodynamic retardation and the other without). The other two additional expressions are possible based on Derjaguin's approximation (again, one considering retardation and the other not). We consider all these four expressions in our calculations because they have all been used in prior studies, However, no previous study has compared the influence of these different expressions on the prediction of the single collector efficiency. The 4 possible van der Waals interaction energies are given by Equations 2.13, 2.14, 2.15, 2.16.

The net tangential force on the particle arises from gravity, yielding

$$F_\theta = \frac{4}{3}\pi a_p^3(\rho_p - \rho_f)g \ \sin\theta \tag{3.5}$$

In the above expressions, $a_p$ is the particle radius, $\rho_p$ and $\rho_f$ are the particle and fluid densities, respectively, and $g$ is the gravitational acceleration.

The explicit non-dimensionalization form of the governing equation (Equation 3.1) [Elimelech, 1994, Elimelech et al., 1995] can be expressed as

$$\begin{aligned}\nabla\cdot(\mathbf{v}c) = f_1(H)f_2(H)u_r\frac{\partial c}{\partial r} + \frac{f_3(H)u_\theta}{r}\frac{\partial c}{\partial r} + \Bigg[f_1(H)f_2(H)\frac{\partial u_r}{\partial r} \\ + f_1(H)u_r\frac{\partial f_2(H)}{\partial r} + f_2(H)u_r\frac{\partial f_1(H)}{\partial r} \\ + \frac{2}{r}f_1(H)f_2(H)u_r + \frac{2}{r}f_3(H)u_\theta cot\theta\Bigg]c\end{aligned} \tag{3.6}$$

$$\begin{aligned}\nabla\cdot(\underline{\underline{D}}\cdot\nabla c) = \Bigg[f_1(H)\frac{\partial^2 c}{\partial r^2} + \frac{2f_1(H)}{r}\frac{\partial c}{\partial r} + \frac{\partial f_1(H)}{\partial r}\frac{\partial c}{\partial r} + f_4(H)\frac{cot\theta}{r^2}\frac{\partial c}{\partial\theta} \\ + \frac{f_4(H)}{r^2}\frac{\partial^2 c}{\partial r^2}\Bigg]D_\infty\end{aligned} \tag{3.7}$$

$$\nabla \cdot \left( \frac{\underline{\underline{D}} \cdot \mathbf{F}}{k_B T} c \right) = \left( \left[ \frac{2 f_1(H) F_r}{r k_B T} + \frac{F_r}{k_B T} \frac{\partial f_1(H)}{\partial r} + \frac{f_1(H)}{k_B T} \frac{\partial F_r}{\partial r} + \frac{f_4(H) F_\theta \; cot\theta}{r k_B T} + \frac{f_4(H)}{r k_B T} \frac{\partial F_\theta)}{\partial \theta} \right] c + \frac{f_1(H) F_r}{k_B T} \frac{\partial c}{\partial r} + \frac{f_4(H) F_\theta}{r k_B T} \frac{\partial c}{\partial \theta} \right) D_\infty \tag{3.8}$$

The reduced form of Equation 3.1 upon combining Equations 3.6, 3.7, 3.8 can be written as

$$\frac{\partial C^*}{\partial \theta} = a_1(H,\theta) \frac{\partial^2 C^*}{\partial H^2} + a_2(H,\theta) \frac{\partial C^*}{\partial H} + a_3(H,\theta) C^* \tag{3.9}$$

where $C^*$ is the non dimensional particle concentration scaled with respect to bulk concentration $c_0$ ($C^* = c/c_0$), $H$ is the scaled separation distance. $a_1(H,\theta),\ a_2(H,\theta),\ a_3(H,\theta)$ are the coefficients which are formulated by rearranging the terms of Equations 3.6, 3.7, 3.8. Thus

$$a_1(H,\theta) = f_1(H) / \left[ \frac{Pe}{2} f_3(H) N_R U_\theta + f_4(H) N_R F_g^* \; sin\theta \right] \tag{3.10}$$

$$a_2(H,\theta) = \left\{ f_1(H) \left[ \frac{\partial \Phi}{\partial H} + F_g^* \; cos\theta \right] + \frac{\partial f_1(H)}{\partial H} + 2 F_1(H) N_R - \frac{Pe}{2} f_1(H) f_2(H) U_r \right\} / \left[ \frac{Pe}{2} f_3(H) N_R U_\theta + f_4(H) N_R F_g^* \; sin\theta \right] \tag{3.11}$$

$$a_3(H,\theta) = \left\{ \left[ 2 f_1(H) N_R + \frac{\partial f_1(H)}{\partial H} \right] \left[ \frac{\partial \Phi}{\partial H} + F_g^* \; cos\theta \right] + f_1(H) \frac{\partial^2 \Phi}{\partial H^2} - 2 f_4(H) N_R F_g^* \; cos\theta - \frac{Pe}{2} \left[ f_1(H) f_2(H) \frac{\partial U_r}{\partial H} + f_1(H) U_r \frac{\partial f_2(H)}{\partial H} + f_2(H) U_r \frac{\partial f_1(H)}{\partial H} + 2 f_1(H) f_2(H) N_R U_r + 2 f_3(H) N_R U_\theta \; cot\theta \right] \right\} / \left[ \frac{Pe}{2} f_3(H) N_R U_\theta + f_4(H) N_R F_g^* \; sin\theta \right] \tag{3.12}$$

The list of various dimensionless numbers required in solving Equation 3.9 is given in Table 3.1.

| Dimensionless group | Expression |
|---|---|
| Scaled surface to surface separation distance | $H = h/a_p$ |
| Scaled radial velocity of particle | $V_r = v_r/U$ |
| Scaled tangential velocity of particle | $V_\theta = v_\theta/U$ |
| Scaled radial velocity of fluid | $U_r = u_r/U$ |
| Scaled tangential velocity of fluid | $U_\theta = u_\theta/U$ |
| Particle Peclet number | $Pe = \frac{2Ua_p}{D_\infty}$ |
| Sherwood number | $Sh = \frac{a_p \mathcal{J}_r}{D_\infty c_0}$ |
| Scaled total interaction energy | $\Phi = \frac{\phi_T}{k_B T}$ |
| Particle aspect ratio | $N_R = a_p/r$ |
| Scaled gravitational force | $F_g^* = \frac{F_g \, a_p}{k_B T}$ |
| Collector to particle aspect ratio | $\gamma = a_c/a_p$ |

**Table 3.1** – Dimensionless groups and constants used in the scaled Convection-Diffusion-Migration equation

### 3.2.3 Boundary Conditions

Here we first focus on the radial direction boundary conditions, required at the collector surface, and at the cell outer edge. The first set of radial direction boundary conditions defined at the collector surface and the cell outer edge involves the classical perfect sink and the bulk Dirichlet conditions, respectively,

$$c = 0 \quad \text{at} \quad r = a_c \;\; (\partial\Omega \in \widehat{AD}) \tag{3.13}$$

$$c = c_0 \quad \text{at} \quad r = b \;\; (\partial\Omega \in \widehat{BC}) \tag{3.14}$$

where $\widehat{AD}$ and $\widehat{BC}$ denote the arc lengths $AD$ and $BC$, respectively. In practical applications, Eq. (3.13) is modified to

$$c = 0 \quad \text{at} \quad r \; = \; a_c + \delta \tag{3.15}$$

where $\delta$ is a small cut-off separation that prevents the divergence of the van der Waals interaction at contact ($h = 0$, corresponding to $r = a_c$) [Elimelech et al., 1995, Nazemifard et al., 2006, Prieve and E, 1974, Ruckenstein, 1964, Tien, 1989, Tufenkji and Elimelech, 2004]. We have used a value of 1 nm for the cut-off separation distance $\delta$ in most of the simulations [Adamczyk and van de Ven, 1981, Nazemifard et al., 2006].

Near the collector surface, the migration flux is predominant [Song and Elimelech, 1993]. Thus, an alternative boundary condition at the collector surface is the constant migration flux condition, which is expressed as

$$\frac{d(v_r c)}{dh} = 0 \quad \text{at } h \; = \; \Delta \tag{3.16}$$

where $v_r$ is the particle radial velocity and $\Delta$ is the cut-off separation distance [Song and Elimelech, 1993]. Typically $\Delta$ is taken as 0.159 nm from the collector surface [Nazemifard et al., 2006]. This constant migration flux boundary condition is physically more appropriate and does not violate any of the underlying assumptions made in defining the perfect sink condition. Also, it does not result in any discernible change in the deposition rates compared to the perfect sink condition defined by Equation 3.13. It, however, improves numerical stability when the particle migration velocity becomes extremely large resulting in steep gradients at the wall. The developed computer program has an option of implementing this boundary condition, but owing to the similarity of results with the perfect sink condition, we have mainly employed Equation 3.15 in our calculations.

It is important to note that use of Equation 3.14 as a boundary condition on the outer boundary is not valid under all conditions. The limitations of Equation 3.14 and suitable alternatives have been discussed in earlier studies

[Song and Elimelech, 1993]. This boundary condition establishes that at the outer boundary the particle concentration is the same as that in the fluid bulk. This boundary condition was originally used for predicting colloid retention on isolated spherical collectors [Levich, 1962, Spielman, 1977] and later extended to sphere-in-cell models. For an isolated sphere surrounded by an unbounded fluid medium, the outer boundary is defined far away from the surface of the collector where the particle concentration is not affected by the particle removal rate at the collector surface. Thus Equation 3.14 is unconditionally valid for an isolated sphere. However, for a sphere-in-cell geometry, the outer boundary, $b$, is defined as a function of the bed porosity. In this latter case, one cannot unconditionally apply the Dirichlet condition at the outer boundary.

The thickness of the diffusion boundary layer is dictated by the relative magnitudes of convection and diffusion in the system, which is quantified by the particle Peclet number ($\mathbf{Pe} = 2Ua_p/D_\infty$). Figure 3.2(a) depicts a scenario where the diffusion boundary layer thickness is much smaller than the thickness of the Happel boundary. Here, the particle concentration has already reached the bulk concentration well within the Happel boundary. Hence, imposing Equation 3.14 as a boundary condition on the outer boundary is valid. However, as the particle Peclet number decreases, the diffusion boundary shifts to the right and approaches the Happel boundary as depicted by Figure 3.2(b). At a limiting Peclet number, the two boundaries overlap. Below this limiting Peclet number, imposing a Dirichlet condition at the outer boundary violates the continuity of mass transport toward the collector. Thus, Equation 3.14 cannot be used unconditionally in conjunction with Happel's flow field, without ensuring the continuity of mass transfer, particularly for small Peclet numbers. Only at moderate and high Peclet numbers, where the mass transfer boundary layer thickness is smaller than the thickness of the fluid envelope, Equation 3.14 can be used legitimately as a boundary condition to the sphere-in-cell model [Ruckenstein, 1964]. It is also important to note that at low Peclet numbers, the concentration of particles leaving the lower quadrant of the cell is not equal to the bulk concentration.

A more general boundary condition can be derived by performing a mass balance across the outer cell boundary [Song and Elimelech, 1992]. The radial particle flux into the fluid envelope is balanced with the radial particle flux

inside the fluid envelope to ensure conservation.

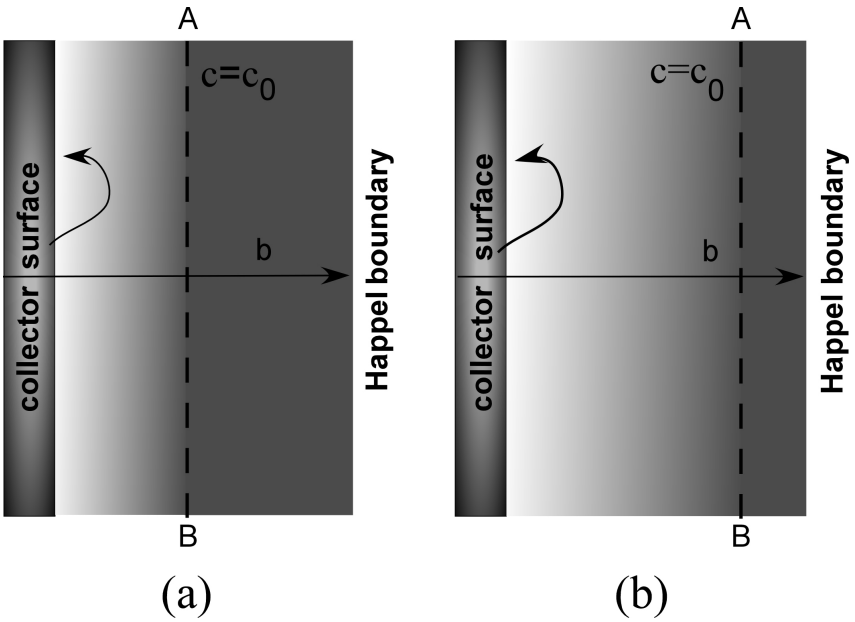


**Figure 3.2** – Relative positions of the bulk concentration limit with respect to Happel's outer boundary. The dashed line AB denotes the position in the domain where $c = c_0$, and $b$ is the outer radius of the cell. (a) Diffusion boundary layer thickness smaller than the thickness of the fluid envelope. In this case bulk concentration is reached well before Happel's boundary. (b) Diffusion boundary layer thickness approaching Happel's boundary and bulk concentration is not reached even at the outer cell radius. The color gradient in the figure also indicates the particle concentration gradient where the darker regions depict higher particle concentrations.

.

$$v_r c - D_{rr}\frac{\partial c}{\partial r} = -U c_0 \cos\theta \quad \text{at } r \;=\; b,\; 0 \leq \theta < \frac{\pi}{2} \tag{3.17}$$

$$\frac{\partial c}{\partial r} = 0 \quad \text{at } r \;=\; b,\; \frac{\pi}{2} \leq \theta \leq \pi \tag{3.18}$$

Here, $D_{rr}$ is the radial diffusion coefficient, $c_0$ is the bulk particle concentration, $v_r$ is the local radial velocity of the fluid and $\theta$ is the azimuthal angle. For

the lower half of the cell, since particles are being convected away from the collector, $c_0$ is replaced by $c$ in Equation 3.17 which gives Equation 3.18. Rewriting Equations 3.17 and 3.18 in non dimensional form,

$$\frac{2}{Pe}\frac{\partial C^*}{\partial H} = (1 - C^*)\ \cos\theta \ \text{ at } H\ =\ (b - a_c)/a_p\ ,\ 0 \leq \theta < \frac{\pi}{2} \tag{3.19}$$

$$\frac{\partial C^*}{\partial H} = 0 \ \text{ at } H\ =\ (b - a_c)/a_p\ ,\ \frac{\pi}{2} \leq \theta \leq \pi \tag{3.20}$$

At higher Peclet numbers, the left hand side of Equation 3.19 becomes negligible, which gives $C^* = 1$ as the boundary condition in the upper half of the cell. Since at high Peclet numbers, the rate of particle capture by diffusion is negligible, the concentration of the particles in the fluid leaving the cell in the lower half is also nearly equal to $c_0$ allowing use of the Dirichlet condition at the outer boundary.

Finally, for the outer cell surface, one can simply use the Neumann boundary condition

$$\frac{\partial C^*}{\partial H} = 0 \quad \text{at } H\ =\ (b - a_c)/a_p,\ 0 < \theta \leq \pi \tag{3.21}$$

with $C^* = 1$ at $\theta = 0$ and $H = (b - a_c)/a_p$. It can be easily shown that this last Neumann condition will yield similar results as Equation 3.19 for the upper hemisphere. To summarize, different combinations of boundary condition can be applied at the collector surface and the cell outer surface. These boundary conditions need to be applied judiciously depending on the parameter values, particularly the particle Peclet number.

We now consider the boundary conditions for $\theta = 0$ and $\pi$. Along the forward stagnation line ($\overline{AB}$), one can employ the symmetry condition, yielding,

$$\frac{\partial C^*}{\partial \theta} = 0 \quad \text{at} \quad \theta = 0\ \ (\partial\Omega\ \in\ \overline{AB}) \tag{3.22}$$

However, the numerical technique used in the present model does not require this boundary condition, as will be explained later. Finally, noting that Equation 3.9 is parabolic in $\theta$, there is no need to specify the boundary condition at $\theta = 180^o$.

### 3.2.4 Particle Deposition Rate

Once the particle concentration distribution is numerically determined, the non-dimensional flux of particles at the collector surface can be evaluated by

$$J^*(H_{min},\theta) = -\frac{2f_1(H_{min})}{Pe}\frac{\partial C^*}{\partial H} + f_1(H_{min})f_2(H_{min})U_r C^* - \frac{2f_1(H_{min})}{Pe}\left[\frac{\partial \Phi}{\partial H} + F_g^*\ cos\theta\right] C^* \tag{3.23}$$

where $H_{min} = \delta/a_p$ and $J^* = J_r/(Uc_0)$, with $J_r$ being the normal flux to the wall.

The overall deposition rate for the unit cell is calculated by integrating Equation 3.23 over the collector surface, yielding

$$I = 2\pi(a_c + \delta)^2(Uc_0)\int_0^\pi J^*(H_{min},\theta)\sin\theta\ d\theta \tag{3.24}$$

The overall particle deposition efficiency can be directly calculated from Equation 3.24 as [Elimelech et al., 1995]

$$\eta = \frac{I}{\pi a_c^2 U c_0} \tag{3.25}$$

One can define the Sherwood number as $Sh = a_p J_r/(D_\infty c_0)$. A non dimensional average Sherwood Number, $Sh_{avg}(= 1/S\int_S Sh(\theta)d\theta$, where $S$ is the total collector surface area), which quantifies the overall deposition on the ideal collector is related to the single collector efficiency as

$$Sh_{avg} = \frac{\eta Pe}{4} \tag{3.26}$$

Equations 3.25, 3.26 provide the overall particle retention characteristics for flow through the porous media. The overall modeling scheme is summarized in Figure 3.3.

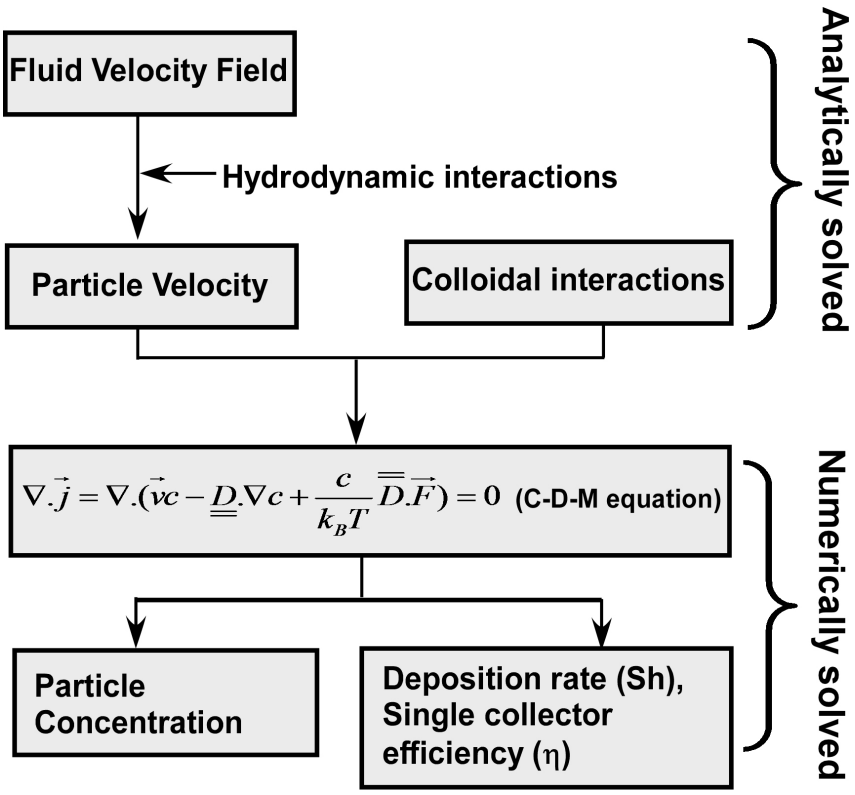


**Figure 3.3** – Overall modeling scheme employed in evaluating particle deposition rate.

## 3.3 Numerical Technique and Solution Methodology

Numerical solution of the convection-diffusion-migration (C-D-M) equation with the prescribed boundary condition as discussed in the previous section was obtained using the method of lines [Zwillinger, 1998] employing a code

implemented in FORTRAN77. Equation 3.9 was discretized in the radial direction using a central difference scheme with the terms in the coefficients also expressed using finite difference formulae. The finite differencing in the radial direction resulted in a set of coupled ordinary differential equations for $\partial C^*/\partial\theta$, which were simulaneously solved using a Differential Algebraic Equation (DAE) solver DASSL [dda]. The solver DASSL is an open source code that can be found in the SLATEC library from Netlib's repository (www.netlib.org).

DASSL is a numerical solver which solves an implicit system of differential algebraic equations (DAE) of the form $F(y, y\prime, t) = 0$. The algorithm approximates the derivative using a $k^{th}$ order backward differencing formula (BDF) and then solves the resulting system of equations using iterative Newton's method. DASSL selects the current time step $\Delta t$ and the value of $k$ (which can be any number between 1 and 5) according to the nature and stiffness of the solution making it adaptive by nature. The algorithm estimates the values of the local error at a constant step size and current order $k$. It then checks what the error would have been at orders $k-1$, $k-2$ and $k+1$. Depending upon the estimate comparison and the predefined tolerance values set by the user, the order and step size for the next iteration are selected. DASSL also requires the user to supply the initial value of the dependent variable and its derivative and the algorithm works most efficiently when the initial guess is accurate.

The computational domain was discretized using Chevyshev's meshing scheme in the radial coordinate with a gradually increasing density of mesh points near the collector surface. This is to ensure a stable and non-oscillating solution since particle concentration gradients are significantly large near the collector surface due to short range colloidal interactions [Kemps and Bhattacharjee, 2009, Nazemifard et al., 2006, Song and Elimelech, 1993]. A smaller sub-domain depicted in Figure 3.1(a) as the area enclosed between the collector surface and the dotted line (area $APQC$) is used to further refine the mesh with a high density of grid points to accurately capture the sharp changes in concentration gradients. The radial distance of the arc PQ from the collector surface was fixed at 50nm for all simulations since the colloidal interactions are the dominant in this range. The thinner sub-domain was discretized into 5000 Chevyshev's mesh points with increasing mesh density near the collector

surface. The outer sub-domain was discretized with 7000 Chevyshev's mesh points also with gradually increasing mesh density near the boundary $\widehat{PQ}$. Thus the entire domain consisted of 12000 mesh points divided between two sub domains. The above discretization scheme also ensured that sudden jump in mesh density was not encountered at the interface of the two sub domains. In the tangential coordinate, the computational domain was discretized into 360 mesh points with a gradually increasing mesh density near the forward stagnation line. This ensured a speed up of the solution process. However, since the ODE solver uses adaptive stepping based on a predefined tolerance, the initial discretization in the $\theta$ direction does not influence the solution accuracy.

The solution of the ODEs marches in the tangential coordinate starting from the forward stagnation line ($\overline{AB}$) where an initial guess solution is provided. All mesh points along the forward stagnation line is initialized with a non dimensional concentration of 1 (i.e, $C^* = 1$) except at the collector surface where the non dimensional concentration is initialized to 0 (i.e, $C^* = 0$). The rationale for choosing such a guess solution was the fact that at the forward stagnation line, the concentration boundary layer is very thin and bulk concentration is reached at a very short distance from the collector wall. This technique saves computational cost in solving the forward stagnation line concentration as a separate Boundary Value Problem (BVP) by employing the third boundary condition (Equation 3.22). The solution method described here would significantly reduce memory consumption and accelerate the solution time.

## 3.4 Validation of the Computational Model

To test the accuracy of the numerical solution, the model results were compared against analytical results available in literature for limiting cases of the convection-diffusion-migration equation. Table 3.2 summarizes the values of the parameters used in the numerical solution.

In the absence of colloidal interactions, gravity, and hydrodynamic retardation, Equation 3.1 reduces to the classical convective diffusion equation. Levich [Levich, 1962] provided the analytical solution to the problem. The average

**Table 3.2** – Physical properties of the system used in the numerical simulations

| Parameter | Value |
|---|---|
| collector radius, $a_c$ | 164 $\mu$m |
| particle radius, $a_p$ | 5nm - 2$\mu$m |
| particle density, $\rho_p$ | 1077 kg/m$^3$ |
| particle density, $\rho_f$ | 997 kg/m$^3$ |
| temperature, $T$ | 298 K |
| Boltzmann constant, $k_B$ | $1.38 \times 10^{-23}$ $J/K$ |
| fluid freestream velocity, $U$ | $3.44 \times 10^{-4}$ m/s |
| Hamaker constant, $A_H$ | $1 \times 10^{-21} - 5 \times 10^{-20}$ J |

Sherwood number for a spherical collector, as given by the Levich-Lighthill equation, takes the form

$$Sh_{avg} = 0.624 Pe_c^{1/3} \tag{3.27}$$

where $Pe_c$ is the Peclet number defined with respect to the collector and expressed as

$$Pe_c = A_S \frac{2a_c U}{D_\infty} = A_s Pe\gamma \tag{3.28}$$

It is emphasized here that $Pe_c$ has been used only to evaluate the analytical average Sherwood number in this study. For all numerical simulations presented in this work, particle Peclet number ($Pe = \frac{2Ua_p}{D_\infty}$), as previously defined, has been used consistently.

In Equation 3.28, $A_s$ is the porosity dependent parameter for the sphere-in-cell geometry [Elimelech et al., 1995], $a_c$ is the collector radius, $U$ is the fluid free stream velocity, and $D_\infty$ is the bulk diffusion coefficient and $\gamma$ is the particle to collector aspect ratio ($\gamma = a_c/a_p$). These dimensionless numbers are described in detail in Table 3.1. Our numerical model can replicate Levich's assumptions by setting $F_g = F_{vdW} = 0$ and $f_1 = f_2 = f_3 = f_4 = 1$.

Figure 3.4 compares the results from the numerical model with Levich's analytical solution. Excellent agreement between the two solutions is observed for particle Peclet numbers of 100. At larger values of Peclet number, the solution starts deviating from Levich's solution because as particle size increases beyond a certain value, Levich's assumption of treating the particle as a point is violated and interception effects come to the fore. For this simulation, particle Peclet number was changed by changing the particle size. The numerical model captures this effect due to the finite size of the particle [Ruckenstein, 1964]. The comparison demonstrates the ability of the numerical model to accurately predict the fundamental mass transport behavior over a spherical collector in a packed bed.

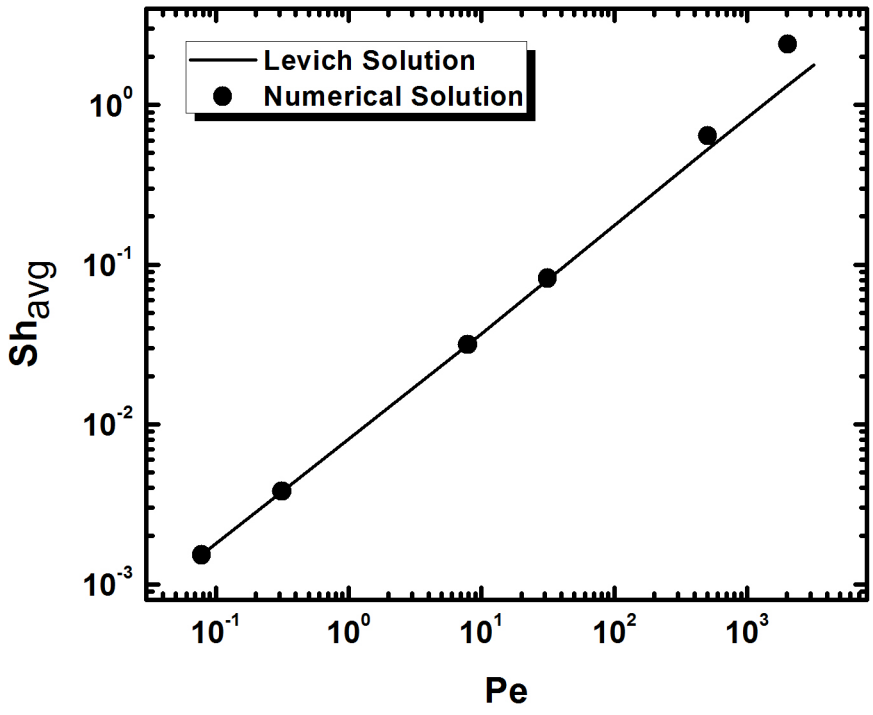


**Figure 3.4** – Variation of Average Sherwood number with Peclet number for a spherical collector using Happel cell model. The solid line denotes the value of the average Sherwood number calculated by the Levich equation (Equation 3.27) whereas the closed circles denote our numerical solution of the convection-diffusion-migration equation with Levich's assumptions.

## 3.5 Particle Transport Behavior-Results and Discussion

In this section, we present the numerical results of the local particle deposition rates, as well as the single collector efficiencies by considering the coupled influence of attractive van der Waals interaction and gravity on the particle transport near a spherical collector. Unless otherwise stated, all our simulations were performed employing the perfect sink condition on the collector and the bulk concentration boundary condition at the outer cell surface.

### 3.5.1 Diffusion Dominated Deposition: Levich Solution

One of the limiting cases of particle deposition is diffusion dominated deposition in the absence of hydrodynamic, gravitational, and colloidal interactions [Levich, 1962]. This limiting behavior (as $a_p \rightarrow 0$) should be displayed by any particle transport and deposition model irrespective of whether the van der Waals attraction, hydrodynamic retardation, and gravitational forces are considered in the model or not. Figure 3.5 compares the numerical results from the present study to Levich's solution under different parametric conditions. Figure 3.5(a) depicts the influence of different Hamaker constants on the average Sherwood number in presence of hydrodynamic retardation whereas Figure 3.5(b) represents the influence of hydrodynamic retardation in absence of van der Waals interaction on the average Sherwood number. The expression for the van der Waal's interaction is based on Derjaguin approximation in absence of electrodynamic retardation (*cf.* Equation 2.13). In all simulations, the other parameters are as given in Table 3.2. It is evident that under all combinations of hydrodynamic retardation and van der Waals interactions commonly encountered in deposition systems, and for negligible gravity, it is virtually impossible to observe a significant deviation from the Levich solution for particle Peclet numbers less than 100. The deviations above this Peclet number are mainly due to interception. As expected, hydrodynamic interactions will lower the Sherwood number from the Levich result in absence of van der Waals attraction.

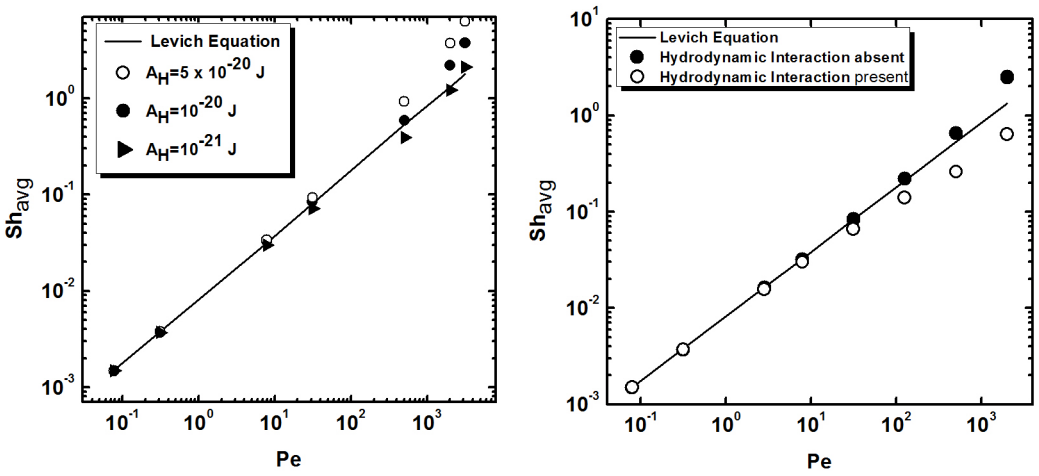


**Figure 3.5** – Variation of average Sherwood number with particle Peclet number. (a) Effect of Hamaker constant on average Sherwood number with hydrodynamic interactions present. (b) Effect of hydrodynamic retardation on average Sherwood number with colloidal interactions absent. The solid line represents the Levich solution. The parameters used in the numerical simulations have been enumerated in Table 3.2. Effect of gravity has been neglected in all the above results.

.

In Figure 3.6, variations of the convective and diffusive flux terms with particle size at a surface to surface separation distance of 1 nm is shown in the presence (solid lines) and absence (dashed lines) of hydrodynamic interactions. It is clear that for particle radii smaller than 100 nm, inclusion of the hydrodynamic retardation functions have no measurable influence on the particle convection or the diffusion. It is interesting to note that although the diffusion coefficient is significantly reduced owing to hydrodynamic retardation, the overall diffusive flux remains relatively unaltered as the concentration gradient adjusts itself to account for the reduced diffusivity in presence of hydrodynamic interactions.

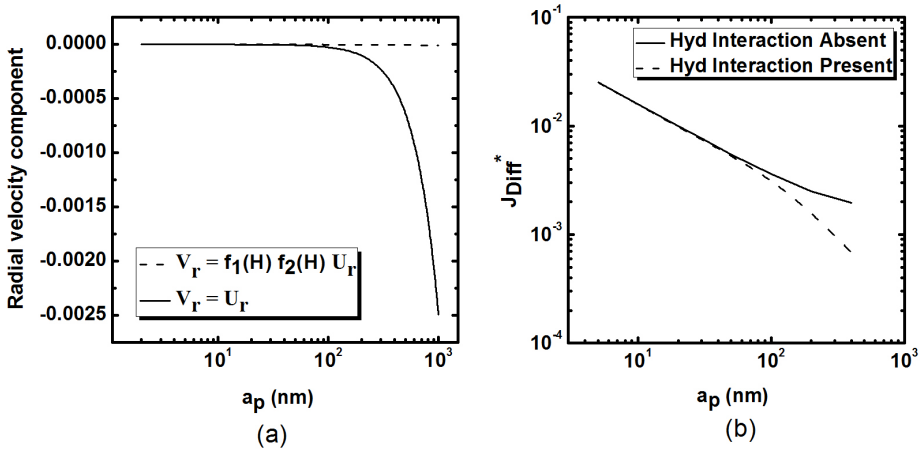


**Figure 3.6** – Effect of hydrodynamic correction factors on dimensionless particle velocity and dimensionless particle diffusive flux. The local values of the dimensionless particle velocities and dimensionless diffusive particle flux have been calculated at an azimuthal angle of $\theta$ =45$^o$. (a) The solid line represents the non dimensional particle velocity ($V_r$) without the hydrodynamic corrections incorporated while the dashed line represents the non dimensional particle velocity with the hydrodynamic corrections incorporated. (b) The solid line depicts the dimensionless diffusive particle flux near the collector in the absence of hydrodynamic interactions while the dashed line represents the flux when hydrodynamic interactions are accounted for. The parameters used to perform the simulations are listed in Table 3.2.

These observations clearly re-establish that the Levich assumption of point-like particles is attained for particles smaller than about 100 nm. For the given set of parameters in Table 3.2, the numerical results tend to deviate from the analytical solution only as the particle radius exceeds 100 nm. Even then, the attractive van der Waals and the hydrodynamic retardation seem to counteract each other, leaving the Sherwood number relatively close to the Levich result.

### 3.5.2 Significance of Happel's Boundary for the Sphere-In-Cell model

As discussed previously, the Happel sphere-in-cell model is an approximation for granular media where the outer cell radius, $b$, is defined as a function of the medium porosity [Elimelech et al., 1995, Happel, 1958, Payatakes et al., 1974, Ruckenstein, 1964]. This outer boundary is not a true physical boundary. In the original definition by Happel, the outer boundary was treated as a free surface such that there is no tangential stress component on it [Happel, 1958]. Under these circumstances, there could be a profound influence of the choice of outer cell surface boundary condition on the solution of the convection diffusion migration equation, particularly as the diffusion boundary layer thickness tends to extend to the Happel cell thickness. This behavior is depicted in Figure 3.7, which shows the influence of the Dirichlet and Neumann boundary conditions on the dimensionless concentration profiles. For moderately high Peclet numbers, such as in Figures 3.7(a) and 3.7(b), the concentration profiles with the Dirichlet and Neumann boundary conditions at the outer cell surface are quite similar. The only difference is the unphysical step discontinuity at the outer cell surface for larger azimuthal angles $\theta \geq 170^{o}$ observed with the Dirichlet boundary condition. With Neumann condition at the outer cell surface, the discontinuity is avoided.

At low Peclet numbers (or strongly diffusive systems), the concentration maps with the two boundary conditions give very different results as shown in Figures 3.7(c) and 3.7(d). Figure 3.7(d), which incorporates the Neumann condition derived in Equations 3.19 and 3.20, clearly indicates the continuous decrease in the concentration at the outer cell surface with increasing azimuthal angle. In contrast, use of Dirichlet condition in Figure 3.7(c) at the outer boundary for such low Peclet numbers grossly misrepresents the particle transport behavior, artificially altering the mass transfer to the collector surface. The choice of the above Peclet numbers for depicting the difference in the concentration profiles are only representative. With this background it is possible to define a threshold Peclet number (for a given thickness of the fluid envelope which is a function of the porosity of the medium) beyond which the Dirichlet boundary condition cannot be legitimately used.

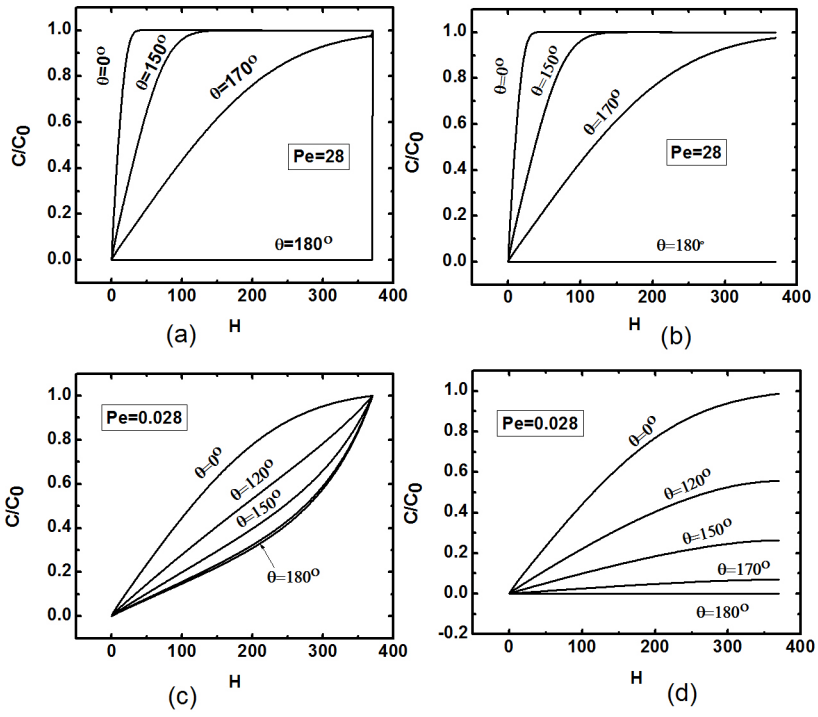


**Figure 3.7** – Variation of concentration with radial distance from the collector at different azimuthal angles. (a) Simulation results with Dirichlet boundary conditions. (b) Simulation results with Neumann boundary conditions. The parameters used in these simulation are $a_p = 25\ nm$, $U = 5 \times 10^{-3} m/s$, $f = 0.4$ and $a_c = 0.05\ mm$.(c) Simulation results with Dirichlet boundary conditions.(d) Simulation results with Neumann boundary conditions. The parameters used in these simulation are $a_p = 25\ nm$, $U = 5 \times 10^{-6} m/s$, $f = 0.4$ and $a_c = 0.05\ mm$.

.

Figure 3.8 shows the regions in the Peclet number-porosity space where use of Dirichlet boundary condition is valid. The region demarcated as $\delta_{Diff} < \delta_{Happel}$ gives the values of porosity and Peclet number where the diffusion boundary layer is well within the Happel's boundary as depicted earlier by the schematic in Figure 3.2 the outer boundary. Thus, the grey region in Figure 3.8 denotes the porosity-Peclet number phase space in which $\delta_{Diff} \not< \delta_{Happel}$. Using any single collector efficiency correlation beyond the acceptable Peclet number-porosity phase space (i.e., where $\delta_{Diff} < \delta_{Happel}$) could lead to erroneous predictions of the deposition rate. This error has a greater chance of manifesting itself only in case of the sphere-in-cell geometry as its outer hy-

drodynamic boundary is artificially imposed and depends on porosity. This ambiguity is not present in other regular collector geometries, such as stagnation point flow, parallel plate channel, or an isolated spherical collector.

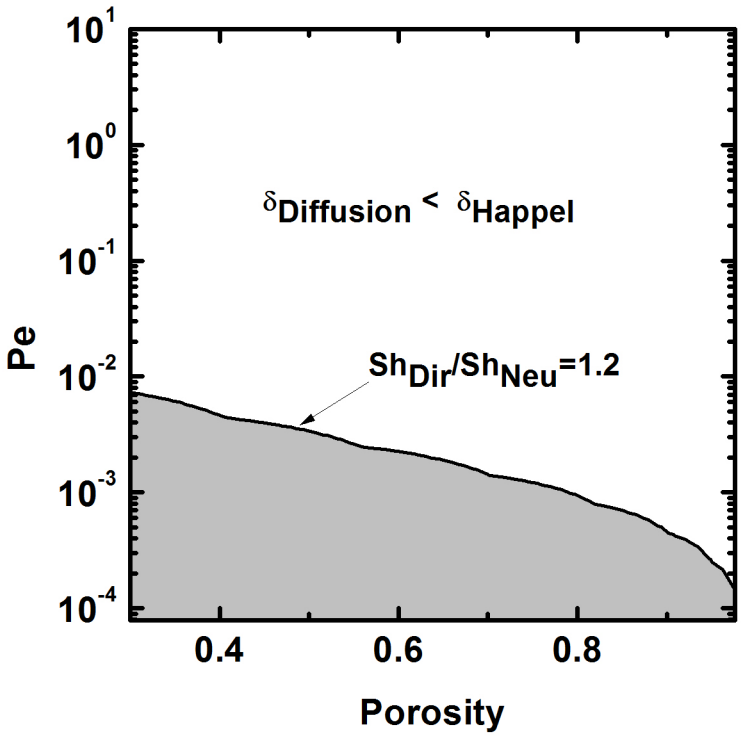


**Figure 3.8** – Regions in Peclet and Porosity domain showing thickness of the diffusion boundary layer relative to the thickness of the Happel's boundary. $Sh_{Dir}$ and $Sh_{Neu}$ are the average Sherwood number values calculated by using Dirchlet and Neumann boundary conditions respectively at $r = b$. The two regions are separated by an iso line such that $Sh_{Dir}/Sh_{Neu} = 1.2$ on all points on the line. For a given porosity, the corresponding values of Peclet number on this iso line define the limit beyond which the Dirichlet condition cannot be used at the outer boundary.

### 3.5.3 Effect of Gravity on Particle Deposition

The influence of gravity on deposition is represented through the non dimensional Gravity number

$$Gr = \frac{4\pi a_p^4(\rho_p - \rho_f)g}{3k_BT} \tag{3.29}$$

where $a_p$ is the particle radius, $\rho_p$ and $\rho_f$ are the particle and fluid densities respectively, $k_B$ is the Boltzmann constant, and $T$ is the temperature. Depending on the density of the particle relative to the fluid, gravity either assists or opposes the deposition process. Also, depending upon the sign of the gravity number, gravity aids deposition in one quadrant of the collector and opposes it in the other quadrant. Influence of gravity on deposition has been extensively studied in context of many standard collector geometries, most notably by Prieve and Ruckenstein for isolated spherical collectors [Prieve and E, 1974]; however, a detailed analysis of the influence of gravity on the Sherwood number in a sphere-in-cell geometry is still lacking.

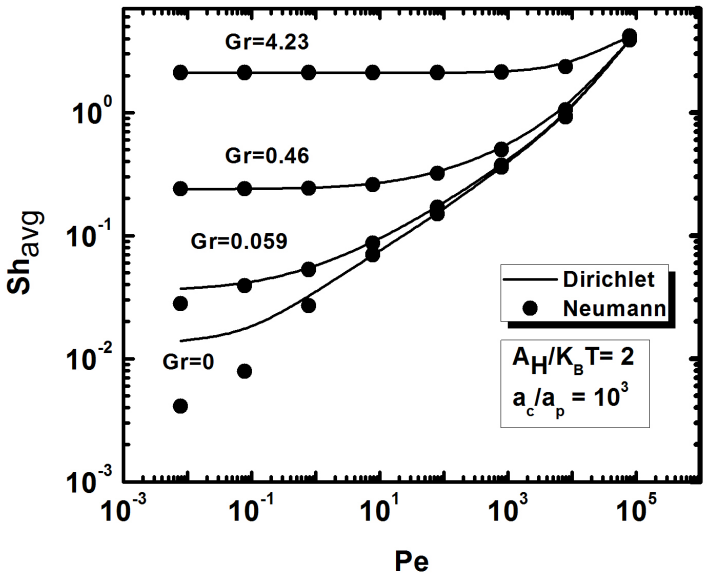


**Figure 3.9** – Variation of Sherwood number with Peclet number under different gravitational intensities. The solid lines represent the results from the numerical solution using a Dirichlet condition at the outer boundary whereas the closed circles represent the corresponding results from the numerical solution with a Neumann condition at the outer boundary. The Peclet number for this simulation was varied by changing the flow velocity. Similar low values of Peclet number can otherwise also be obtained by employing particles of less than 1 nm size which would be unrealistic.

Figure 3.9 depicts the effect of the gravitational intensity on the particle

deposition rate at different Peclet numbers obtained for the sphere-in-cell geometry. The solid lines show predictions using the Dirichlet condition at the outer boundary, whereas the symbols are based on the Neumann condition. At higher values of $Gr$, the deposition rate becomes almost constant at lower Peclet numbers. This indicates that for larger $Gr$, gravity masks the effect of convection and diffusion. At very high Peclet numbers, convection dominates, and the Sherwood number becomes independent of $Gr$. At lower values of $Gr$ and $Pe$, there is significant difference between the deposition rates when Neumann and Dirichlet conditions are used at the outer boundary. For high $Gr$ values, even at low Peclet numbers, this disagreement is not observed. This is because the transport is dominated by migration, which confines the diffusion boundary layer to well within the Happel cell thickness. Such a difference is not observed in case of an isolated collector [Prieve and E, 1974]. As previously mentioned, one of the contributions of the present analysis is to highlight the difference in particle deposition behavior of an isolated sphere and a packed bed of spheres in presence of gravity, which has not been previously studied.

### 3.5.4 Single Collector Efficiency

The dependence of particle deposition efficiency on particle size has been a subject of interest in several studies over the past four decades [Kemps and Bhattacharjee, 2009, Nazemifard et al., 2006, Nelson and Ginn, 2005, Rajagopalan and Tien, 1976, Tufenkji and Elimelech, 2004, Yao et al., 1971]. As stated in the introduction, the correlations of Rajagopalan and Tien [Rajagopalan and Tien, 1976] and Tufenkji and Elimelech [Tufenkji and Elimelech, 2004] differ in the diffusion dominated region, with the Tufenkji and Elimelech correlation showing a different slope compared to the Levich slope.

Figure 3.10 compares the numerically computed single collector efficiency values from our Eulerian model with the two correlations. All the plots are characterized by a minimum single collector efficiency at a particular value of particle radius, which will henceforth be referred to as $(a_p)_{min}$. For particle radii smaller than $(a_p)_{min}$, deposition is diffusion dominated, whereas for particle radii greater than $(a_p)_{min}$, deposition is dominated by interception, gravity, and migration forces.

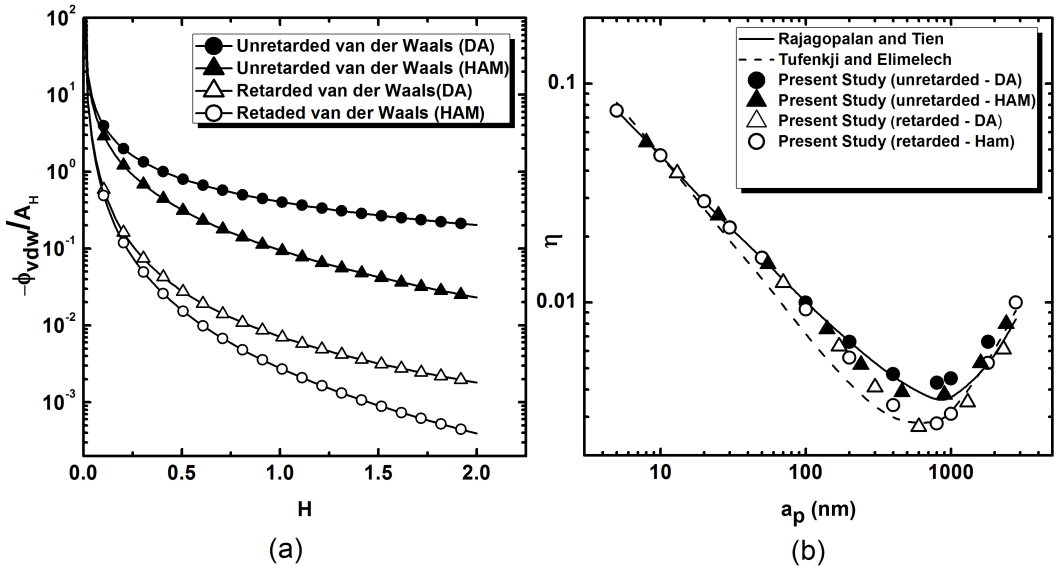


**Figure 3.10** – (a) Variation of van der Waals interaction energies with scaled separation distance. The curves represent four different van der Waals interaction energy definitions as follows - solid line: unretarded, Derjaguin approximation; open circles: unretarded, Hamaker approach; dashed line: retarded, Derjaguin approximation (Schenkel and Kitchener [**?**]); dotted line: retarded, Hamaker approach (Czarnecki [**?**]).The expressions for these interaction energies are provided in the supporting information. $-\phi_{vdW}/A_H$ denotes the absolute scaled energy calculated by these expressions. (b) Single collector efficiency variation with particle size. The solid and dashed lines represent the Rajagopalan-Tien and Tufenkji-Elimelech correlation, respectively. The symbols represent the numerically calculated values with different van der Waals expressions.The parameters used for these simulations are: $a_c = 1.64 \times 10^{-4} m$, $U = 3.44 \times 10^{-4} m/s$, $A_H = 1 \times 10^{-20} J$, $\Delta\rho = 0$, $T = 298K$, $f = 0.37$

.

The numerical results obtained from our Eulerian model (symbols) all coincide with the RT correlation for particle sizes below 100 nm (the Levich limit). For 100 nm $< a_p <$ 2000 nm, the numerical results show two distinct trends depending on whether the unretarded (solid symbols) or the retarded (open symbols) van der Waals interactions are employed. The expressions considering

the retarded van der Waals interactions coincide with the Tufenkji-Elimelech correlation near $(a_p)_{min}$. Indeed, Tufenkji and Elimelech used the Hamaker expression for the retarded van der Waals interaction in their work, and hence, it is not a surprise that our Eulerian model gives their result. However, Rajagopalan and Tien also used the retarded van der Waals interaction in their trajectory analysis. Why does their correlation predict higher values of $\eta$ in this regime of particle size? This is because it is derived by linear superposition of the Levich equation to their deterministic trajectory analysis solution in the interception/migration regime. This approximation could be avoided in more rigorous Lagrangian particle tracking models that account for Brownian motion. Indeed, use of the Hamaker expression for retarded van der Waals interaction in the particle tracking model [Kemps and Bhattacharjee, 2009] yields results that match the corresponding result of our Eulerian model.

The simulation results show that near the deposition minimum, the Tufenkji-Elimelech correlation should be more accurate. However, if a correlation is developed based on linear regression from a data set that has more bias (larger number of points) from near the deposition minimum, the exponents of such correlations could be unrealistic. We note here that Tufenkji and Elimelech obtained their correlation for the diffusion based single collector efficiency, $\eta_D$, as

$$\eta_D \propto Pe^{-0.715} \tag{3.30}$$

employing linear regression of their numerical results over the entire range of particle radius of 0.01 to 10 $\mu$m. However, our simulation results clearly show two distinct regimes in the diffusion dominated range, with $\eta_D \propto Pe^{-0.67}$ for $a_p < 100$ nm, followed by a different exponent for approximately 100 nm $< a_p < (a_p)_{min}$. As Figure 3.10 suggests, the disagreement in the slope of the single collector efficiency curve from the Tufenkji-Elimelech correlation is quite significant below $(a_p)_{min}$ when compared to the RT correlation (or the Levich slope). This calls for the development of an improved correlation which accurately estimates the deposition efficiency below the $(a_p)_{min}$ range. It is also important to note that the efficiency values would differ depending upon the expressions used for the van der Waals interactions. This aspect has been pre-

viously overlooked in the existing body of literature related to single collector efficiency evaluation.

To summarize, the Levich solution represents the correct limiting behaviour of colloidal systems as particle sizes become smaller. This behavior is ubiquitous in all classical deposition systems and hence, it should also be exhibited in sphere-in-cell systems.

As discussed previously, caution must be exercised in choosing the boundary condition at the outer boundary for low particle Peclet numbers. Figure 3.11 shows the difference in the single collector efficiency *vs.* Peclet number plots when Neumann and Dirichlet boundary conditions are used at low Peclet numbers. As the classical correlations are not based on the Neumann boundary condition, but instead on the Dirichlet condition, they will predict unphysically high values of the single collector efficiency ($\eta > 1$) in the limit $Pe \rightarrow 0$. This unphysical behavior can be avoided by employing the Neumann condition at the outer mass transfer boundary, which will limit the value of the single collector efficiency to 1 as $Pe \rightarrow 0$. In light of this, proper bounds must be defined when employing the correlations to ensure their accuracy. For the range of parameters considered in development of Rajagopalan-Tien, as well as Tufenkji-Elimelech correlations, assumption of Dirichlet boundary condition at the outer cell surface is valid. However, one should not extrapolate these conditions to cases where the diffusion boundary layer thickness merges with the Happel boundary, and then claim these correlations to be unphysical - these correlations simply should not be used under such low Peclet numbers.In light of this, the present study proposes the threshold Peclet number and the Peclet-porosity space in which the Dirichlet condition can be used legitimately. The analysis also explains the shortcomings of the two most widely used correlations pertinent to particle deposition in saturated porous media and explains the grounds on which the two differ. The findings from the study opens up the scope for the development of a more accurate correlation to predict the single collector efficiency, particularly for Brownian particles.

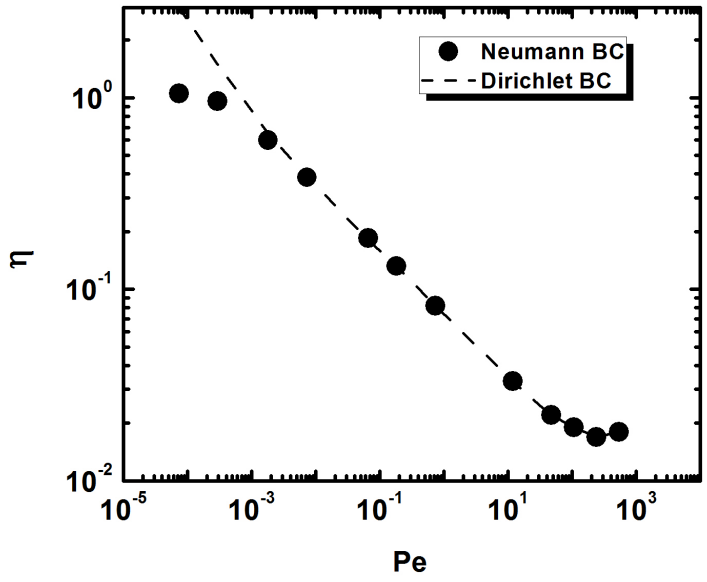


**Figure 3.11** – Comparison of efficiency plots using Dirichlet and Neumann boundary conditions on the outer boundary. Parameters used for this simulation are the same as that in Figure 3.7. However, the efficiency here has been defined with respect to the fluid cell instead the collector.

## 3.6 New Correlation for Predicting Single Collector Efficiency in Sphere-in-cell Models

Different correlations for predicting single collector efficiency have evolved over the years as discussed in the previous section. However, it was only in 2004 that Tufenkji and Elimelech [2004] performed studies to capture the effect of colloidal and hydrodynamic interactions on single collector efficiency for particles of all sizes. They performed linear regression analysis on the numerical data generated by their Eulerian model and proposed an analytical correlation to establish a relationship between the single collector efficiency and the relevant non-dimensional parameters involved [Tufenkji and Elimelech, 2004]. Prior to the Tufenkji and Elimelech (TE) correlation, the Rajagopalan and Tien (RT) correlation [Rajagopalan and Tien, 1976] remained the most widely used correlation for predicting single collector efficiency. In essence, the TE correlation is an improvement on the RT correlation for Brownian particles by incorporating the effects of colloidal and hydrodynamic interactions. Although other correlations have also been developed since then [Long and Hilpert, 2009, Ma

and Johnson, 2010], the RT and TE correlations remain the most widely used and will be our focus in this thesis for comparison.

Classical correlations predict a minimum single collector efficiency at a particle size around 1$\mu$m (*cf.* Figure 3.10), which we refer to here as $(a_p)_{min}$, where $a_p$ is the particle radius. The difference in the RT and TE correlation is essentially in predicting the deposition efficiency for Brownian particles ($a_p \leq 1\mu m$). However, both correlations fall short of predicting theoretically correct results for the entire range of particle sizes below $(a_p)_{min}$. The RT correlation does not consider colloidal interactions (namely van der Waals interactions) and hydrodynamic retardation for particles smaller than $(a_p)_{min}$ and uses the analytical Levich equation to characterize the deposition behavior in this regime [Rajagopalan and Tien, 1976]. Tufenkji and Elimelech [Tufenkji and Elimelech, 2004] corrected this by accounting for the effects of the van der Waals and hydrodynamic interaction for particles smaller than $(a_p)_{min}$ but their correlation violates the fundamental limiting behavior given by the Levich's equation [Levich, 1962]. Levich's equation, like in all other geometries, represents the true limiting behavior of mass transfer as particles approach point-like dimensions even for the Happel sphere-in-cell model [Kemps and Bhattacharjee, 2009, Nazemifard et al., 2006]. The present work proposes a new correlation which overcomes these limitations of the RT and TE correlations by incorporating correction factors in a theoretically consistent manner.

### 3.6.1 Development of the Correlations

Figure 3.12 compares the the numerically obtained values for the single collector efficiency with the RT and TE correlations for a representative set of parameters (Table 3.2). It appears from Figure 3.12 that the numerical results tend to follow the RT line approximately up to a particle radius of 100 nm. Beyond this, the efficiency values tend to dip below the RT line progressively to finally meet the TE line around the $(a_p)_{min}$ of *ca.* 1$\mu$m. The efficiency values predicted by both correlations and the numerical model for particle sizes greater than $(a_p)_{min}$ are in good agreement with each other upto the 2$\mu$m size we studied in this letter. Thus, three distinct regions can be demarcated on the efficiency curve. We call these the *Brownian deposition regime* for $\eta$ corresponding to $a_p < 100\ nm$, the *transition deposition regime* for $\eta$ corresponding

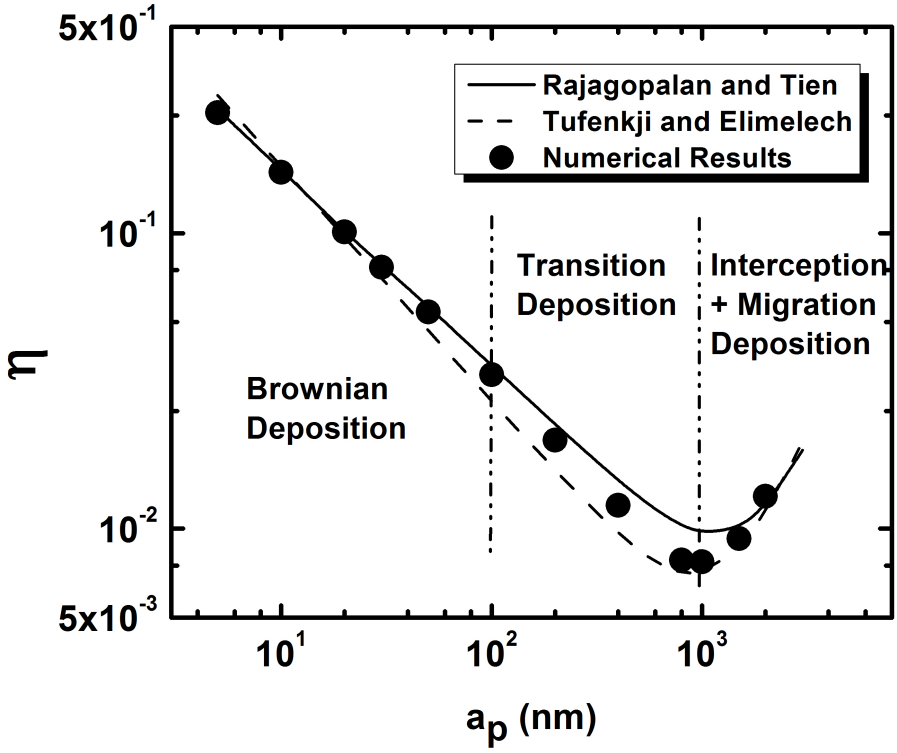


**Figure 3.12** – Comparison of single collector efficiency curves for the RT correlation, TE correlation and results from the numerical analysis. The parameters used for this simulation are $a_c = 0.2\ mm$, $f = 0.4$, $A_H = 1.0 \times 10^{-20}$ J, $U = 4.0 \times 10^{-5}$ m/s, $T = 298$ K, $\rho_f = 997$ Kg/$m^3$ and $\rho_p = 1050$ Kg/$m^3$

to 100 $nm < a_p < (a_p)_{min}$ and the *interception and migration dominated deposition regime* for $a_p > (a_p)_{min}$. These regions have been indicated in Figure 3.12 as well.

Consistent with the earlier discussions, Figure 3.12 suggests that the RT correlation, containing the Levich equation [Levich, 1962], is correct for *Brownian deposition* but must be corrected for the *transition deposition* regime to accurately predict deposition below $(a_p)_{min}$. It is important to note that the slope of the efficiency curve is different in the *Brownian* and *transition* regions. As a matter of fact, the slope of the curve in the *transition* region is greater than $Pe_c^{-0.715}$. In this context, the slope of the TE correlation below $(a_p)_{min}$ only represents an average slope of the deposition curve in the Brownian and transition regions and thus misinterprets the correct deposition in the *Brownian* and *transition* regime.

The deviation of the efficiency values from the Levich equation in the *transition* regime can been attributed to the retardation in the van der Waal's expression [Kemps and Bhattacharjee, 2009, Tufenkji and Elimelech, 2004]. Further, it has been shown that when un-retarded van der Waal's interaction energy is used in evaluating the efficiencies, this deviation is not observed and numerical results agree perfectly with the RT correlation below $(a_p)_{min}$ (cf. Figure 3.10). This suggests that the retardation in the van der Waals expression is the significant factor in determining the slope of the efficiency curve in the *transition* region.

Based on the above discussions, we define our new correlation which is given as

$$\eta = \underbrace{4.04 A_s^{1/3} Pe_c^{-0.667} \eta_{ret}}_{\eta_D} + \underbrace{0.55 A_s \gamma^{1.675} N_A^{0.125}}_{\eta_I} + \underbrace{0.22 \gamma^{-0.24} N_{grav}^{1.11} N_{vdW}^{0.053}}_{\eta_G} \quad (3.31)$$

where $\eta_{ret}$ is the proposed correction factor to accommodate for the dip in the efficiency values beyond the *Brownian* regime and is of the form

$$\eta_{ret} = (1 + a_p/\zeta)^{-\chi} \quad (3.32)$$

Here, $\zeta$ and $\chi$ are values which are to be determined by non-linear regression analysis of the numerical results. Careful observation indicates that $\eta_{ret}$ shares the same form as that of the retardation term in van der Waals energy expression as per Dejaguin approximation. The remaining non-dimensional numbers used in Equation 3.31 have been summarized in Table 2.4. Since the TE correlation does not require any correction in the *interception and migration* regime, the new correlation retains the $\eta_I$ and $\eta_G$ terms from the TE correlation [Tufenkji and Elimelech, 2004] in Equation 3.31.

### 3.6.2 Non-Linear Regression Methodology

A robust non-linear regression analysis subroutine LMDIF from the FORTRAN library MINPACK (www.netlib.org/minpack) was used to obtain the values of $\zeta$ and $\chi$ in Equation 3.32. LMDIF uses a modified Levenberg-Marquardt algorithm and optimizes the values of the unknown parameters by minimizing the sum of squares of the residuals. Thus, for a set of $m$ independent-dependent variable pair $(x_i, y_i)$, the algorithm optimizes the value of the fitting parameter $\beta$ of the hypothetical curve $f(x, \beta)$ such that the sum of the square of the difference

$$G(\beta) = \sum_{i=1}^{m} [y_i - f(x_i, \beta)]^2 \tag{3.33}$$

is minimum. In this a user defined subroutine calculates the function $G(\beta)$ for an initial guess solution to be provided by the user. The algorithm then automatically performs multiple iterations for evaluating the optimized value for $\beta$.

For the problem in question, the $f(x, \beta)$ function is given by Equation 3.31 and the data set $(x_i, y_i)$ is obtained from the numerical C-D-M model described in the previous section. It is important to note that unlike all previous studies which have used linear regression analysis to derive the correlation for predicting single collector efficiency, the present work employs non-linear regression analysis. This enables the model to capture the different slopes of the *Brownian* and *transition* regimes accurately by performing a non-linear fit rather than fitting a straight line with an average slope for the entire size range of particles below $(a_p)_{min}$.

## 3.7 The New Correlation for Predicting Single Collector Efficiency

The expression for $\eta_{ret}$ obtained from the non-linear regression analysis is given as

$$\eta_{ret} = \left(1 + \frac{a_p}{2.0 \times 10^{-7}}\right)^{-0.243} \tag{3.34}$$

and thus the overall correlation takes shape as

$$\begin{aligned}\eta &= \underbrace{4.04 A_s^{1/3} Pe_c^{-0.667} \left(1 + \frac{a_p}{2.0 \times 10^{-7}}\right)^{-0.243}}_{\eta_D} + \underbrace{0.55 A_s \gamma^{1.675} N_A^{0.125}}_{\eta_I} \\ &+ \underbrace{0.22 \gamma^{-0.24} N_{grav}^{1.11} N_{vdW}^{0.053}}_{\eta_G} \end{aligned} \tag{3.35}$$

Figure 3.13 compares the new correlation with the RT and TE correlations as well as the numerically calculated values of the single collector efficiency. It is clear that the new correlation matches the theoretically calculated efficiency values much more accurately compared to the RT and TE curves. The most significant improvement, however, lies in the fact that the developed correlation obeys the limiting Levich solution for Brownian particles and captures the deposition behavior in the *transition* regime correctly where the colloidal and hydrodynamic interactions start taking effect. In essence, it corrects the slope of the TE correlation in the diffusion regime which violates the Levich equation and improves on the RT correlation for particles roughly larger than 100 nm in radius by accounting for the colloidal and hydrodynamic interactions. The parameters used for the simulations in Figure 3.13 depict the conditions that are most widely encountered practical filtration scenarios.

Comparing the $\eta_D$ term of the new correlation with the $\eta_D$ term of the TE correlation, it is easy to see that unlike in the latter, the former does not have a $N_{vdW}$ term. For particles smaller than 100 nm in radius this would not have any effect whatsoever as already established [Kemps and Bhattacharjee, 2009]. Near $(a_p)_{min}$, the correlation slightly over-predicts the deposition efficiency values for strongly convective conditions with low attraction intensity as suggested by Figure 3.13(d) . But even then the deviation between the numerical values and that predicted by the correlation is less than 10 percent. Thus, the correction term in $\eta_D$ of the new correlation accommodates for these variations quite accurately. It is also interesting to note that the exponent of the $N_{vdW}$ term in the TE correlation is a small number (0.052) which indicates

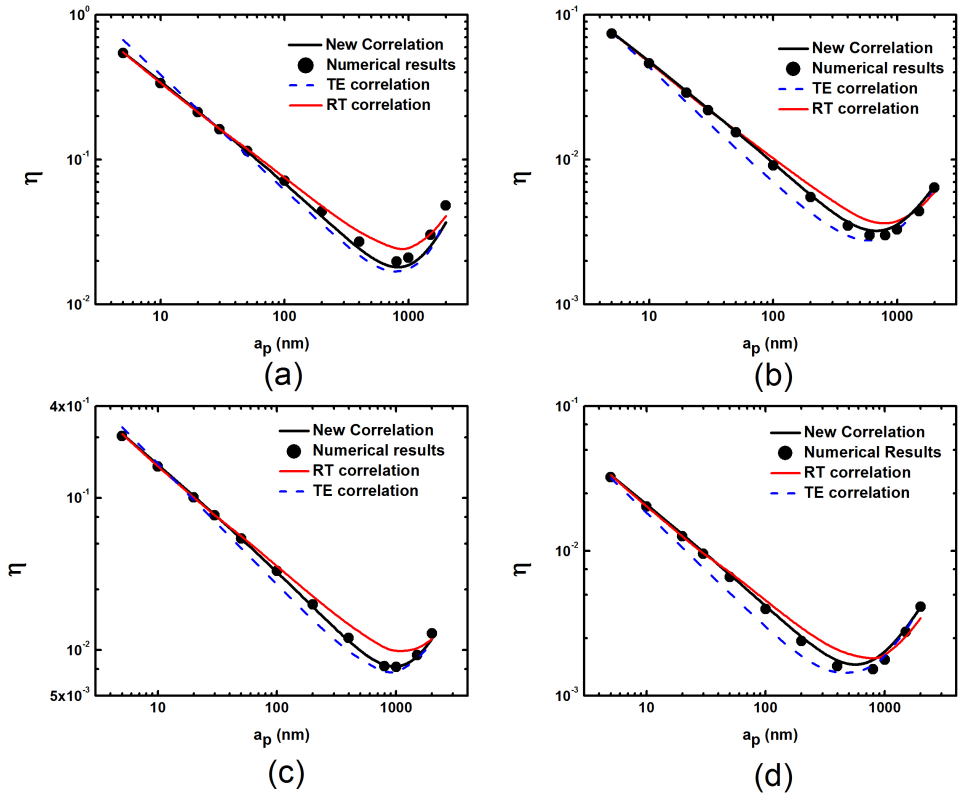


**Figure 3.13** – Comparison of the new correlation with RT and TE correlations. For all 4 simulations shown in this figure $\rho_p = 1.05\ g/cm^3$, $\rho_f = 0.997\ g/cm^3$, $A_H = 10^{-20}\ J$. (a) $a_c = 1.64 \times 10^{-4}\ m$, $U = 3.44 \times 10^{-4}\ m/s$, $f = 0.37$, $T = 298\ K$ (b) $a_c = 0.3 \times 10^{-3}\ m$, $U = 9.0 \times 10^{-6}\ m/s$, $f = 0.39$, $T = 298\ K$ (c) $a_c = 0.2 \times 10^{-3}\ m$, $U = 4.0 \times 10^{-5}\ m/s$, $f = 0.4$, $T = 298\ K$ (d) $a_c = 0.2 \times 10^{-3}\ m$, $U = 1.0 \times 10^{-3}\ m/s$, $f = 0.36$, $T = 288\ K$

that the effect of this parameter on the diffusion dominated deposition is not significant. Also, as elaborated in the previous section, the deviation from the Levich equation in the *transition* regime stems from the retardation in the van der Waals interaction energy and not the attraction. If retardation is not accounted for in the van der Waals energy, the numerical results are in perfect agreement with the RT correlation [Kemps and Bhattacharjee, 2009].

Figure 3.14 establishes the accuracy of the new correlation statistically and compares it with that of the TE correlation. It is important to note that the primary focus of the present work is to propose a theoretically correct correla-

tion. Comparison with experimental results to establish its accuracy could be misleading as the experimental data would form a random scatter around the dashed line in Figure 3.14. It is clear that the newly developed correlation is almost an ideal fit (with a slope of 0.98) and is far more accurate compared to the TE correlation (slope of 0.84). The TE correlation seems to over-predict the higher efficiency values which would typically be in the *Brownian* regime. Since the TE correlation violates the Levich equation in the *Brownian* regime, it is important to investigate the nature of this correlation separately for point like particles. The RT correlation has not been used for comparison in Figure 3.14 since it does not consider the effects of the colloidal and hydrodynamic interactions below $(a_p)_{min}$ and statistical comparison with the RT correlation could be misleading.

It has already been pointed out that the major shortcoming of the TE correlation lies in the fact that it violates the limiting mass transport behavior given by Levich equation for Brownian particles. Figure 3.15 compares the Levich equation with the TE correlation and the newly developed correlation for 3 different cases. The parameters listed in Table 3.2 were used for this simulation but for particles upto 100 nm in radius where the Levich equation must be obeyed. In a recent review article by Petosa *et al.*[Petosa et al., 2010] it has been mentioned that the TE correlation over-predicts the efficiency values for particles below 30nm in diameter. This is true only for strongly diffusive systems as indicated by Figure 3.15(a) where the open circles fall below the dashed line. As the intensity of convection is increased, the results from the TE correlation starts to under-predict and fall below the Levich equation for the entire range of particle sizes as indicated by 3.15(b) and (c). This is purely a mathematical manifestation of the average $Pe_c^{-0.715}$ slope which renders the correlation physically untenable in the *Brownian* regime. Compared to this, the new correlation, depicted by the filled circles, obeys the limiting Levich behavior accurately and falls perfectly on the dashed line for all conditions.

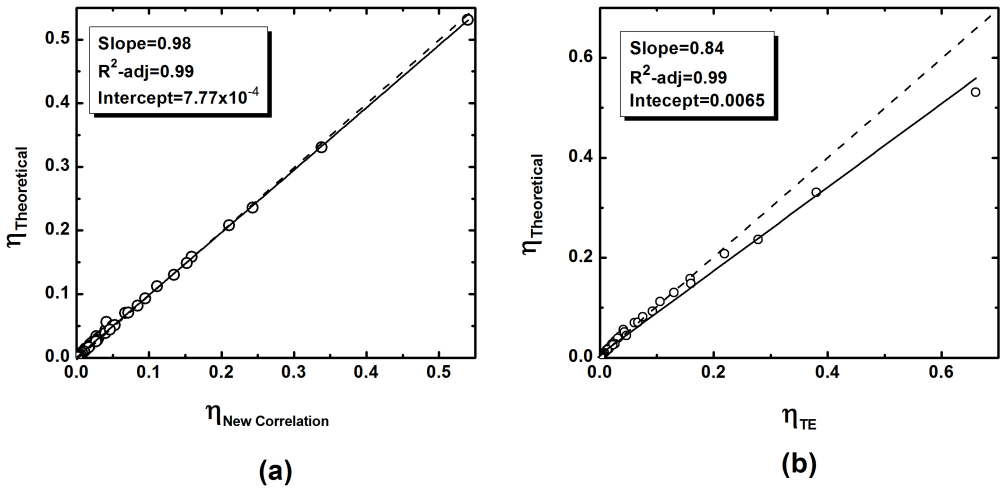


**Figure 3.14** – Statistical comparison of the correlation and numerical results. (a) Single collector efficiency values from the new correlation compared with the numerically generated results. (b) Single collector efficiency values from the TE correlation compared with the numerically generated results. The numerical results are obtained over the entire parameter space in Table 3.2. For an ideal linear fit, the dashed and solid lines should coincide.

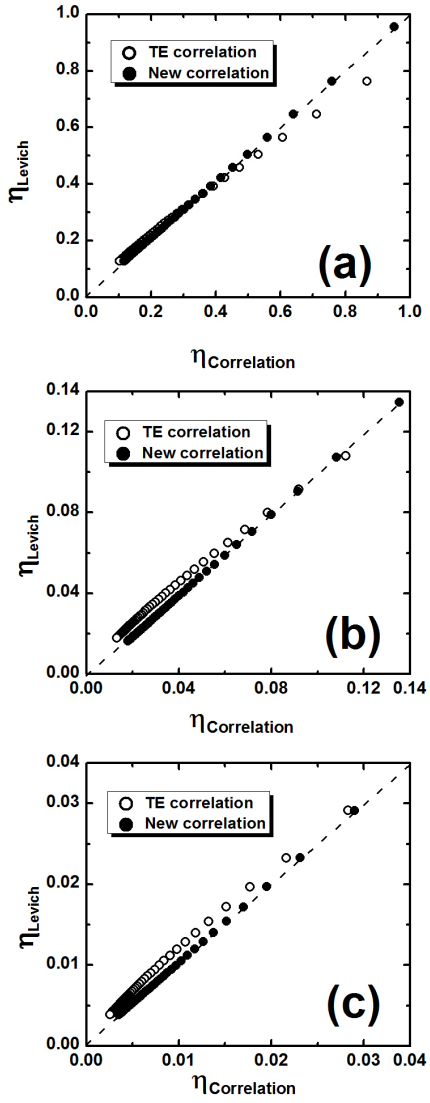


**Figure 3.15** – Comparison of TE and the new correlation results with the Levich Solution for 3 cases. (a) Strongly diffusive (or weakly convective) system: $a_c = 0.3\ mm$, $A_H = 1 \times 10^{-20}\ J$, $U = 8.0 \times 10^{-6}\ m/s$, $\rho_p = 1050\ Kg/m^3$, $\rho_f = 997\ Kg/m^3$, $f = 0.37$ (b) Mildly diffusive (or mildly convective) system: $a_c = 0.3\ mm$, $A_H = 1 \times 10^{-20}\ J$, $U = 8.0 \times 10^{-5}\ m/s$, $\rho_p = 1050\ Kg/m^3$, $\rho_f = 997\ Kg/m^3$, $f = 0.37$ (c) Weakly diffusive (or strongly convective) system: $a_c = 0.3\ mm$, $A_H = 1 \times 10^{-20}\ J$, $U = 8.0 \times 10^{-4}\ m/s$, $\rho_p = 1050\ Kg/m^3$, $\rho_f = 997\ Kg/m^3$, $f = 0.37$. For all three cases 5 nm$< a_p <$100nm which defines the *Brownian* regime.

## 3.8 Summary

In this chapter, systematic evaluation of particle deposition models in literature to calculate single collector efficiency is performed and their disagreements with one another is addressed. Discussions from this chapter indicate that the Eulerian approach for predicting Sherwood number and the single collector efficiency for the Happel sphere-in-cell geometry provides the same results as the Lagrangian approach when all governing transport mechanisms are considered simultaneously. The study re-establishes that Levich's solution cannot be violated for point like particles and the deviation of the TE correlation from the Levich slope for Brownian particles($a_p < 100\ nm$) is not physical. Further, a new correlation with the correct particle deposition behavior for the entire range of particle sizes and other parameters was presented. This new correlation represents an improvement on the established correlations for single collector efficiency prediction. Having evaluated and established the correct mass transport on homogeneous collectors, in the next chapter, we look at more realistic cases of particle deposition onto spherical collectors with surface heterogeneity. The same Eulerian model will be retained but unlike in the present chapter, EDL interactions will be incorporated and their role in particle deposition will be analyzed.

# Chapter 4

# Particle Deposition onto Patchy and Janus Spherical Collectors-Effect of Surface Chemical Heterogeneity on Deposition [1]

## 4.1 Introduction

In the previous chapter, particle deposition onto a smooth homogeneous spherical collector in the absence of electrostatic double layer interactions were presented. However, in most cases physical heterogeneity in the form of roughness and chemical heterogeneity in the form of surface charge is inevitable. Real heterogeneity is however, random and too complex to facilitate systematic analysis. Further, including both types of heterogeneity in the same model makes it rather difficult to evaluate the effect of each on particle deposition. To the best of the author's knowledge, there is no existing model that incorporates both physical and chemical heterogeneity together. In this chapter, we present a numerical model to evaluate the effect of surface chemical heterogeneity on particle deposition in a sphere-in-cell geometry using DLVO interactions (EDL+vdW). In order to enable tractable analysis, the surface chemical heterogeneity is modeled using the commonly employed patterning technique [Nazemifard et al., 2006, Rizwan and Bhattacharjee, 2009]. Two particular types of surface patterning are discussed thereby giving the collector

[1] Parts of this chapter have been published in *Langmuir*, June 2011, doi:10.1021/la201421n., *In press*

Janus and patchy characteristics. The choice of these two types of collectors are in line with the recent verve in developing methods to fabricate particles (which can be used as collectors) with such surface properties. The other important aspect of this model is that it considers chemical heterogeneity on spherical collector surfaces. To the best of the author's knowledge most other works dealing with chemical heterogeneity have focused only on planar surfaces. Towards the end of the chapter, we discuss novel applications of using such collectors as efficient collectors in filter beds.

## 4.2 Modification of Cell Model to Predict Deposition on Heterogeneous Surfaces

A schematic representation of sphere-in-cell geometry with micropatterned surface charge distribution is indicated in Figure 4.1(a). The collector consists of concentric circular bands with alternate positive and negative surface potentials. The figure depicts flow at a tilt angle $\chi$ to the vertical. The section denoted by $\widehat{ABC}$ constitutes *Half I* of the geometry and the remaining part of the collector constitutes *Half II*. When the tilt angle $\chi$ is 0 and $\pi$, the entire transport process is symmetric about the line $AC$ and the deposition in the two halves are identical. For all other values of $\chi$, the deposition is different in the two halves due to the combined effect of gravity and the fluid flow field. It is important to note that the flow symmetry about $AC$ is not broken. This symmetry is retained to keep the analysis tractable while keeping the essential physics of heterogeneity intact. $F_g$ and $F_{int}$ denote the force due to gravity and colloidal interactions (van der Waals and Electrostatic Double Layer interactions) respectively. The 0 and $\pi$ shown in the figure indicates the start and end points of the $\theta$ discretization for numerical evaluation. Figure 4.1(b) shows the angular pitch ($p$) given as the total angular width of the positive ($w_p$) and negative ($w_n$) stripes, all angles measured in radians. Each band is separated by the horizontal dashed lines.

A qualitative picture of the particle trajectory as it is transported around the collector is shown in Figure 4.1(b). The repulsion over the positive band makes the particle to move away from the collector followed by an attractive stretch which causes it to migrate towards the collector. All other features of the original Happel cell model [Elimelech et al., 1995, Happel, 1958] are maintained in the present analysis. For a positively charged particle, the ratio

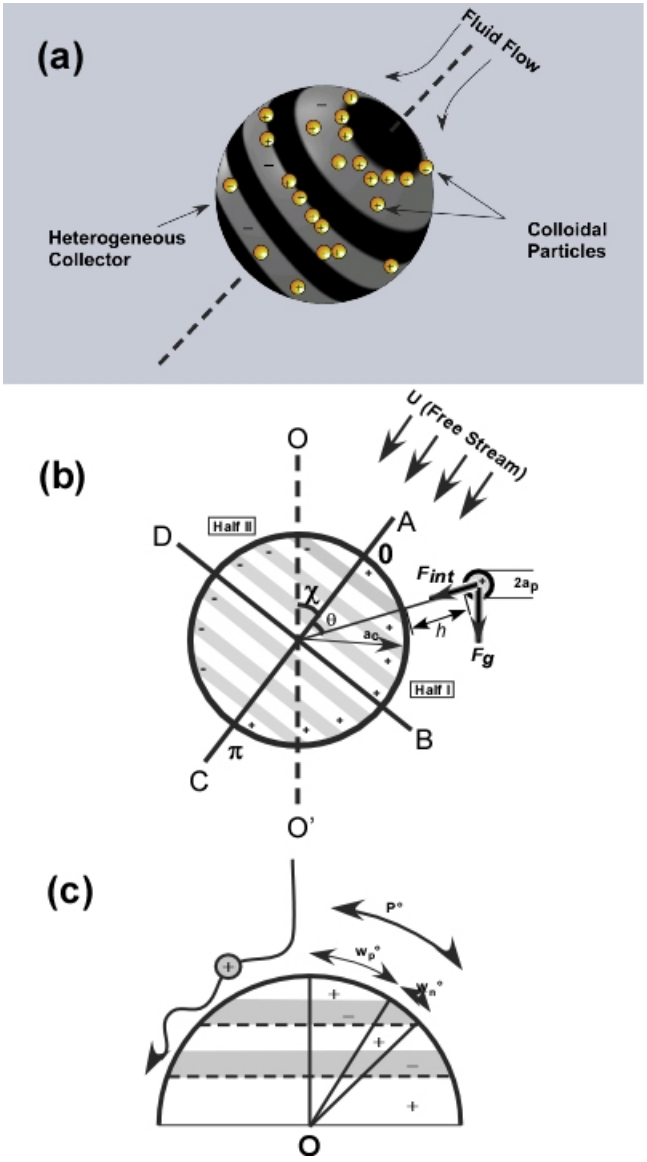


**Figure 4.1** – (a) Schematic representation of a collector with micropatterned surface charge distribution showing preferential particle accumulation. (b) The collector consists of concentric circular bands with alternate positive and negative surface potentials. The figure depicts flow at a tilt angle $\chi$ to the vertical. The section denoted by $\widehat{ABC}$ constitutes *Half I* of the geometry and the remaining part of the collector constitutes *Half II*. $F_g$ and $F_{int}$ denote the force due to gravity and colloidal interactions (van der Waals and Electrostatic Double Layer interactions) respectively. (c) Collector showing the positive ($w_p$) and negative ($w_n$) stripes and the angular pitch ($p$)(all in radians). $h$ is the dimensional surface-to-surface separation distance.

of the negative stripe thickness ($w_n$) to the angular pitch quantifies the fraction of the collector surface that attracts the particle and favors deposition. The favorable area fraction is denoted as $\lambda_p = A_f/A$ where $A_f$ is the area of collector favoring deposition and $A$ is the total surface area of the collector. Thus

$$\lambda_p = \frac{A_f}{A} = \frac{\sum_{n=1}^{n=N_b} \int_{(n-1)p+w_p}^{np} 2\pi a_c^2 sin(\theta) d\theta}{4\pi a_c^2} \tag{4.1}$$

where $n$ is the index and $n \in (1, N_b)$, $p$ is the angular pitch, $N_b$ is the total number of bands on the collector surface. If $N_b$ is sufficiently large, then Equation 4.1 can be approximated fairly accurately as

$$\lambda_p = \frac{A_f}{A} \simeq \frac{w_n}{p} \tag{4.2}$$

In the present study, the particle is positively charged and the first stripe of each band is always positively charged and unfavorable to deposition as indicated in Figure 4.1. The charge heterogeneity is incorporated by varying the scaled surface potential ($\Psi_s$) over the white and shaded regions giving it a periodic profile along $\theta$. Thus, $\Psi_{s,n}$ and $\Psi_{s,p}$, denote the negative and positive scaled surface potentials. Although the profile indicates discontinuity at the edges of the stripes, the accuracy of such a profile in calculating the EDL energies has been established earlier [Nazemifard et al., 2006]. Thus, the periodic variation of $\Psi_s$, represents a simplified model to simulate surface charge heterogeneity effects on the double layer interaction energies. In this model, it is assumed that the EDL energies are governed entirely by the surface potentials of the particle and the collector region directly facing it (distance of closest approach). Such approximation has been shown to be sufficiently realistic as long as $\kappa a_p > 5$ [Nazemifard et al., 2006]. Solution of the Poisson-Boltzman equation over the heterogenous surface provides a more robust evaluation of the EDL energies for lower values of $\kappa a_p$ [Das and Bhattacharjee, 2005].

### 4.2.1 Modified Governing Equations

Although the fundamental governing equations for the particle transport (Equations 3.1, 3.2, 3.3) do not change, subtle modifications must be made to incorporate the EDL interactions and the effect of the tilt angle $\chi$. For the geometry depicted in Figure 4.1(a), net radial force includes the radial component of the gravitational force ($F_g$), the attractive van der Waals force ($F_{vdW}$) and the electrostatic double layer interactions ($F_{EDL}$) between the particle and the collector:

$$F_r = -\frac{d\phi_T}{dr} - \frac{4}{3}\pi a_p^3(\rho_p - \rho_f)g \ \cos(\chi + \theta) \tag{4.3}$$

where $\phi_T$ ($= \phi_{Ham} + \phi_{EDL}$) is the total interaction energy due to attractive van der Waals interaction and electrostatic double layer interactions. The present model uses retarded van der Waals interaction energy evaluated using the Hamaker's approach (Equation 2.16) [**?**]. The electrostatic double layer interaction is calculated using the well established Hogg, Healy and Fuerstenau (HHF) [Hogg et al., 1966] expression under the assumptions that linearized Poisson-Boltzmann equation is applicable, surface potentials are constant and the electrolyte in question is a symmetric (z:z) electrolyte. The interaction energy is expressed as

$$\phi_{h,EDL} = 4\pi\epsilon\epsilon_0 a_p \left(\frac{k_B T}{ze}\right)^2 \Psi_p \Psi_s \left[\ln(1 + e^{-\kappa h}) - \frac{(\Psi_p - \Psi_s)^2}{4\Psi_p \Psi_s} \ln(1 - e^{-2\kappa h})\right] \tag{4.4}$$

Here, $\epsilon$ and $\epsilon_0$ are the dielectric constant and permittivity of vacuum, $\Psi_p$ and $\Psi_s$ are the scaled particle and surface potentials, $\kappa$ is the inverse Debye length, $z$ is the valency and $e$ is the electronic charge. It is easy to observe that for equipotential surfaces, $\Psi_p,\ \Psi_s$, the last term in Equation 4.4 becomes zero. The expression used for the Double Layer interaction energy in Equation 4.4 applies to sphere-flat plate interactions. For small particle to collector aspect ratio systems ($a_p/a_c < 0.1$), this expression is sufficiently accurate, especially near the wall of the collector where these colloidal interactions are predomi-

nant.

The coefficients $a_1(H,\theta)$, $a_2(H,\theta)$ and $a_3(H,\theta)$ in the explicit form of the C-D-M equation in Equation 3.9 are modified for the geometry in question. Thus

$$a_1(H,\theta) = f_1(H) / \left[ \frac{Pe}{2} f_3(H) N_R U_\theta + f_4(H) N_R F_g^* \ sin(\chi+\theta) \right] \tag{4.5}$$

$$\begin{aligned} a_2(H,\theta) = \Bigg\{ & f_1(H) \left[ \frac{\partial \Phi}{\partial H} + F_g^* \ cos(\chi+\theta) \right] + \frac{\partial f_1(H)}{\partial H} + 2F_1(H) N_R \\ & - \frac{Pe}{2} f_1(H) f_2(H) U_r \Bigg\} / \left[ \frac{Pe}{2} f_3(H) N_R U_\theta + \right. \\ & \left. f_4(H) N_R F_g^* \ sin(\chi+\theta) \right] \end{aligned} \tag{4.6}$$

$$\begin{aligned} a_3(H,\theta) = & \left\{ \left[ 2f_1(H) N_R + \frac{\partial f_1(H)}{\partial H} \right] \left[ \frac{\partial \Phi}{\partial H} + F_g^* \ cos(\chi+\theta) \right] + f_1(H) \frac{\partial^2 \Phi}{\partial H^2} - \right. \\ & f_4(H) N_R F_g^* \ sin(\chi+\theta) / tan\theta - f_4(H) N_R F_g^* \ cos(\chi+\theta) - \\ & \frac{Pe}{2} \left[ f_1(H) f_2(H) \frac{\partial U_r}{\partial H} + f_1(H) U_r \frac{\partial f_2(H)}{\partial H} + f_2(H) U_r \frac{\partial f_1(H)}{\partial H} \right. \\ & \left. + 2f_1(H) f_2(H) N_R U_r + 2f_3(H) N_R U_\theta \ cot\theta \right] \Big\} / \\ & \left[ \frac{Pe}{2} f_3(H) N_R U_\theta + f_4(H) N_R F_g^* \ sin(\chi+\theta) \right] \end{aligned} \tag{4.7}$$

The list of relevant non-dimensional parameters used for solving Equation 3.9 remain the same as provided in Table 3.1. The boundary conditions used for solving the C-D-M equation are identical to the ones used for solving the standard sphere in cell model.[Elimelech, 1994, Elimelech et al., 1995, Masliyah and Bhattacharjee, 2006, Ruckenstein, 1964, Tufenkji and Elimelech, 2004]

Once the particle concentration distribution is numerically determined, the non-dimensional flux of particles at the collector surface can be evaluated by

$$\begin{aligned} J^*(H_{min},\theta) = & -\frac{2f_1(H_{min})}{Pe} \frac{\partial C^*}{\partial H} + f_1(H_{min}) f_2(H_{min}) U_r C^* - \\ & \frac{2f_1(H_{min})}{Pe} \left[ \frac{\partial \Phi}{\partial H} + F_g^* \ cos(\chi+\theta) \right] C^* \end{aligned} \tag{4.8}$$

where $H_{min} = \delta/a_p$ and $J^* = J_r/(Uc_0)$, with $J_r$ being the normal flux to the wall. $\delta = 1\ nm$ is the wall cut off separation to prevent non-physical divergence of van der Waals interaction at contact. The expressions for calculating the overall deposition efficiency ($\eta$) and the overall deposition rate ($Sh$) are given in the previous chapter (Equations 3.24, 3.25, 3.26). The numerical technique used to solve the governing set of equations is the same as described in the previous chapter (Section 3.3)

## 4.3 Particle Deposition onto Janus Collectors

In this section, deposition behavior on Janus collectors is discussed. The spherical collector is assumed to be attractive in the upper half and repulsive in the lower half as shown by the unit cell inset in Figure 4.2. As stated in the previous section, the orientation of the line demarcating the two halves on the collector must be perpendicular to the flow direction to maintain azimuthal symmetry. The overall deposition behavior for such a collector is compared against that of a homogeneously favorable collector which is used as a benchmark.

Two possible cases can be used to describe the surface heterogeneity of a Janus collector. The first one, which we shall refer hereafter as Configuration1, has an attractive lower half (shown by the shaded region in Figure 4.2(a)) which favors deposition and a repulsive lower half which hiders deposition. The other scenario, referred to as Configuration2, favors deposition in the shaded upper half and hinders deposition in the lower half. Such differential surface characteristics are typical to Janus particles [Chute et al., 2011, Liang et al., 2011]. In order to determine the deposition behavior, it is important to first investigate the concentration distribution of the particles near the collector surface.

For Configuration 1, the concentration profile shows a sharp peak at the leading edge of the shaded favorable half where the surface potential flips from being positive to negative (or in other words repulsive to attractive) for a positively charged particle. Such a sharp rise in concentration indicates an accumulation of particles near the edge. This happens because in the leading half of the collector, the particles are not able to penetrate the repulsive energy

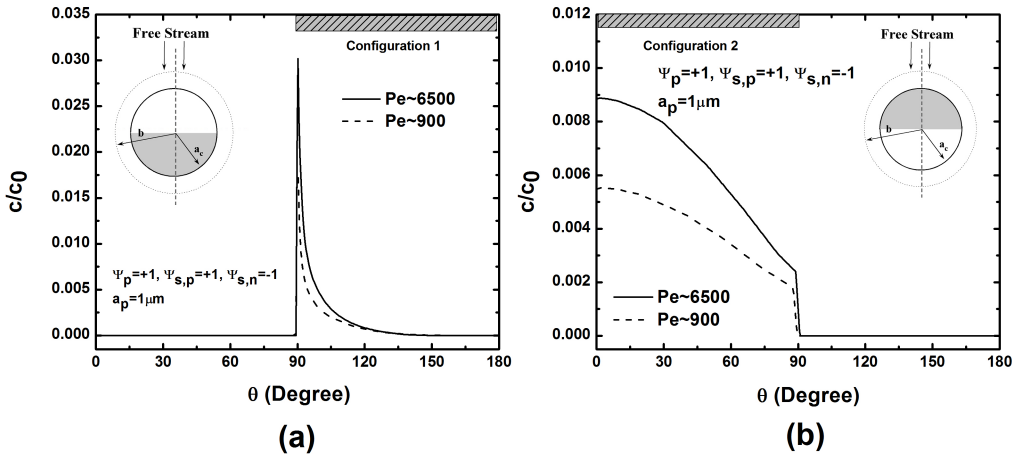


**Figure 4.2** – Scaled concentration of particles around the collector near the wall (at a separation distance of ∼5 nm). The shaded regions indicate the attractive halves. Thus for Configuration 1, the lower half ($90° \leq \theta \leq 180°$) is shaded and for Configuration 2, the upper half ($0° \leq \theta \leq 90°$) is shaded. The dashed lines correspond to the concentration distribution for a lower Peclet number ($Pe \simeq 900$) while the solid lines represent a higher Peclet number ($Pe \simeq 6500$). Sub-parts (a) and (b) correspond to Configuration1 and Configuration2 respectively.

barrier due to double layer interactions and are convected around the collector due to the fluid flow. Upon reaching the edge where there is a sudden change in surface potentials, the particles quickly migrate towards the wall due to the attractive colloidal interactions. The peak is sharper as the intensity of convection is increased, as more particles are being transported to the edge at a faster rate resulting in greater accumulation. The concentration profile shows a decaying behavior after the peak, which indicates that the probability of finding a particle decreases along $\theta$ as most particles have already deposited at the edge. The decay is less steeper with greater convection as there is a greater chance of a particle to be carried along with the flow past the leading edge of the attractive region.

For Configuration 2, the upper half being attractive, the particles deposit as it would for a homogeneously attractive collector until it reaches the trailing edge of the attractive region. The particle concentration is highest near the stagnation point due to the combined action of the impinging action of the flow and the attractive colloidal interactions. As the particles are transported around the collector in the tangential direction, the intensity of the shear flow increases and radial flow decreases, carrying the particle further along the $\theta$ direction indicated by a steady drop in the concentration till the trailing edge. At the trailing edge, there is an abrupt drop in concentration due to the sudden change in surface potentials thereby making the interactions repulsive in nature. Beyond this, no deposition occurs due to the repulsion. Thus a marked difference in the transport behavior around the two collector configurations is observed. Understandably, the overall deposition rate around each of these collectors would be different.

Figure 4.3 depicts the variation in deposition efficiencies with Peclet number for a homogeneously attractive collector and a half attractive-half repulsive Janus collector with the two possible configurations described earlier. The deposition efficiencies show a decreasing trend upon increasing convection due to the relatively higher tangential particle flux compared to the radial particle flux. The dependence of the deposition rate on Peclet number is much stronger for Configuration 2 compared to that of Configuration 1. This is expected due to the convection of particles away from the collector in the lower half. Upon comparison of the deposition efficiencies of the two configurations with that of

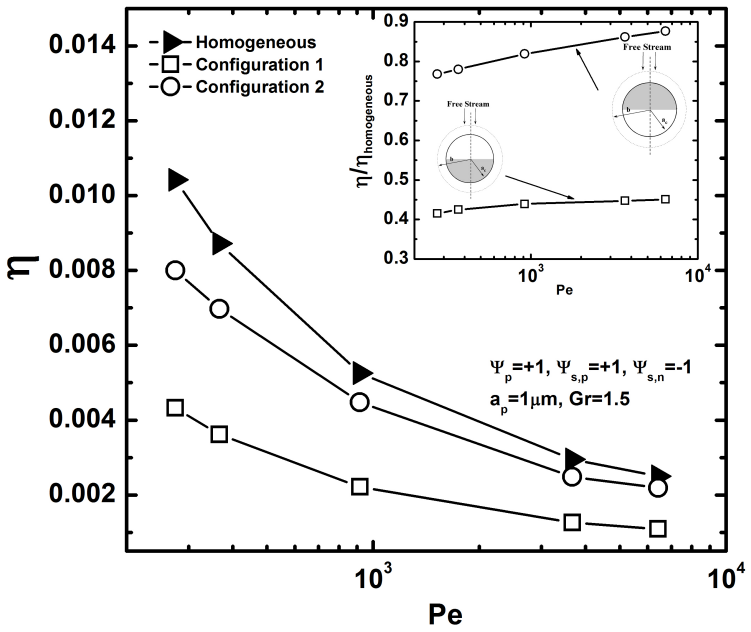


**Figure 4.3** – Particle deposition efficiency and its dependence on Peclet number for a homogeneously favorable collector and half favorable collector with two possible configurations described earlier. Comparison of the deposition efficiencies of the half favorable collector with the homogeneously favorable collector for different Peclet numbers under the same operating parameters (inset).

a homogeneous collector (inset Figure 4.3), it is remarkable to note that the deposition rate on a Janus collector under Configuration 2 is almost identical to that of a homogeneous collector (almost 80 percent minimally). Thus, it can be conclusively summarized that, a Janus collector under Configuration 2 can be as effective in particle retention as a homogeneous collector. Also, Figure 4.3 indicates the relative insignificance of the lower half of the collector on particle deposition even when it is attractive. The advantages of using a Janus collector over a homogeneous collector will be discussed later.

Having established that a half favorable collector has far superior deposition characteristics under Configuration 2 compared to that in Configuration 1, the present study now analyzes the variation of particle retention behavior with tilt angle ($\chi$). For non zero tilts, the deposition behavior in the right and left halves of the unit cell are different due to the combined effect of gravity and the fluid flow field. Figure 4.4(a) shows a somewhat sigmoidal behavior for both curves. The deposition efficiency drops as $\chi$ is increased in

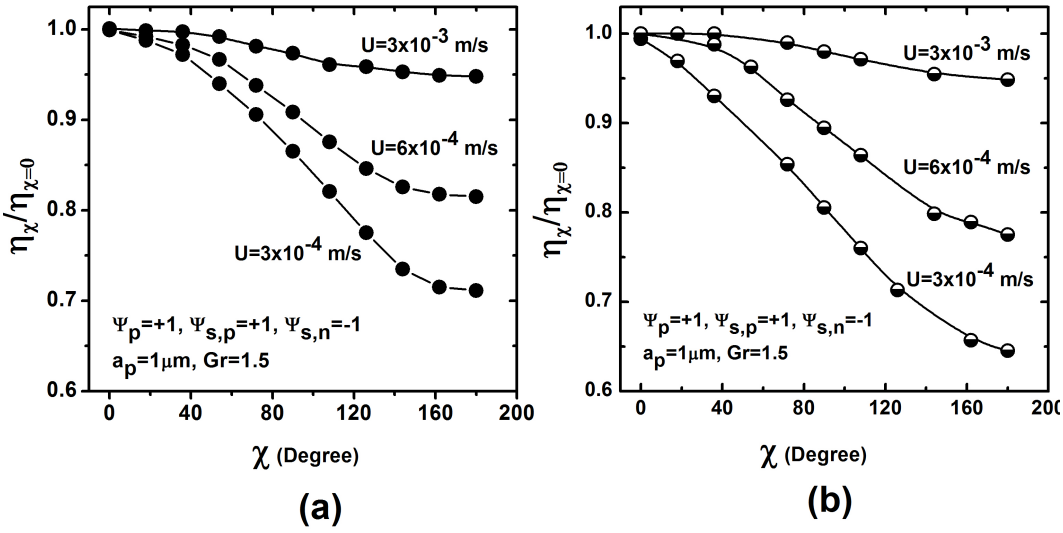


**Figure 4.4** – (a) Variation of single collector efficiency with tilt angle ($\chi$) for a homogeneous collector at three different velocities (b) Variation of single collector efficiency with tilt angle ($\chi$) for a Janus collector (configuration 2) at three different velocities.

both cases. However, for a half favorable collector, the deposition efficiency suffers a slightly greater dip compared to the homogeneous collector. For a gravity assisted flow scenario, the effect of gravity in aiding particle deposition is maximum. As $\chi$ increases, the favorable impact of gravity in aiding deposition decreases. At $\chi = 180$ degrees, i.e. for gravity opposed flow, the deposition efficiency is significantly reduced compared to a vertically downward flow because in the attractive half, gravity hinders deposition. Figure 4.4(b) depicts the variation in deposition efficiencies at different tilt angles for three different velocities. At higher velocities reflecting higher convection rate, the deposition efficiency becomes less sensitive to the tilt. This is because, at higher velocities, the effect of gravity is masked by the convective flow.

## 4.4 Particle Deposition onto Patterned Collectors

In this section, the deposition results from a micropatterned charged collector surface are discussed. As for a half favorable-half unfavorable collector, the particle concentration distribution due to the periodic colloidal interactions near the collector surface is investigated. The concentration distribution provides the first picture of the particle accumulation around the collector and hence gives an indication of the deposition process.

Figure 4.5 shows the variation of scaled particle concentration with tangential position on the surface of a heterogeneous collector at a separation distance of approximately 5 nm from the collector surface (close to the collector). The collector surface is patterned with alternate stripes of scaled surface potentials $\Psi_{s,p} = +1$ and $\Psi_{s,n} = -1$. The angular width of each of these stripes is 3°, making the collector 50 percent favorable to deposition ($\lambda_p = 0.5$). A particle radius of 1 micron, $\kappa a_p = 100$ and $Gr = 0.37$ were used for this simulation. The scaled surface potential for the particle is given as $\Psi_p = +1$. The particle concentration shows a periodic profile in the tangential direction with zero concentration over the unfavorable sections due to the repulsive colloidal interactions. Over the favorable sections, however, the particle concentration indicates a sharp rise at the leading edge of each favorable stripe.

The concentration profile varies as the particle traverses the arc length around the collector. Near the forward stagnation line, a sharp peak is observed at the leading edge of each favorable stripe following which the concentration decays rapidly to settle to a constant value over the remaining part of the favorable stripe. The concentration profile closely follows the periodic nature of the surface potentials on the collector. The sharp rise in concentration near the leading edge of the favorable stripe indicates an accumulation of particles at that location. Since the particles cannot come close to the surface over the unfavorable stripe due to the repulsive interactions, they are convected to the next favorable stripe. As soon as the particle reaches the favorable section, it experiences an attraction and deposits immediately on the collector surface. The height of the peak decreases with distance away from the forward stagnation line due as most particles will tend to deposit on the

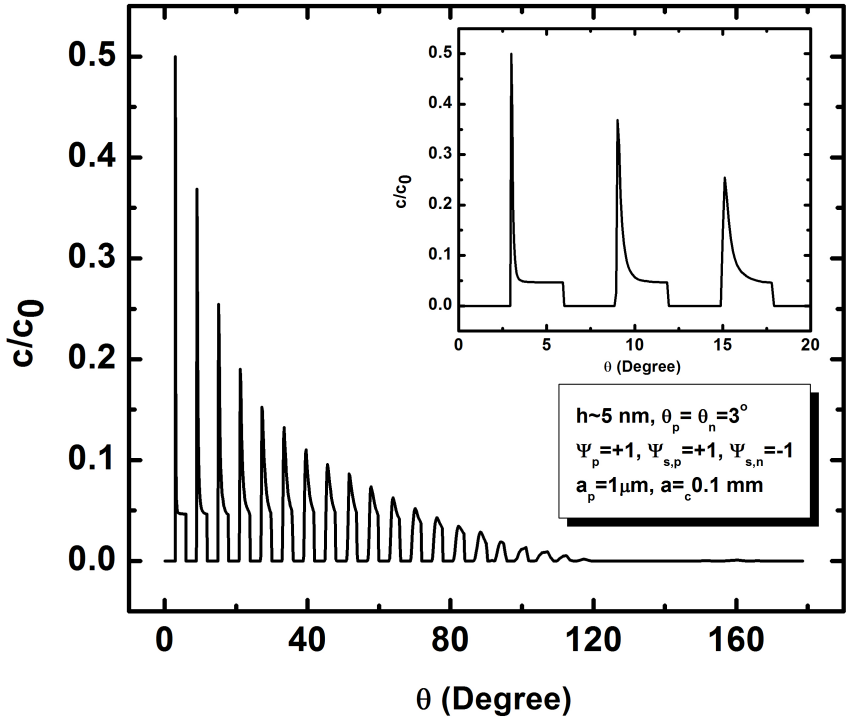


**Figure 4.5** – Variation of scaled particle concentration with tangential position on the surface of a heterogeneous collector at a separation distance of approximately 5 nm from the collector surface. (Inset) Scaled particle concentration as a function of tangential position near the forward stagnation line ($0° \leq \theta \leq 20°$). $\kappa a_p = 100$ and $Gr = 0.37$ were used for this simulation.

first favorable stripe and hence the probability of particle accumulation over the next set of favorable stripes gradually decreases.

At distances further away from the forward stagnation line, the peaks at the leading edge of each favorable stripe becomes smoother and the particle concentration does not decay continuously till the end of the stripe without settling to a constant finite value. Interestingly, the peaks also tend to gradually shift slightly to the right of the leading edge as tangential distance increases. Similar behavior has also been reported for a impinging jet flow over a micropatterned flat plate [Nazemifard et al., 2006]. The gradual shift to the right indicates the presence of an inaccessible region over the favorable stripe which increases as the intensity of shear flow increases with tangential distance from the forward stagnation line.

It is also interesting to note from Figure 4.5 that despite the presence of favorable stripes, there is virtually no deposition in the trailing half of the collector ($\theta \geq 90°$). This is unique to the cell model geometry. In the lower half of the collector, the fluid flow tends to carry the particle away from the collector surface as well as the fact that gravity opposes deposition in the lower half. This further establishes the relative insignificance of surface interactions in determining deposition in the lower half of the collector. The particles tend to be sensitive to the surface interactions only in the upper half. The simulation results also showed that even upon reducing the Peclet number, there is no deposition in the lower half. However, as Peclet number decreases, the concentration peak near the stagnation region decreases in magnitude.

Having analyzed the particle concentration around the collector, it is now important to investigate the particle flux (represented by the local Sherwood number) on the collector surface. It is also essential to understand how the presence of patterned heterogeneity modifies the local particle flux on the collector surface compared to that of a homogeneous favorable collector. Figure 4.6 compares the variation of local Sherwood number with tangential position on the collector surface for a patchy collector and a homogeneous favorable collector (Figure 4.6(inset)). The simulation parameters are identical to that in Figure 4.5 and the local Sherwood number is calculated at the surface of the collector (at the cut off distance of 1 nm).

The local Sherwood number is basically an indication of the radial particle flux at the collector surface. Figure 4.6 indicates that the local Sherwood number shows the same periodic variation with $\theta$ as was observed with concentration in Figure 4.5. Like the scaled particle concentration, the local Sherwood number is zero over the unfavorable stripes indicating no local deposition. The particle flux increases sharply at the leading edge of the favorable stripes near the forward stagnation line before decaying to a constant value similar to the particle concentration. The local Sherwood number also displays the same decay and shift of the peaks to the right of the leading edge of the favorable stripe as $\theta$ increases indicating an inaccessible fraction over the favorable stripes [Nazemifard et al., 2006]. For the lower half of the collector, Figure 4.6 also indicates virtually no particle deposition.

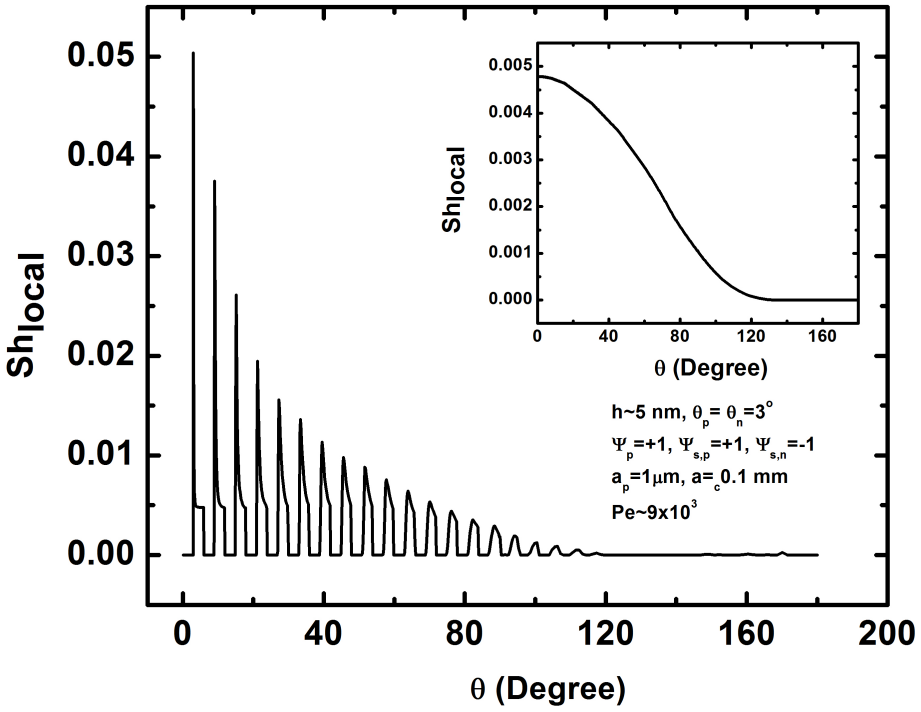


**Figure 4.6** – Comparison of variation of local Sherwood number for a homogeneous favorable collector (inset) and heterogeneous collector with patterned surface charge heterogeneity. Parameters used for this simulation are identical to that in Figure 4.5. The local Sherwood number is calculated at the surface of the collector (at the cut off distance of 1 nm).

Comparison of the Sherwood numbers in Figure 4.6 indicates a significant difference in the local deposition rates of the microscopically heterogeneous and homogeneous collector. Near the forward stagnation line the local Sherwood for a heterogeneous collector is almost ten times that of a homogeneous collector. This is attributed to the tangential convection of particles over the first unfavorable stripe where no deposition occurs resulting in a much higher particle flux over the first favorable stripe compared to that of a homogeneous collector. This is significant as it indicates that having small pockets of favorable area on the otherwise unfavorable collector can result in significantly high local deposition rates at these sites compared to the deposition on a homogeneous collector. It shows that microscopic heterogeneity can play significant roles in preferentially "doping" a particular site with particles of a specific

kind. Essentially it leads to controlled deposition and can have significant implications in areas spanning drug targeting to developing novel materials with surface arrays. It is however important to note that although the local deposition rate for a 50 percent favorable collector is higher than that of a homogenous favorable collector, the overall deposition rates of the two collectors could be comparable.

### Comparison of the Convection-Diffusion-Migration Model with the Patchwise Heterogeneity Model

The overall deposition rate for a heterogeneous collector consisting of favorable and unfavorable stripes, as given by the patchwise heterogeneity model in context of the Eulerian analysis [Song et al., 1994] is

$$Sh_{avg} = \lambda_p Sh_{avg,f} + (1 - \lambda_p) Sh_{avg,uf} \tag{4.9}$$

where $Sh_{avg,f}$ and $Sh_{avg,uf}$ are the average deposition rates over homogeneously favorable and homogeneously unfavorable surfaces respectively. Since $Sh_{avg,uf} = 0$, the patchwise heterogeneity model reduces to a linear relationship between the average deposition rate ($Sh_{avg}$) and the favorable area fraction on a collector surface ($\lambda_p$). Thus, for a surface with 50 percent favorable area fraction (i.e. $\lambda_p = 0.5$), the average Sherwood number for the heterogeneous collector is given as $Sh_{avg} = 0.5 Sh_{avg,f}$.

The patchwise heterogeneity model predicts overall deposition rates independent of the spatial characteristics of the surface heterogeneity. However, as Figure 4.6 clearly points out, the local deposition rates at a given tangential position for a patchy collector is significantly higher than that of a homogeneous collector owing to the coupling of various transport mechanisms (for example, near the stagnation point, $Sh_{local}$ for a patchy collector is 10 times higher than that of a homogeneous collector). Since, the overall deposition rate is evaluated by tangential averaging of the local deposition rates on the collector surface, the comparatively high deposition rates over the favorable stripes compensates for the zero deposition rates over the unfavorable stripes. As a result, the overall deposition rates of the patchy collector is comparable to the overall deposition rate of a homogeneous collector even at 50 % favorable coverage.

In order to compare the current convection-diffusion-migration model with the patchwise heterogeneity model exhaustively, the dependence of the overall deposition rate on the favorable area fraction must be analyzed. For a patterned heterogeneous collector with a constant pitch (p), the favorable area fraction ($\lambda_p$) can be altered by changing the ratio of the favorable stripe to the unfavorable stripe ($w_n/w_p$).

Figure 4.7 shows the variation of scaled overall particle deposition rate $Sh_p/Sh_0$ with favorable area fraction of the collector, $\lambda_p$. The open symbols (squares and circles) denote the results from the convection diffusion migration model for two particle sizes (0.5 micron and 1 micron, respectively) while the line with closed triangles are the overall deposition rate prediction from the patchwise heterogeneity model. Figure 4.7(a) and (b) show the dependence of the overall deposition rate on the Peclet number (or the fluid flow rate). It is evident from 4.7 that the numerical results from the convection-diffusion-migration model deviates significantly from the patchwise heterogeneity model. This deviation is however dependent on the coupling of other transport mechanisms such as particle size, collector size and flow velocity. For all the simulations, a slight increase in the value of $\lambda_p$ (below $\lambda_p = 0.5$) results in a significant increase in the value of overall deposition rate. The dependence of the overall deposition rate on the favorable area fraction gradually decreases beyond ($\lambda_p = 0.5$) indicated by the flattening of the plots for all cases. Also for all the simulation conditions depicted, at $\lambda_p = 0.5$, the overall deposition rate is inside 20% of the completely favorable analogue.

Figure 4.7 also shows the variation of the scaled particle deposition rates with favorable area coverage for two particle sizes and two Peclet numbers (obtained by changing the flow velocity). The deviation of the overall Sherwood number predicted by the numerical model from the patchwise heterogeneity model follows the same trend as the impinging jet flow discussed by Nazemifard et al. [2006]. However, the variations with Peclet number were not discussed for the impinging jet flow system. Figure 4.7(a) depicts a strongly convective system. The initial response of the deposition rates for the two particle sizes are almost the same. The difference in the deposition rates of the two particles are only observed for $\lambda_p > 0.3$. For higher $\lambda_p$, the 0.5 micron par-

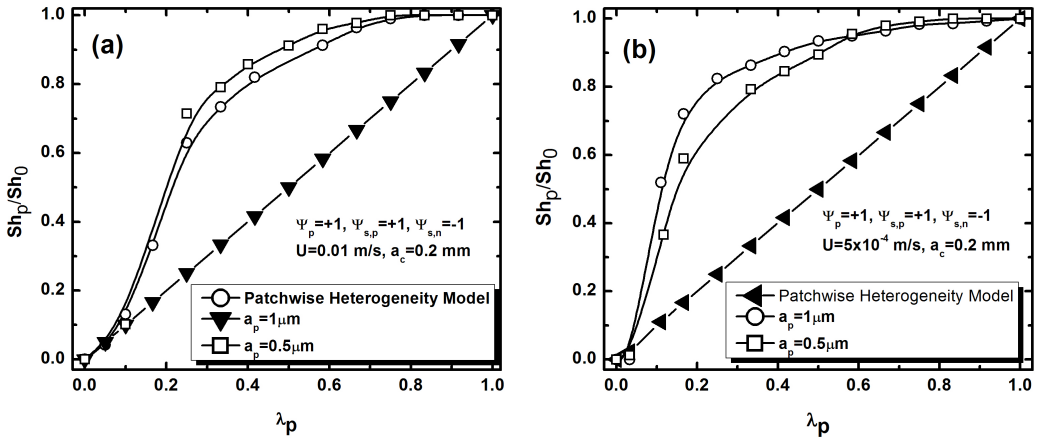


**Figure 4.7** – Variation of scaled overall particle deposition rate $Sh_p/Sh_0$ with favorable area fraction of the collector, $\lambda_p$. The open symbols (squares and circles) denote the results from the convection diffusion migration model for two particle sizes (0.5 micron and 1 micron respectively) while the line with closed triangles are the overall deposition rate prediction from the patchwise heterogeneity model. (a) Comparison of the present model with the patchwise heterogeneity model for a strongly convective transport system ($U = 0.01m/s$). (b) Comparison of the present model with the patchwise heterogeneity model for a strongly diffusive transport system ($U = 5 \times 10^{-4}/s$). The scaled surface potentials used for this simulation are $\Psi_p = +1$, $\Psi_{s,p} = +1$, $\Psi_{s,n} = -1$. The ionic strength of the solution is $I = 1 \times 10^{-3}M$.

ticle has greater deposition rates compared to a 1 micron particle. This is primarily due to the fact that the larger particle is convected tangentially at a much greater rate thereby making it less sensitive to the colloidal interactions in the radial directions. For a strongly diffusive system however (Figure 4.7(b)), the behavior is just the opposite. Here, the tangential convection is weak and the larger particle feels the interactions more intensely compared to the smaller one. Thus, the deposition rate is greater for a larger particle. The initial response is also different due to the difference in the intensity of

the particle-collector interactions which now predominates in the absence of the masking effect of the tangential convection. This shows the effect of the complex transport mechanisms on the deposition behavior and how they cause a deviation from the analytical patchwise heterogeneity model. The patchwise heterogeneity model however serves as a good limiting solution at low $\lambda_p$ values as long as the width of the stripes is larger than the particle diameter.

Figure 4.8 shows the change in deposition efficiencies with tilt orientation compared to a vertically downward flow orientation ($\chi = 0$). As explained earlier, the deposition efficiency varies upon changing the orientation due to the role of gravity. Upon increasing the Peclet number, by increasing flow velocity, the effect of the gravity is masked as shown by the flattening nature of the plots with increasing Peclet number. The results indicate that for high Peclet number flows, the deposition efficiency hardly changes with change in orientation. However, as Peclet number is reduced, the effect of gravity is more predominant and the dip in the curve is more significant. This deviation depends entirely upon the non dimensional gravity number ($Gr = 4/3\pi a_p^3 \Delta\rho g$) and increases as the relative density of the particle increases.

## 4.5 Applications of Janus and patchy Collectors in Particle Deposition

The simulation results highlight three critical aspects about deposition on patchy and Janus collectors.

- The trailing half (or lower half) of the collector is insensitive to deposition even if it is favorably charged (Figure 4.6).
- A heterogeneous collector with even 50 percent favorable surface coverage, can have deposition characteristics very similar to its completely homogeneous analogue (Figure 4.7).
- At lower flow velocities, deposition efficiency is higher (Figure 4.3).

Is it possible to capitalize on these characteristics and use such collectors with artificial surface heterogeneity to design energy efficient filter beds? As the results have shown that the trailing half of a stationary, supported collector

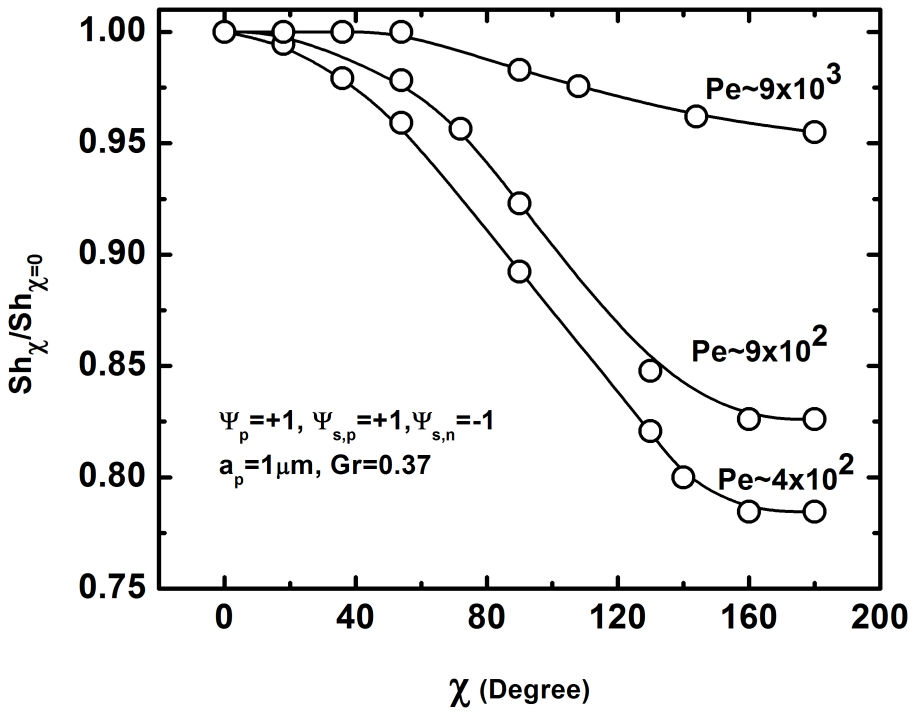


**Figure 4.8** – Comparison of deposition efficiencies at a given tilt to vertically downward flow. Parameters used for this simulation are identical to that of 4.7.

is relatively clean, if a mechanism can be developed to rotate the collector, it would facilitate deposition on the cleaner trailing half. Keeping this in mind, it is feasible to use the patchy or Janus collectors in a fluidized bed filter system, as depicted in the schematic of Figure 4.9. In such a system, the collectors could be kept floating with the fluid flow imposed in a direction opposite to the gravity, which will allow the collectors to rotate and use the cleaner half for deposition. Since the collectors have surface charge, it is also possible to rotate the collectors using external force fields. However, the former option is more energy efficient. Such a filter system would have longer operational life and better particle retention properties. In most supported filter beds, the bed porosity is constant and the collectors are held tightly in a close packed formation. In a fluidized bed system, however, a combination of fluid drag and the inter-collector interactions can be used to vary the filter porosity. Higher porosity would mean a lower pressure drop across the filter bed defined by Darcy's equation $dp/dz = -\mu u/k$ (where $u$ is the superficial velocity, $\mu$ is the

fluid viscosity and $k$ is the bed permeability). This would result in further reduction in pump energy. Secondly, an increase in porosity would also lead to lower interstitial flow velocities thereby increasing the deposition efficiency (*cf.* Figure 4.3). Using such patterned collectors, two types of charged particles can be collected on the same collector with near homogeneous efficiency.

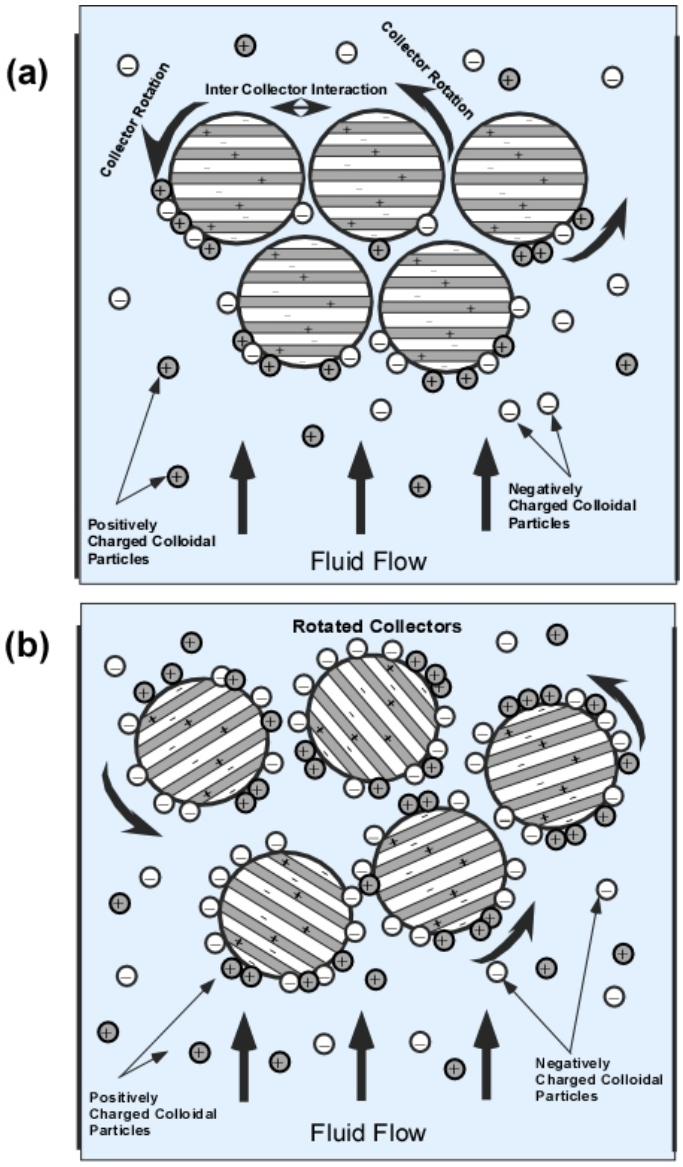


**Figure 4.9** – Schematic of a fluidized field variable porosity filter.

With Janus collectors, instead of being part attractive and part repulsive, it is possible to make the two halves attractive to different extents. Collectors with different Debye lengths in the two halves have been used in studies per-

taining to aggregation [Pardhy and Budhlall, 2010]. Such collectors could be used to preferentially capture particles in a suspension. They could also be used in separation of components from emulsions where the components would have varying magnitudes of attraction towards the two halves of the collector surface.

## 4.6 Summary

An analysis of particle transport around a patterned charge heterogeneous spherical collector is presented in this chapter using the sphere-in-cell approach. The cases discussed are for a Janus collector and a patchy collector with micropatterned surface charge distribution. In both cases the results indicate particle accumulation at the leading edge of the favorable stripe due to tangential transport of particles over the unfavorable section of the collector. For a sphere-in-cell geometry, the model shows the relative insignificance of lower half of the collector playing a dominant role in the deposition process. For Janus and patchy collectors, the effect of different flow orientations were also analyzed. The results indicate the possibility of designing filter beds using these heterogeneous collectors which can have longer operational life compared to homogeneous collectors. For a micropattened charge surface, the comparison of the overall deposition rates with patchwise heterogeneity model showed significant deviation. Having comprehensively analyzed particle deposition onto spherical collectors (both homogenous and chemically heterogeneous), in the next chapter we shall investigate particle transport in a microchannel with chemical heterogeneity on its walls. The study would complete looking at the entire gamut of particle transport problems in porous media geometries.

# Chapter 5

# Transport and Deposition of Colloidal Particles in a Patterned Cylindrical Microchannel [1]

## 5.1 Introduction

In this chapter, we look at particle transport in a cylindrical microchannel with surface charge heterogeneity on its walls. Rock structures, which classify as natural porous media, are often comprised of a network of pores and throats. Most of these pores are arbitrary shapes rendering them inappropriate for systematic analysis without making suitable approximations. In this chapter we present a numerical model which investigates particle transport in a chemically heterogeneous pore approximated as a cylindrical microchannel. The model also has relevance to several microfluidic/nanofluidic devices in which particle transport in microchannels is an integral part. A lot of research has been performed to investigate electrokinetic and particle transport in homogeneous microchannels. There is, however, a dearth of theoretical work in which particle transport is analyzed in a microchannel with chemical heterogeneity. Following the trend from the previous chapters, we shall present the variation of typical particle transport parameters that characterize deposition. The work is intended to provide a direction in improving existing pore network models by incorporating surface charge heterogeneity, thereby making them

[1] Parts of this chapter have been published in *Microfluidics and Nanofluidics*, July 2011, doi:10.1007/s10404-011-0847-9 *In press.*

more practical and realistic.

## 5.2 Mathematical Modeling

### 5.2.1 Patterned Microchannel Geometry with Poiseuille Flow

A schematic representation of patchy microchannel with micropatterned surface charge distribution is indicated in Figure 5.1. The walls of the channel consists of co-axial circular rings with alternate positive and negative surface potentials with the particle assumed to be positively charged. The velocity profile inside the microchannel is assumed to be fully developed and parabolic in nature. In the absence of gravity, the model is axisymmetric in nature and 2D analysis can be performed to evaluate particle transport. Figure 5.1(c) shows the pitch length ($p$) and the negative and positive band widths of the co-axial rings denoted by $w_n$ and $w_p$, respectively.

A qualitative picture of the trajectory of the particle as it gets transported through the microchannel is shown in Figures 5.1(b) and (c). The repulsion over the positive band makes the particle to move away from the channel wall and towards the centerline followed by an attractive stretch which causes it to migrate towards the wall. All other features of the original model developed by Adamczyk and van de Ven [1981] for particle transport in a homogeneously attractive channel are retained in the present analysis. For a positively charged particle as in the present analysis, the ratio of the width of the negative band ($w_n$) to the pitch length ($p$) quantifies the fraction of the microchannel wall surface area that is attractive and favors deposition. The favorable area fraction is denoted as $\lambda_p = A_f/A$ where $A_f$ is the area of the microchannel wall favoring deposition and $A$ is the total surface area of the microchannel wall. Thus, the area fraction can be calculated as

$$\lambda_p = \frac{A_f}{A} = \frac{\sum_{n=1}^{n=N_b} \int_{(n-1)p+w_p}^{np} 2\pi R dL}{2\pi RL} \tag{5.1}$$

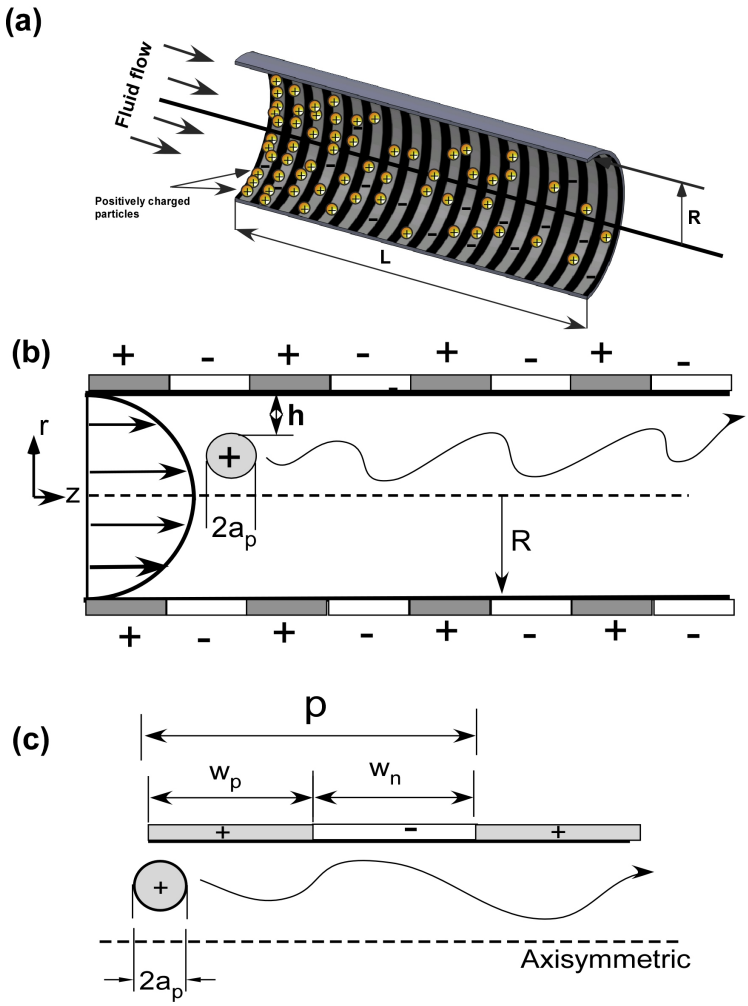


**Figure 5.1** – Schematic of a patterned microchannel geometry with Poiseuille flow profile. The model is axisymmetric about the centerline. $R$ is the radius of the microchannel and $a_p$ is the particle radius. The schematic shows the oscillatory trajectory of the particle under the influence of the attractive and repulsive surface interactions. (a) 3D schematic representation of positively charged particles depositing at the leading edge of the favorable stripes along the length of the microchannel (cut section shown). The grey bands are negatively charged and the black bands are positively charged. (b) 2D axisymmetric view of the microchannel geometry showing the parabolic velocity profile, the channel length, particle radius and the surface charges. Sub-part (c) shows the zoomed in section of one pitch ($p$) length. $w_n$ and $w_p$ are the negative and positive band widths of the co-axial rings.

where $N_b$ is the total number of bands on the channel wall and L is the microchannel length. Equation 5.1 can be simplified to

$$\lambda_p = \frac{A_f}{A} \simeq \frac{w_n}{p} \tag{5.2}$$

The present study considers a positively charged particle and the first ring of each band is always positively charged and unfavorable to deposition. The charge heterogeneity is incorporated by varying the scaled surface potential ($\Psi_s$) over the white and shaded regions as reported in Figure 5.1(b), giving it a periodic profile along the channel length ($L$). Thus, $\Psi_{s,n}$ and $\Psi_{s,p}$, would denote the negative and positive scaled surface potentials. The other approximations involved with the modeling are the same as they were for the patterned spherical collector in chapter 4.

### 5.2.2 Governing Particle Transport Equations

Particle transport in the microchannel is governed by the steady state C-D-M equation given by Equation 3.1. For solving Equation 3.1, the fluid velocity vector must be known. The present model employs a fully developed, laminar parabolic velocity profile (Poiseuille flow) given by

$$u_z(r) = 2U_m \left[1 - \left(\frac{r}{R}\right)^2\right] \tag{5.3}$$

where $u_z(r)$ is the fluid velocity in the axial direction, $U_m$ is the mean flow velocity, $r$ is the local radial co-ordinate in the microchannel and $R$ is the microchannel radius. For the Poiseuille flow profile, $u_r(r) = 0$ (i.e, zero radial velocity). The hydrodynamic coupling of the fluid and particle velocities are easily obtained by incorporating suitable hydrodynamic correction factors $f_1(H)$, $f_2(H)$, $f_3(H)$ and $f_4(H)$ [Goldman et al., 1967, Kemps and Bhattacharjee, 2009]. Thus, $v_r(r) = f_1(H)f_2(H)u_r(r)$ and $v_z(r) = f_3(H)u_z(r)$ where $H$ is the dimensionless surface to surface separation distance between the particle and the microchannel wall (defined as $H = h/a_p$). Since $u_r(r) = 0$, there is no particle convection component in the radial direction (i.e, $v_r(r) = 0$) It must be mentioned here that the correction factors used in this study apply

for a sphere approaching a flat surface. For the ratio of particle size to channel radius used in the simulations ($a_p/R \leq 0.05$ maximally), the particle does not feel the curvature of the channel wall and hence these correction factors can be employed. In general, this approximation is correct as long as $a_p/R \ll 1$ [Adamczyk and van de Ven, 1981]. For comparable particle to channel radius aspect ratios, other correction factors are available in literature which can also be easily incorporated into the model [Al Quddus et al., 2008]. Even in those expressions, it has been shown that for small aspect ratio systems ($a_p/R < 0.1$), the hydrodynamic corrections are insensitive to the channel wall curvature. The particle diffusion tensor is defined in the same was as it was done for the spherical collector case.

The non-hydrodynamic forces considered here are the attractive van der Waals and the electrostatic double layer interactions. Thus, the net radial force on the particle is given as

$$F_r = -\frac{d\phi_T}{dr} \tag{5.4}$$

where $\phi_T$ ($= \phi_{Ham} + \phi_{EDL}$) is the total interaction energy due to attractive van der Waals interaction and electrostatic double layer interactions. We employ the Derjaguin expression for the unretarded van der Waals interaction energy in this model (Equation 2.13). For the electrostatic double layer interactions, the well known Hogg, Healy and Fuerstenau (HHF) Hogg et al. [1966] expression is used (Equation 4.4).

The C-D-M equation for particle transport in a cylindrical channel with Poiseuille flow is given by Adamczyk and van de Ven [1981]. Upon formulating the equation explicitly and grouping the derivative terms, the C-D-M equation can be expressed as

$$\frac{\partial C^*}{\partial Z} = a_1(H)\frac{\partial^2 C^*}{\partial H^2} + a_2(H)\frac{\partial C^*}{\partial H} + a_3(H)C^* \tag{5.5}$$

where $C^*(= c/c_0)$ is the scaled particle concentration. The coefficients $a_1(H)$, $a_2(H)$ and $a_3(H)$ are

$$a_1(H) = f_1(H) / \left[ Pe f_3(H) \{ 2 - (H+1)\gamma \} \right] \tag{5.6}$$

$$a_2(H) = \left[ f_1(H) \frac{\partial \Phi}{\partial H} + \frac{\partial f_1(H)}{\partial H} - f_1(H)\gamma \right] / \left[ Pe f_3(H) \{ 2 - (H+1)\gamma \} \right] \tag{5.7}$$

$$a_3(H) = \left[ \frac{\partial f_1(H)}{\partial H} \frac{\partial \Phi}{\partial H} + f_1(H) \frac{\partial^2 \Phi}{\partial H^2} - \gamma f_1(H) \frac{\partial \Phi}{\partial H} \right] / \left[ Pe f_3(H) \{ 2 - (H+1)\gamma \} \right] \tag{5.8}$$

Note that the correction factor $f_2(H)$ does not appear in Eqs. 4.5, 4.6, 4.7 due to the absence of particle convection in the radial direction. However, migration due to the colloidal interactions, which is responsible for the transport of particles towards the wall is corrected by the factor $f_1(H)$. A list of relevant non-dimensional parameters used for solving Equation 5.5 is provided in Table 5.1.

**Table 5.1** – Dimensionless groups and constants used in the scaled Convection-Diffusion-Migration equation

| Dimensionless group | Expression |
|---|---|
| Scaled surface to surface separation distance | $H = h/a_p$ |
| Particle Peclet number | $Pe = \frac{2U_m a_p^3}{D_\infty R^2}$ |
| Scaled total interaction energy | $\Phi = \frac{\phi_T}{k_B T}$ |
| Particle aspect ratio | $\gamma = a_p/R$ |
| Scaled distance along z | $Z = \frac{z}{R}$ |
| Scaled Surface Potential | $\Psi = \frac{ze\psi}{k_B T}$ |

The boundary conditions used for solving Equation 5.5 are

$$C^* = 1 \qquad at \quad Z = 0 \quad (h \neq d_{min}) \tag{5.9}$$

$$C^* = 0 \qquad at \quad h = d_{min} \qquad (perfect\ sink) \tag{5.10}$$

$$\frac{\partial C^*}{\partial H} = 0 \qquad at \quad H = R/a_p \qquad (symmetry\ along\ centerline) \qquad (5.11)$$

noindent Here, Here, $h$ is the dimensional particle-wall separation distance and $d_{min} = 1\ nm$ is the wall cut off separation to prevent non-physical divergence of van der Waals interaction at contact. The local Sherwood number which quantifies local deposition is evaluated as Adamczyk and van de Ven [1981]

$$Sh = \left[ f_1(H) \frac{\partial C^*}{\partial H} \right]_{d_{min}} \qquad (5.12)$$

Similarly, the overall deposition number ($Sh_{avg}$) is obtained by integrating the local Sherwood number over the entire surface of the microchannel [Adamczyk and van de Ven, 1981]. Thus

$$Sh_{avg} = \frac{R}{L} \int_0^{L/R} ShdZ \qquad (5.13)$$

It is observed that Equation 5.13 is independent of $\theta$ (tangential) due to axisymmetry. Although Equation 5.12 is devoid of the particle interaction energy term, the change in deposition number due to the interaction is accounted for by the wall concentration gradient which is a function of the total interaction energy. The numerical scheme employed for solving the governing set of equations is identically similar to those described in Chapters 3 and 4. The parameters used for the simulations in this chapter are given in Table 5.2

**Table 5.2** – Physical and Chemical Properties of the system used in the simulations

| Property | Value |
|---|---|
| Particle radius, $a_p$ | $0.5 - 1\mu m$ |
| Fluid viscosity, $\mu$ | $1 \times 10^{-3} N - s/m^2$ |
| Free stream velocity, $U$ | $1.0 \times 10^{-5} - 1.0 \times 10^{-2}\ m/s$ |
| Temperature, $T$ | $298\ K$ |
| Electronic charge, $e$ | $1.6 \times 10^{-19}\ C$ |
| Permittivity of vacuum, $\epsilon_0$ | $8.85 \times 10^{-12}\ C/Vm$ |
| Dielectric constant, $\epsilon$ | 78.54 |
| Hamaker constant, $A_H$ | $10^{-21}\ J\ -\ 10^{-20}\ J$ |
| Solution ionic strength, $I$ | $10^{-1}\ M$ |
| Valence of ion, $z$ | 1 |
| Channel Radius, $R$ | $10\ -\ 50\ \mu m$ |
| Channel Length, $L$ | $50\mu m\ -\ 0.1\ mm$ |

## 5.3 Results and Discussion

### 5.3.1 Local Deposition Behavior

For the heterogeneous microchannel, it is important to first investigate the near wall concentration profile along the length of the channel. Figure 5.2(a) depicts the variation of near wall concentration along the length of the channel. The dashed line represents the concentration profile for a homogeneously attractive channel while the solid line represents the concentration profile for a patchy (micropatterned) channel. The inset plot represents the magnified picture of the concentration profile for $z/a_p < 20$. The near wall distance was chosen to be 5 nm which lies just outside the secondary minima. The concentration profile follows the oscillatory surface potential profile along the channel length. The zero concentration regions are the repulsive regions where no particle penetration occurs and consequently there is no deposition.

Three important observations are made from Figure 5.2(a). Firstly, a comparison with the concentration profile of the homogeneous microchannel shows that for a micropatterned microchannel, the concentration peak over the attractive stripe is significantly higher (i.e, the solid line peaks are much higher over the attractive bands compared to the dashed lines). This is due to the fact that the particles that are not deposited over the unfavorable region gets convected over to the next favorable stripe. Secondly, the concentration peaks

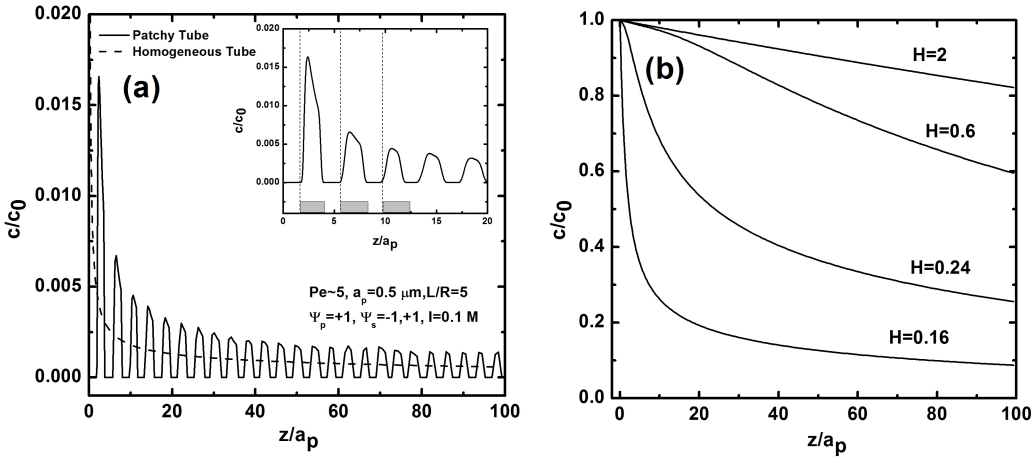


**Figure 5.2** – (a) Variation of near wall concentration along the length of the channel. The dashed line represents the concentration profile for a homogeneously attractive channel while the solid line represents the concentration profile for a patchy (micropatterned) channel. The inset plot represents the magnified picture of the concentration profile for $z/a_p < 20$. Shaded regions depict the attractive stripes and dashed vertical lines have been drawn to show how particles tend to deposit near the leading edge of the favorable stripes. (b) Variation of the concentration profile along the channel length at different separation distances (scaled) for a homogeneous channel. Parameters used for this simulation are $L/R = 5,\ a_p = 0.5\ \mu m,\ I = 0.1\ M,\ p = 4\ \mu m$

tend to form at the leading edge of each favorable stripe. Similar behavior has also been reported by Nazemifard et al. [2006] for an impinging jet geometry. This behavior is expected as most of the particles will deposit as soon as they experience an attraction from the wall. The height of the peaks decreases upto a certain distance along the channel length and finally become constant at a certain value. It is observed that beyond roughly the half channel length, the concentration profile on each of the favorable stripes is almost identical. Finally, there is a greater probability that a particle might travel the entire length of a micropatterned channel than compared to a homogeneous channel.

This is evident from the finite concentration peaks further down the channel length which is higher compared to the case of a homogeneous channel. Hence, it can be concluded that deposition is more uniform along the length of a micropatterned channel wall compared to a homogeneous one in which all the particles will deposit within a very short distance from the inlet.

Figure 5.2(b) depicts the concentration profile for a homogeneous microchannel at different separation distances from the wall. Thus, as the separation distance from the wall decreases, the concentration profile falls off more sharply due to the influence of the attractive particle-wall interactions. At further distances, most particles will travel the length of the channel almost unaffected. In other words, particles that are near the centerline would be transported along the microchannel without depositing. As can be seen from Fig.5.2(a), the concentration profile for the micropatterned channel oscillates around the dashed line. Hence, the flattening of the curves at a larger separation distance is observed even for the case of a micropatterned channel.

Once the concentration field and the corresponding gradients have been calculated in the computational domain, the local Sherwood number is calculated using Equation 5.12. Figure 5.3 depicts the variation of the local Sherwood number ($Sh_{local}$) along the channel length for two different Peclet numbers. The Peclet number in these simulations were varied by changing the fluid flow velocity. Comparison of the two subparts show that the height of the $Sh_{local}$ peak is higher for a higher Peclet number (28 at the first peak for Pe $\simeq$ 5 compared to 10 for Pe $\simeq$ 0.5). This again is due to convection along the flow direction making particles available for deposition over the favorable stripes at a faster rate. Also, the peaks at a lower Peclet number are much sharper compared to smoother peaks at a higher Pe. As convection increases, it tends to carry the particles faster allowing lesser time for the particles to deposit at a particular location on the wall. Thus, there is a smoother gradient in the Sherwood number along the flow direction as indicated by the rounded edges. Another important observation is that for lower Peclet numbers, there is very little deposition towards the end of the channel (i.e, very small peaks observed for $Pe = 5$ beyond the half channel length). Compared to this, at higher Peclet numbers, deposition is significant towards the end of the channel. Hence, one would expect the average deposition rate to be

higher for higher Peclet numbers. This also indicates that more uniform deposition can be achieved on the microchannel walls by allowing a faster flow rate.

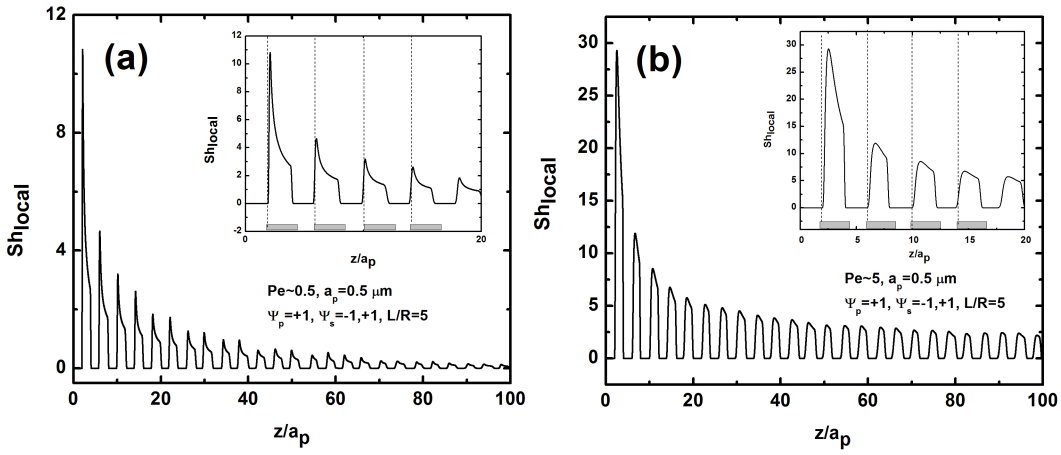


**Figure 5.3** – Variation of local Sherwood number ($Sh_{local}$) along the channel length for two different Peclet numbers. The shaded regions are the areas favoring deposition. Dashed vertical lines are drawn at the leading edge of each favorable stripe to highlight the fact that particles tend to deposit at the leading edge of these favorable stripes. The simulation parameters are the same as mentioned in Figure 5.2

### 5.3.2 Dependence of Deposition Behavior on Peclet number, Pitch Length and Favorable Surface Coverage

The overall deposition behavior of the channel is quantified by the average Sherwood number which is obtained by integrating the local Sherwood numbers over the length of the channel. Figure 5.4 shows the variation of the average Sherwood number with Peclet number for three different channel radii. As justified in the previous section, increased Peclet number would result in enhanced deposition of particles on the channel wall indicated by the higher

peaks further down the length of the channel. Again, this is expected as more particles are being made available for deposition to the attractive bands further down the length of the channel thereby increasing the average deposition. Upon increasing the channel radius, the deposition rate is observed to increase. The increase in channel radius yet keeping Peclet number constant ($Pe = 2U_m a_p^3/D_\infty R^2$) would require either a larger $a_p$ or larger $U_m$. A larger particle radius would mean that the particle interactions are stronger thereby increasing deposition and a higher fluid velocity would also increase the average deposition number due to the reasons mentioned earlier.

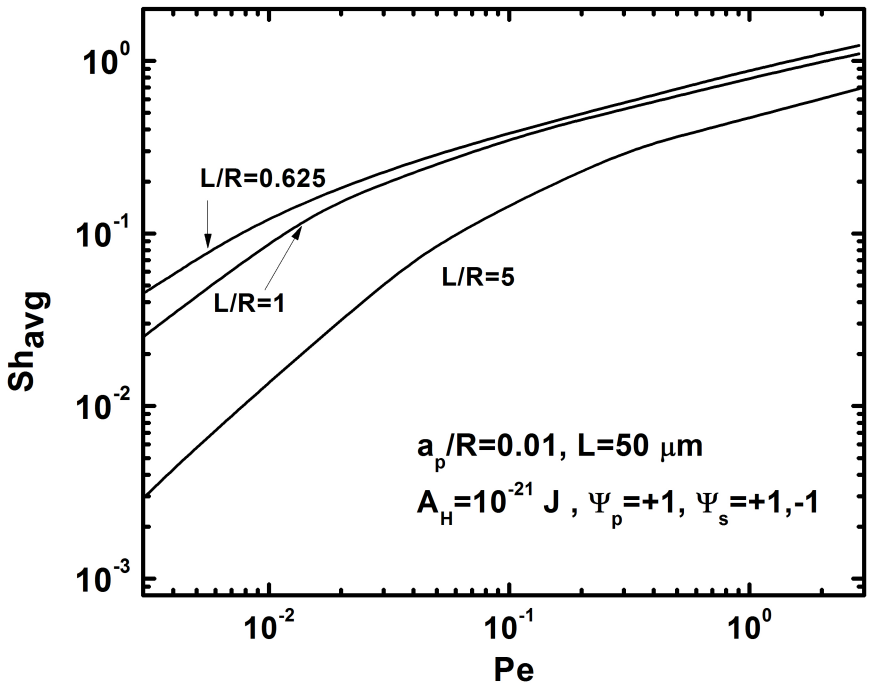


**Figure 5.4** – Variation of average Sherwood number with Peclet number for cylindrical channels with three different radii. The parameters used for this simulation are $A_H = 10^{-21}$ $J$, $p = 4$ $\mu m$, $L = 50$ $\mu m$, $a_p/R = 0.01$, $\lambda_p = 0.5$

Figure 5.5 shows the overall deposition rate due to the variation in the pitch length for two Peclet numbers. A larger $L/p$ ratio indicates smaller pitch width and thus smaller width of the positive and negative bands. The plot shows the variation in deposition rates at $\lambda_p = 0.5$. Upon increasing the

length to pitch ratio, the average deposition rate shows a tendency to increase initially before flattening out. As previously discussed, the deposition rates are higher for higher Peclet number. The figure indicates that although the fraction of the surface area favorable for deposition is the same, a larger number of favorable stripes will result in better deposition as a particle can access a larger number of favorable sections along a given length of the channel. As a limiting case, one can have a channel which is half favorable and half unfavorable along the entire microchannel length. In such a situation, only one half of the channel allows particle to deposit on the walls and there is a greater probability that a particle might be transported over the favorable section without depositing. Compared to this, if the width of the stripe is small there is a greater possibility of the particle being captured anywhere (on any one of the favorable stripes) along the length of the microchannel. Thus, the deposition is dependent on the distribution of the surface charge as well as the geometry and is not determined solely by the $\lambda_p$ parameter.

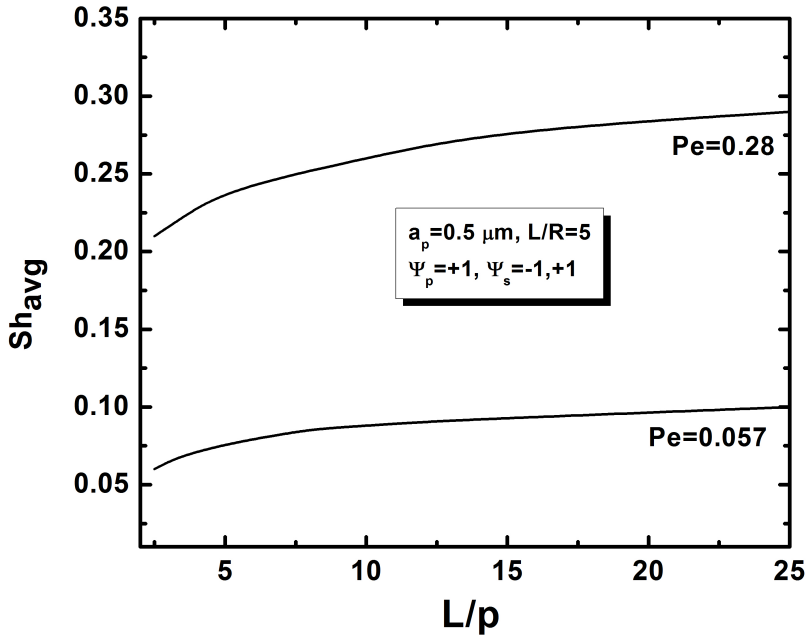


**Figure 5.5** – Variation of overall deposition rate with pitch length for two Peclet numbers. Larger $L/p$ ratio indicates smaller pitch width and thus smaller width of the positive and negative bands. $\lambda_p = 0.5$ has been used for this simulation. All other simulation parameters are the same as that in Figure 5.4

As we did for the spherical collectors, we investigate the dependence of the overall Sherwood number on the favorable area fractions and compare the results with the patchwise heterogeneity model Song et al. [1994] (Equation 4.9).The overall deposition rates predicted by the patchwise heterogeneity model is independent of the spatial characteristics of the surface heterogeneity. However, Figure 5.2 indicates that at a given location along the channel length, the particle accumulation can be much higher compared to the homogeneous analogue which will result in significantly higher deposition rates locally. This is primarily due to the coupling of the various transport mechanisms. Since, the overall deposition rate is simply a length averaging of the local deposition rates on the channel wall, the comparatively high deposition rates over the favorable stripes compensates for the zero deposition rates over the unfavorable stripes. Thus, the overall deposition rates at even 50% favorable surface coverage are comparable to those of a homogeneously favorable channel.

Figure 5.6 shows the variation of scaled overall particle deposition rate $Sh_{avg}/Sh_0$ with favorable area fraction of the microchannel, $\lambda_p$. The open circles and open squares denote the results from the convection diffusion migration model for two different Peclet numbers while the solid line with filled triangles denotes the overall deposition rate prediction from the patchwise heterogeneity model. The scaled surface potentials used for this simulation are $\Psi_p = +1$, $\Psi_{s,p} = +1$, $\Psi_{s,n} = -1$. The ionic strength of the solution is $I = 1 \times 10^{-1} M$ and $A_H = 10^{-21}\ J$. The plot indicates a significant difference between the C-D-M results and the patchwise heterogeneity model. As mentioned earlier, this deviation is dependent on the coupling of the various transport mechanisms. Thus for a higher Peclet number, the deviation is more pronounced. An important observation from Figure 5.6 is that for all the simulation conditions depicted, at $\lambda_p = 0.5$, the overall deposition rate is within 30% of the completely favorable analogue. Increasing the Peclet number brings the overall deposition rate even closer to the homogeneously favorable situation at $\lambda_p = 0.5$. It can be is expected that upon decreasing the ionic strength of the solution and increasing the value of the Hamaker constant, the deposition rate will be further enhanced. The reason for the higher deposition rates at higher Peclet number has already been discussed in the previous subsection.

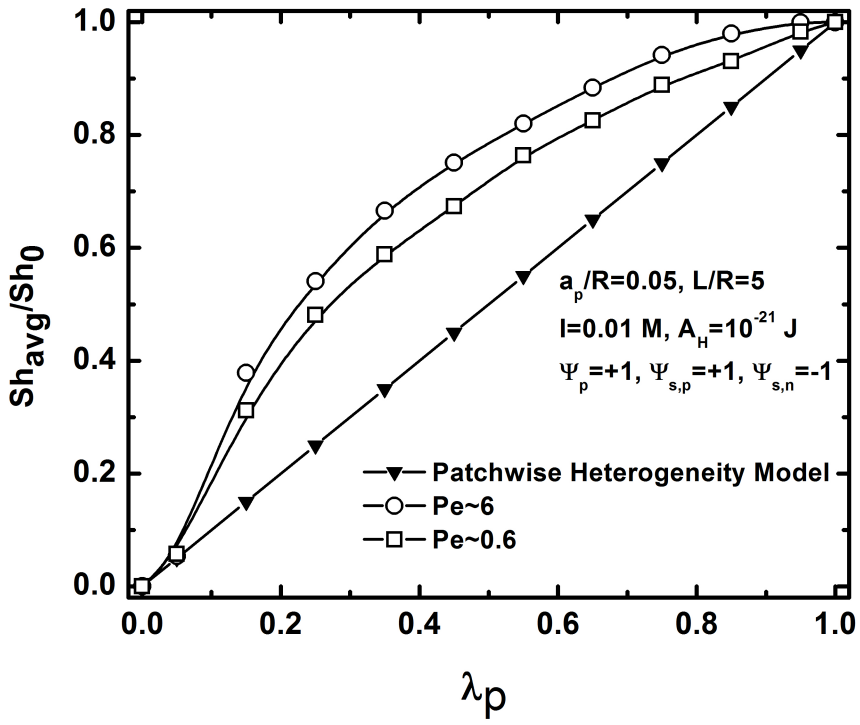


**Figure 5.6** – Variation of scaled overall particle deposition rate $Sh_{avg}/Sh_0$ with favorable area fraction of the microchannel, $\lambda_p$. The open circles and open squares denote the results from the convection diffusion migration model for two Peclet numbers while the solid line with filled triangles denotes the overall deposition rate prediction from the patchwise heterogeneity model. The scaled surface potentials used for this simulation are $\Psi_p = +1$, $\Psi_{s,p} = +1$, $\Psi_{s,n} = -1$. The ionic strength of the solution is $I = 1 \times 10^{-2} M$ and $A_H = 10^{-21}$ $J$.

## 5.4 Summary

A comprehensive analysis of the transport of particles in chemically heterogeneous microchannels was provided in this chapter. The study highlights how particle transport is modified strongly in the presence of surface chemical heterogeneity. Further, the model results showed that frequency of the stripes and the favorable area fraction also effected the particle capture rate at the walls. This suggests that the shape of the heterogeneous patches would also have strong impacts on the particle transport. Most importantly, the analysis showed how surface heterogeneity on the channel walls can be tuned to control the path of the particle inside the channel. Enhanced particle capture at the

leading edge of the favorable stripes also indicated that this technique could be effectively used for drug delivery/targeting in capillaries to biomolecule transport in microfluidic devices. The model can be further improved by incorporating more realistic fluid flow profiles and electrokinetic effects.

# Chapter 6

# Conclusions and Future Work

The primary goal of this thesis was to investigate particle transport and deposition in various porous media geometries. Further, we wanted to establish the correct limiting particle transport behavior onto a homogeneous spherical collector and then extend the model to include surface chemical heterogeneity. Finally, a second model was developed to investigate particle transport in heterogeneous microchannels as it is relevant to various microfluidic/nanofluidic as well as porous media systems. Initial investigation of existing literature indicated a lack of agreement between various particle transport models onto homogeneous spherical collectors in the absence of double layer interactions. The various correlations developed for predicting single collector efficiency seemed to be deficient in some way or the other. Further, a dearth of theoretical models dealing with particle deposition onto spherical collectors with surface chemical heterogeneity was observed. Similarly, for flow in microchannels, no significant model was found which analyzed particle transport in a microchannel with chemically heterogeneous walls. In light of these issues, theoretical results were reported which lends significant insight into particle transport in both spherical and microchannel geometries. The numerical model developed was robust and efficient in terms of computational cost and coding effort. The results from the numerical models highlighted novel aspects of particle deposition which could be employed to improve on the existing filtration and microfluidic/nanofluidic systems.

## 6.1 Concluding Remarks

From the results of the initial section of the thesis where we investigated particle transport and deposition onto homogeneous spherical collectors in the absence of double layer interactions, we conclude the following

1. The Lagrangian and the Eulerian methods both lead to the same conclusion in terms of predicting single collector efficiency for a sphere-in-cell model. The disagreements between the various deposition models was not due to the adopted method, but due to systematic errors in approximation or a manifestation of inappropriate statistical calculations.

2. The Levich solution represents the correct limiting behavior for particle deposition for Brownian particles. For such particles, the effect of the attractive van der Waals interactions and hydrodynamic retardation was insignificant. Hence, the deviation between the collector efficiency values predicted by the various correlations for Brownian particles was not due to the presence of these interactions.

3. Previously it was established that all particles roughly below 1 micron particle radius would lead diffusion dominated deposition. Our model indicated that the Brownian deposition was only predominant for particles below 100 nm. Beyond 100 nm particle radius, the slope of the efficiency curve depends upon the expression for the van der Waals interactions used in the model. As a matter of fact, the deviation of the single collector efficiency values from the Levich equation was due to the retardation factor in the van der Waals interaction energy.

4. Finally, a new correlation was developed to accurately predict the deposition efficiency for the entire range of particle size. The new correlation improved upon the widely used RT and TE correlations. The developed correlation showed remarkable accuracy for the entire parameter space considered in this problem especially for Brownian particles which was till then a matter of constant debate.

Next, the effect of surface chemical heterogeneity on particle deposition onto patterned collectors were investigated. Major conclusions drawn from the study included the following

1. Surface chemical heterogeneity had significant impact on the particle deposition rates. On the favorable stripes, higher local deposition rates were observed compared to a homogenously favorable collector.

2. The particles showed an inherent tendency to deposit at the leading edges of the favorable stripes. This rate of local deposition was dependent on other transport parameters as well.

3. The lower half of the collector seemed to be completely insensitive to deposition even under favorable deposition conditions. This led us to conclude that a spherical collector which is said to have been fouled completely is actually only half fouled. The cleaner lower half could be used to collect particles and thereby increase the retention efficiency and longevity of the filter bed if the collectors could be rotated dynamically.

4. The effect of collector rotation was captured by making the free flow approach the collector at different angles to gravity. Even in gravity opposed flow, the drop in efficiency was with 20% compared to that of gravity assisted mode. This could however be compensated if the collectors could be made to rotate.

5. For a patterned collector, the results indicated that a collector with even 50% favorable area fraction had deposition characteristics very similar to that of a fully favorable collector.

6. We summarized the results from this section of the thesis to propose fluidized field variable porosity filters in which the inter-collector interactions could be employed for varying the system porosity in a fluidized mode thereby reducing Darcy's pressure drop across the bed. This would lead to improved operational life and better deposition efficiency in the filter bed.

Finally for the particle transport in chemically heterogeneous patterned microchannels, we made the following major conclusions

1. As in the case of a spherical collector, particles deposition was maximum at the leading edge of the favorable stripes. However, the extent of deposition decreased along the length of the microchannel. Unlike in a spherical collector though, some deposition was observed beyond half the channel length and near the exit.

2. The overall deposition rate was dependent on the favorable area fraction as well as the width of each favorable stripes (or conversely, the number of favorable stripes). For a given value of favorable area fraction, greater deposition was observed for a greater frequency of the stripes.

3. The numerical results indicated that local deposition rate along the microchannel length could be tuned effectively using such patterning. This would be particularly helpful in analyte and biomolecular transport in microchannel for drug delivery/targeting or doping a particular site on the channel wall.

## 6.2 Future Work

The work presented in this thesis were obtained under a few simplifying assumptions. Although, the results provide a good indication of the particle deposition process onto both homogeneous and heterogeneous surfaces, there is still significant room for improvement in developing better models. Such models would validate the hypotheses presented in this thesis and provide more concrete and indepth knowledge of particle deposition onto the geometries discussed. Among several aspects where the modeling could be improved, the most notable ones are highlighted below.

1. In the evaluation of the particle velocities, we considered that the fluid field is undisturbed by the particle. Although this would be fairly accurate for Brownian particles, this assumption would not hold true for larger particles. Addition modeling of the exact hydrodynamics of the fluid-particle interaction is required to make the model more realistic.

2. In the present model, all the particle deposition rates are calculated for very dilute solution such that inter particle interactions can be neglected. A better model could be developed in which inter particle as well as inter collector interactions would be incorporated.

3. The model developed for the patterned spherical collectors considers fluid flow approaching the collector at different angles but maintains symmetry by assuming that the stripes are always normal to the free stream flow direction. There is a massive scope in improving this model by considering a full 3D geometry in which the flow direction and the orientation of

the stripes could be varied independently. Since, the model talks about developing a system in which the collectors are dynamically rotating, this would be an apt direction to delve into further investigation.

4. In designing a fluidized bed system would require full porous bed modeling. Although the single collector deposition rates present a good indication of what the overall deposition of the entire filter would be, more concrete results must be produced to validate this claim. This can only be achieved by considering a system in which a cluster of collectors is considered and flow of suspension through it is investigated.

5. In the model where we discussed particle transport in a microchannel, we considered neutrally buoyant particles to ensure 2D symmetry was maintained. This would not be the case in all practical situations. Hence, 3D simulations must be performed once again to develop a complete picture of particle transport in a microchannel.

6. Again, for the patterned microchannel model, fully developed Poiseuille flow was considered. It will be interesting to investigate the reservoir effects, particle deposition under the condition when flow is not fully developed and also a more realistic flow field since a pure Poiseuille flow is never really achieved in practice. Electrokinetic transport could also be incorporated to improve the model.

# Bibliography

*Description of DASSL: A differential-algebraic system solver. Technical Report SAND82-8637, Sandia National Laboratory. (1982).*

Adamczyk, Z. and van de Ven, T. G. M. Deposition of particles under external forces in laminar-flow through parallel-plate and cylindrical channels. *J. Colloid Interface Sci.*, 80(2):340–356, 1981.

Adamczyk, Z., Dabros, T., and Czarnecki, J. Thoery for Particle Deposition onto Rotating-Disk Surface. *Acta Phys. Pol. A*, 53(2):347–356, 1978.

Adamczyk, Z., Dabros, T., Czarnecki, J. and van de Ven, T. G. M. Particle transfer to solid-surfaces. *Adv. Colloid Interface Sci.*, 19(3):183–252, 1983.

Adamczyk, Z., Zembala, M., Siwek, B., and Czarnecki, J. Kinetics of latex particle deposition from flowing suspensions. *J Colloid Interface Sci.*, 110 (1):188–200, 1986.

Al Quddus, N., Moussa, W. A., and Bhattacharjee, S. Motion of a spherical particle in a cylindrical channel using arbitrary Lagrangian-Eulerian method. *J Colloid Int. Sci.*, 317(2):620–630, 2008.

Ali, F. S., Base, T .E., and Inculet, I. I. Mathematical modeling of powder paint particle trajectories in electrostatic painting. *IEEE Transactions on Industry Applications*, 36(4):992–997, 2000.

Bacchin, P., Marty, A., Duru, P., Meireles, M., and Aimar, P. Colloidal surface interactions and membrane fouling: Investigations at pore scale. *Adv. Colloid Interface Sci.*, 164(1-2, Sp. Iss. SI):2–11, MAY 11 2011.

Behrend, C. J., Anker, J. N., McNaughton, B. H., Brasuel, M., Philbert, M. A., and Kopelman, R. Metal-capped brownian and magnetically modulated op-

tical nanoprobes (moons): Micromechanics in chemical and biological microenvironments. *J. Phys. Chem. B*, 108(29):10408–10414, 2004.

Bendersky, M. and Davis, J. M. DLVO interaction of colloidal particles with topographically and chemically heterogeneous surfaces. *J. Colloid Interface Sci.*, 353(1):87–97, 2011.

Bernate, J. A. and Drazer, G. Partition-induced vector chromatography in microfluidic devices. *J Colloid Interface Sci.*, 356(1):341–351, 2011.

Binks, B. P. and Fletcher, P. D. I. Particles adsorbed at the oil-water interface: A theoretical comparison between spheres of uniform wettability and "Janus" particles. *Langmuir*, 17(16):4708–4710, 2001.

Bormashenko, E., Bormashenko, Y., Pogreb, R., and Gendelman, O. Janus Droplets: Liquid Marbles Coated with Dielectric/Semiconductor Particles. *Langmuir*, 27(1):7–10, 2011.

Brenner, H. The slow motion of a sphere through a viscous fluid towards a plane surface. *Chem. Eng. Sci.*, 16(3-4):242–251, 1961.

Buffham, B. A. Model-independent aspects of field-flow fractionation theory. *J Colloid Interface Sci.*, 181(2):490–502, 1996.

Chein, R. and Dutta, P. Effect of charged membrane on the particle motion through a nanopore. *Colloids Surf., A*, 341(1-3):1–12, 2009.

Chen, G., Bedi, R. S., Yan, Y. S. , and Walker, S. L. Initial Colloid Deposition on Bare and Zeolite-Coated Stainless Steel and Aluminum: Influence of Surface Roughness. *Langmuir*, 26(15):12605–12613, 2010.

Chen, J. Y., Ko, C. H., Bhattacharjee, S., and Elimelech, M. Role of spatial distribution of porous medium surface charge heterogeneity in colloid transport. *Colloids Surf., A*, 191(1-2, Sp. Iss. SI):3–15, 2001.

Chen, K. M., Jiang, X. P., Kimerling, L. C., and Hammond, P. T. Selective self-organization of colloids on patterned polyelectrolyte templates. *Langmuir*, 16(20):7825–7834, 2000.

Chute, J. A., Hawker, C. J., Rasmussen, K. O., and Welch, P. M. The Janus Character of Heterogeneous Dendritic Nanoparticles. *Macromol.*, 44(4): 1046–1052, 2011.

Civan, F. Non-isothermal Permeability Impairment by Fines Migration and Deposition in Porous Media including Dispersive Transport. *Transp. Porous Media*, 85(1):233–258, 2010.

Czarnecki, J. Van der waals attraction energy between sphere and half-space. *J. Colloid Interface Sci.*, 72:361–362, 1979.

Czarnecki, J. The effects of surface inhomogeneities on the interactions in colloidal systems and colloid stability. *Adv. Colloid Interface Sci.*, 24(4): 283–319, 1986.

Czarnecki, J . and Dabros, T. Attenuation of the van der waals attraction energy in the particle semi-infinite medium system due to the roughness of the particle surface. *J Colloid Interface Sci.*, 78(1):25–30, 1980.

Dabros, T. and Adamczyk, Z. Non-inertial particle transfer to the rotating disk under an external force field (laminar flow). *Chem. Eng. Sci.*, 34(8): 1041–1049, 1979.

Dabros, T. and van de Ven, T. G. M. A direct method for studying particle deposition onto solid-surfaces. *Colloid Polymer Sci.*, 261(8):694–707, 1983.

Das, P. K. and Bhattacharjee, S. Electrostatic double layer force between a sphere and a planar substrate in the presence of previously deposited spherical particles. *Langmuir*, 21(10):4755–4764, 2005.

Das, P. K., Bhattacharjee, S., and Moussa, W. A. Electrostatic double layer force between two spherical particles in a straight cylindrical capillary: Finite element analysis. *Langmuir*, 19(10):4162–4172, 2003.

Derjaguin, B. V. and Landau, L. Theory of the stability of strongly charged lyophobic sols and of the adhesion of strongly charged particles in solutions of electrolytes. *Acta Physicochim.*, 14:633–662, 1941.

Dickinson, E. Brownian dynamics with hydrodynamic interactions - the application to protein diffusional problems. *Chem. Soc. Rev.*, 14(4):421–455, 1985.

Duffadar, R. D. and Davis, J. M. Dynamic adhesion behavior of micrometer-scale particles flowing over patchy surfaces with nanoscale electrostatic heterogeneity. *J Colloid Interface Sci.*, 326(1):18–27, 2008.

Edward, J. T. Molecular volumes and stokes-einstein equation. *J. Chem. Educ.*, 47(4):261–&, 1970.

Elimelech, M. Particle deposition on ideal collectors from dilute flowing suspensions - mathematical formulation, numerical solution, and simulations. *Sep. Technol.*, 4(4):186–212, 1994.

Elimelech, M., Gregory, J., Jia, X., and Williams, R. A. *Particle Deposition and Aggregation: Measurement, Modeling and Simulation*. Butterworth Heinemann, Oxford, 1995.

Elimelech, M., Chen, J. Y., and Kuznar, Z. A. Particle deposition onto solid surfaces with micropatterned charge heterogeneity: The "hydrodynamic bump" effect. *Langmuir*, 19(17):6594–6597, 2003.

Erickson, D. and Li, D. Q. Microchannel flow with patchwise and periodic surface heterogeneity. *Langmuir*, 18(23):8949–8959, 2002.

Erickson, D. and Li, D. Q. Three-dimensional structure of electroosmotic flow over heterogeneous surfaces. *J Phys. Chem. B*, 107(44):12212–12220, 2003.

Felten, M., Staroske, W., Jaeger, M. S., Schwille, P., and Duschl, C. Accumulation and filtering of nanoparticles in microchannels using electrohydrodynamically induced vortical flows. *Electrophoresis*, 29(14):2987–2996, 2008.

Fridjonsson, E. O., Seymour, J. D., Cokelet, G. R., and Codd, S. L. Dynamic NMR microscopy measurement of the dynamics and flow partitioning of colloidal particles in a bifurcation. *Exp. Fluids*, 50(5):1335–1347, 2011.

Godinez, I. G. and Darnault, C. J. G. Aggregation and transport of nano-TiO2 in saturated porous media: Effects of pH, surfactants and flow velocity. *Water Res.*, 45(2):839–851, 2011.

Goldman, A. J., Cox, R. G., and Brenner, H. Slow viscous motion of a sphere parallel to a plane wall .i. motion through a quiescent fluid. *Chem. Eng. Sci.*, 22(4):637–&, 1967.

Goren, S. L. and Oneill, M. E. Hydrodynamic resistance to a particle of a dilute suspension when in neighbourhood of a large obstacle. *Chem. Eng. Sci.*, 26(3):325–&, 1971.

Gudipaty, T., Stamm, M. T., Cheung, L. S. L., Jiang, L., and Zohar, Y. Cluster formation and growth in microchannel flow of dilute particle suspensions. *Microfluid. Nanofluid.*, 10(3):661–669, 2011.

Hamaker, H. C. London van der waals attraction between spherical particles. *Physica*, 4:1058–1072, 1937.

Happel, J. Viscous flow in multiparticle systems - slow motion of fluids relative to beds of spherical particles. *AIChE J.*, 4(2):197–201, 1958.

Happel, J. and Brenner, H. *Low Reynolds Number Hydrodynamics*. Prentice Hall, Englewood Cliffs, New Jersey, 1965.

Henry, C., Minier, J. P., Lefevre, G., and Hurisse, O. Numerical Study on the Deposition Rate of Hematite Particle on Polypropylene Walls: Role of Surface Roughness. *Langmuir*, 27(8):4603–4612, 2011.

Herman, M. C. and Papadopoulos, K. D. Effects of asperities on the van der waals and electric double-layer interactions of 2 parallel flat plates. *J Colloid Interface Sci.*, 136(2):385–392, 1990.

Hiemstra, T. and VanRiemsdijk, W. H. A surface structural approach to ion adsorption: The charge distribution (CD) model. *J Colloid Interface Sci.*, 179(2):488–508, 1996.

Hoek, E. M. V., Bhattacharjee, S., and Elimelech, M. Effect of membrane surface roughness on colloid-membrane DLVO interactions. *Langmuir*, 19 (11):4836–4847, 2003.

Hogg, R., Healy, T. W., and Fuersten, D. W. Mutual coagulation of colloidal dispersions. *Trans Faraday Soc.*, 62(522P):1638–&, 1966.

Honig, E. P., Roeberse, G. J., and Wiersema, P. H. Effect of hydrodynamic interaction on coagulation rate of hydrophobic colloids. *J Colloid Interface Sci.*, 36(1):97–&, 1971.

Howse, J. R., Jones, R .A. L., Ryan, A. J., Gough, T., Vafabakhsh, R., and Golestanian, R. Self-motile colloidal particles: From directed propulsion to random walk. *Phys. Rev. Lett.*, 99(4), 2007.

Hunter, R. J. *Foundations of Colloid Science*. 2nd ed., Oxford University Press, Oxford, 2001.

Hunter, R. J. *Zeta Potential in Colloid Science*. Academic Press, London, 1981.

Israelachvili, J. *Intermolecular and Surface Forces*. 2nd ed., Academic Press, New York, 1992.

Kalasin, S. and Santore, M. M. Sustained Rolling of Microparticles in Shear Flow over an Electrostatically Patchy Surface. *Langmuir*, 26(4):2317–2324, 2010.

Kemps, J. A. L. The effects of substrate heterogeneity on colloid deposition. Master's thesis, University of Alberta, 2010.

Kemps, J. A. L. and Bhattacharjee, S. Interactions between a solid spherical particle and a chemically heterogeneous planar substrate. *Langmuir*, 21(25): 11710–11721, 2005.

Kemps, J. A. L. and Bhattacharjee, S. Particle Tracking Model for Colloid Transport near Planar Surfaces Covered with Spherical Asperities. *Langmuir*, 25(12):6887–6897, 2009.

Kim, S. and Karrila, S. J. *Microhydrodynamics: Principles and Selected Applications*. Dover Publications, Mineola, NY, 2005.

Levich, V. G. *Physicochemical Hydrodynamics*. Prentice Hall, Englewood Cliffs, N.J, 1962.

Liang, F., Liu, J., Zhang, C., Qu, X., Li, J., and Yang, Z. Janus hollow spheres by emulsion interfacial self-assembled sol-gel process. *Chem. Comm.*, 47(4): 1231–1233, 2011.

Lifshitz, E. M. The theory of molecular attractive forces between solids. *Soviet Physics JETP-USSR*, 2(1):73–83, 1956.

Lin, E., Page, D., and Pavelic, P. A new method to evaluate polydisperse kaolinite clay particle removal in roughing filtration using colloid filtration theory. *Water Res.*, 42(3):669–676, 2008.

Liu, C., Luo, Y., Fang, N., and Chen D. D. Analyte Distribution at Channel Intersections of Electro-Fluid-Dynamic Devices. *Anal. Chem.*, 83(4):1189–1192, 2011.

Liu, S., Wang, Q., Ma, H., Huang, P., Li, J., and Kikuchi, T. Effect of microbubbles on coagulation flotation process of dyeing wastewater. *Sep. Purif. Technol.*, 71(3):337–346, 2010.

Long, W. and Hilpert, M. A Correlation for the Collector Efficiency of Brownian Particles in Clean-Bed Filtration in Sphere Packings by a Lattice-Boltzmann Method. *Environ. Sci. Technol.*, 43(12):4419–4424, 2009.

Loveland, J. P., Bhattacharjee, S., Ryan, J. N., and Elimelech, M. Colloid transport in a geochemically heterogeneous porous medium: aquifer tank experiment and modeling. *J. Contam. Hydrol.*, 65(3-4):161–182, 2003.

Ma, H. and Johnson, W. P. Colloid Retention in Porous Media of Various Porosities: Predictions by the Hemispheres-in-Cell Model. *Langmuir*, 26(3): 1680–1687, 2010.

Ma, H., Pedel, J., Fife. P, and Johnson, W. P. Hemispheres-in-cell geometry to predict colloid deposition in porous media. *Environ. Sci. Technol.*, 43 (22):8573–8579, 2009.

Mamleev, V. S., Villieras, F., and Cases, J. M. Adsorption of spherical molecules in probing the surface topography. 1. Patchwise heterogeneity model. *Langmuir*, 18(6):2075–2088, 2002.

Masliyah, J. H. and Bhattacharjee, S. *Electrokinetic and Colloid Transport Phenomenon*. Wiley-Interscience, 2006.

Miller, A. W., Rodriguez, D. R., and Honeyman, B. D. Upscaling sorption/desorption processes in reactive transport models to describe metal/radionuclide transport: A critical review. *Environ. Sci. Technol.*, 44(21):7996–8007, 2010.

Molla, S. and Bhattacharjee, S. Dielectrophoretic levitation in the presence of shear flow: Implications for colloidal fouling of filtration membranes. *Langmuir*, 23(21):10618–10627, 2007.

Nazemifard, N. Particle deposition onto charge heterogeneous surfaces in radial impinging jet system. Master's thesis, University of Alberta, 2006.

Nazemifard, N., Masliyah, J. H., and Bhattacharjee, S. Particle deposition onto charge heterogeneous surfaces: Convection-diffusion-migration model. *Langmuir*, 22(24):9879–9893, 2006.

Nelson, K. E. and Ginn, T. R. Colloid filtration theory and the Happel sphere-in-cell model revisited with direct numerical simulation of colloids. *Langmuir*, 21(6):2173–2184, 2005.

Nelson, K. E. and Ginn, T. R. Comment on Particle Tracking Model for Colloid Transport near Planar Surfaces Covered with Spherical Asperities. *Langmuir*, 25(21):12835–12836, 2009.

Ngene, I. S., Lammertink, R. G. H., Wessling, M., and van der Meer, W. A microfluidic membrane chip for in situ fouling characterization. *J Membrane Sci.*, 346(1):202–207, 2010.

Ninham, B. W. On progress in forces since the DLVO theory. *Adv. Colloid Interface Sci.*, 83(1-3):1–17, 1999.

Pardhy, N. P. and Budhlall, B. M. Pickering Emulsion as a Template to Synthesize Janus Colloids with Anisotropy in the Surface Potential. *Langmuir*, 26(16):13130–13141, 2010.

Payatakes, A. C., Rajagopan, R., and Tien, C. Use of happels model for filtration studies. *J. Colloid Interface Sci.*, 49(2):321–325, 1974.

Pegueroles, M., Aparicio, M., Bosio, M., Engel, M., Gil, F. J., Planell, J. A., and Altankov, G. Spatial organization of osteoblast fibronectin matrix on titanium surfaces: Effects of roughness, chemical heterogeneity and surface energy. *Acta Biomaterialia*, 6(1):291–301, 2010.

Perro, A. and Manoharan, V. N. Bulk Synthesis of Polymer-Inorganic Colloidal Clusters. *Langmuir*, 26(24):18669–18675, 2010.

Petit, L., Manaud, J. P., Mingotaud, C., Ravaine, S., and Duguet, E. Submicrometer silica spheres dissym-metrically decorated with gold nanoclusters. *Mater. Lett.*, 51(6):478–484, 2001.

Petosa, A. R., Jaisi, D. P., Quevedo, I. R., Elimelech, M., and Tufenkji, N. Aggregation and Deposition of Engineered Nanomaterials in Aquatic Environments: Role of Physicochemical Interactions. *Environ. Sci. Technol.*, 44 (17):6532–6549, 2010.

Phenrat, T., Kim, H. J,, Fagerlund, F., Illangasekare, T., and Lowry, G. V. Empirical correlations to estimate agglomerate size and deposition during injection of a polyelectrolyte-modified Fe-0 nanoparticle at high particle concentration in saturated sand. *J. Contam. Hydrol.*, 118(3-4, Sp. Iss. SI): 152–164, 2010.

Prieve, D. C. and Ruckenstein, E. Effect of london forces upon rate of deposition of brownian particles. *AIChE J.*, 20(6):1178–1187, 1974.

Rajagopalan, R. and Tien, C. Comment on "Correlation equation for predicting single-collector efficiency in physicochemical filtration in saturated porous media". *Environ. Sci. Technol.*, 39(14):5494–5495, 2005.

Rajagopalan, R. and Tien, C. Trajectory analysis of deep-bed filtration with sphere-in-cell porous-media model. *AIChE J.*, 22(3):523–533, 1976. ISSN 0001-1541.

Rizwan, T. and Bhattacharjee, S. Particle deposition onto charge-heterogeneous substrates. *Langmuir*, 25(9):4907–4918, 2009.

Ruckenstein, E. On mass transfer in the continuous phase from spherical bubbles or drops. *Chem. Eng. Sci.*, 19(2):131–146, 1964.

Ryan, J. N. and Elimelech, M. Colloid mobilization and transport in groundwater. *Colloids Surf., A*, 107:1–56, 1996. Symposium on Colloidal and Interfacial Phenomena to Aquatic Environments, at the 209th National Meeting of the American-Chemical-Society, Anaheim, 1995.

Saadatmand, M., Ishikawa, T., Matsuki, N., Abdekhodaie, M. J., Imai, Y., Ueno, H., and Yamaguchi, T. Fluid particle diffusion through high-hematocrit blood flow within a capillary tube. *J. Biomech.*, 44(1):170–175, 2011.

Saiers, J. E. and Ryan, J. N. Colloid deposition on non-ideal porous media: The influences of collector shape and roughness on the single-collector efficiency. *Geophys. Res. Lett.*, 32(21):1–5, 2005.

Santillo, M. F., Ewing, A. G., and Heien, M. L. Trends in computational simulations of electrochemical processes under hydrodynamic flow in microchannels. *Anal. Bioanal. Chem.*, 399(1):183–190, 2011.

Sbai, M. A. and Azaroual, M. Numerical modeling of formation damage by two-phase particulate transport processes during CO2 injection in deep heterogeneous porous media. *Adv. Water Resour.*, 34(1):62–82, 2011.

Schenkel, J. H. and Kitchener, J. A. A test of the derjaguin-verwey-overbeek theory with a colloidal suspension. *Trans Faraday Soc.*, 56:161–173, 1960.

Shellenberger, K. and Logan, B. E. Effect of molecular scale roughness of glass beads on colloidal and bacterial deposition. *Environ. Sci. Technol.*, 36(2): 184–189, 2002.

Shen, C., Huang, Y., Li, B., and Jin, Y. Predicting attachment efficiency of colloid deposition under unfavorable attachment conditions. *Water Resour. Res.*, 46, 2010.

Soliman, W., Bhattacharjee, S., and Kaur, K. Adsorption of an Antimicrobial Peptide on Self-Assembled Monolayers by Molecular Dynamics Simulation. *J. Phys. Chem. B*, 114(34):11292–11302, 2010.

Song, L. F. and Elimelech, M. Deposition of brownian particles in porous media : Modified boundary conditions for the sphere-in-cell model. *J. Colloid Interface Sci.*, 153(1):294–297, 1992.

Song, L. F. and Elimelech, M. Calculation of particle deposition rate under unfavorable particle surface interactions. *J Chem. Soc.-Faraday Trans.*, 89 (18):3443–3452, 1993.

Song, L. F., Johnson, P. R., and Elimelech, M. Kinetics of colloid deposition onto heterogeneously charged surfaces in porous-media. *Environ. Sci. Technol.*, 28(6):1164–1171, 1994.

Spielman, L. A. Particle capture from low-speed laminar flows. *Annu. Rev. Fluid Mech*, 9:297–319, 1977.

Spielman, L. A. and Fitzpatr, J. A. Theory for particle collection under london and gravity forces. *J Colloid Interface Sci.*, 42(3):607–623, 1973.

Sun, N. and Walz, J. Y. A model for calculating electrostatic interactions between colloidal particles of arbitrary surface topology. *J Colloid Interface Sci.*, 234(1):90–105, 2001.

Sunkara, B., Zhan, J., He, J., McPherson, G. L., Piringer, G., and John, V. T. Nanoscale Zerovalent Iron Supported on Uniform Carbon Microspheres for the In situ Remediation of Chlorinated Hydrocarbons. *ACS Appl. Mater. Interfaces*, 2(10):2854–2862, 2010.

Suresh, L. and Walz, J. Y. Effect of surface roughness on the interaction energy between a colloidal sphere and a flat plate. *J Colloid Interface Sci.*, 183(1):199–213, 1996.

Tien, C. *Granular Filtration of Aerosols and Hydrosols*. Butterworths, Stoneham, MA, 1989.

Torkzaban, S., Kim, Y., Mulvihill, M., Wan, J., and Tokunaga, T. K. Transport and deposition of functionalized cdte nanoparticles in saturated porous media. *J. Contam. Hydrol.*, 118(3-4):208–217, 2010.

Torrie, G. M. and Valleau, J. P. Monte-carlo study of an electrical double-layer. *Chem. Phys. Lett*, 65(2):343–346, 1979.

Tufenkji, N. and Elimelech, M. Response to comment on "Correlation equation for predicting single-collector efficiency in physicochemical filtration in saturated porous media". *Environ. Sci. Technol.*, 39(14):5496–5497, 2005.

Tufenkji, N. and Elimelech, M. Correlation equation for predicting single-collector efficiency in physicochemical filtration in saturated porous media. *Environ. Sci. Technol.*, 38(2):529–536, 2004.

Vaidyanathan, R. and Tien, C. Hydrosol deposition in antigranulocytes media under unfavorable surface conditions. *Chem. Eng. Sci.*, 46(4):967–983, 1991.

van de Ven, T. G. M. *Colloidal Hydrodynamics*. Academic Press. San Diego, 1989.

Verwey, E. J. W. and Overbeek, J. Th. G. *Theory of the Stability of Lyophobic Colloids*. Elsevier, Amsterdam, 1948.

Waghmare, P. R. and Mitra, S. K. Finite reservoir effect on capillary flow of microbead suspension in rectangular microchannels. *J Colloid Interface Sci.*, 351(2):561–569, 2010a.

Waghmare, P. R. and Mitra, S. K. Mechanism of cell transport in a microchannel with binding between cell surface and immobilized biomolecules. volume 12, pages 779–784, 2010b.

Waghmare, P. R. and Mitra, S. K. A generalized analysis of electroosmotically driven capillary flow in rectangular microchannels. In *ICNMM 2009, Pts A-B*, pages 203–210, 2009. ISBN 978-0-7918-4349-9.

Waghmare, P. R. and Mitra, S. K. Mechanism of cell transport in a microchannel with binding between cell surface and immobilized biomolecules. In *IMECE 2009: Proceedings of the ASME International Mechanical Engineering Congress and Exposition, Vol 12, Pts A and B*, pages 779–784, 2010.

Walther, A. and Mueller, A. H. E. Janus particles. *Soft Matter*, 4(4):663–668, 2008.

Westall, J. and Hohl, H. Comparison of electrostatic models for the oxide solution interface. *Adv. Colloid Interface Sci.*, 12(4):265–294, 1980.

Wheat, P. M., Marine, N. A., Moran, J. L., and Posner, J. D. Rapid Fabrication of Bimetallic Spherical Motors. *Langmuir*, 26(16):13052–13055, 2010.

Yang, J., Masliyah, J. H., and Kwok, D. Y. Streaming potential and electroosmotic flow in heterogeneous circular microchannels with nonuniform zeta potentials: Requirements of flow rate and current continuities. *Langmuir*, 20(10):3863–3871, 2004.

Yao, K. M., Habibian, M. M., and Omelia, C. R. Water and waste water filtration - concepts and applications. *Environ. Sci. Technol.*, 5(11):1105–&, 1971.

Zhang, Z. L. and Glotzer, S. C. Self-assembly of patchy particles. *Nano Letters*, 4(8):1407–1413, 2004.

Zhao, K. and Mason, T. G. Suppressing and enhancing depletion attractions between surfaces roughened by asperities. *Phys. Rev. Lett.*, 101(14), 2008.

Zhao, R., Marhefka, J. N., Antaki, J. F., and Kameneva, M. V. Drag-reducing polymers diminish near-wall concentration of platelets in microchannel blood flow. *Biorheol.*, 47(3-4):193–203, 2010.

Zheng, H. P., Lee, I., Rubner, M. F., and Hammond, P. T. Two component particle arrays on patterned polyelectrolyte multilayer templates. *Adv. Mater.*, 14(8):569–572, 2002.

Zwillinger, D. *Handbook of Differential Equations*. Academic Press, San Diego, 1998.